DIAGNOSTICS OF AIR GAP ECCENTRICITY IN CLOSED-LOOP DRIVE-CONNECTED INDUCTION MOTORS

A Dissertation
Presented to
The Academic Faculty

by

Xianghui Huang

In Partial Fulfillment
of the Requirements for the Degree
Doctor of Philosophy in
Electrical Engineering

School of Electrical and Computer Engineering
Georgia Institute of Technology
May 2005

DIAGNOSTICS OF AIR GAP ECCENTRICITY IN CLOSED-LOOP DRIVE-CONNECTED INDUCTION MOTORS

Approved by:

Dr. T. G. Habetler, Chair
School of Electrical and Computer Engineering
Georgia Institute of Technology

Dr. R. G. Harley
School of Electrical and Computer Engineering
Georgia Institute of Technology

Dr. D. Divan
School of Electrical and Computer Engineering
Georgia Institute of Technology

Date Approved: March 29, 2005

ACKNOWLEDGEMENT

During my Ph.D. study at Georgia Tech, I have been fortunate to receive valuable suggestions, guidance, and support from my mentors, colleagues, family, and friends.

I am greatly appreciative to my advisor, Dr. Thomas Habetler, for his continual guidance and support. He has been a source of motivation and inspiration throughout the course of this work. I feel grateful to Dr. Ronald Harley, for his time and invaluable input into my research. I have benefited immensely from his knowledge and experience. I would also like to thank Dr. Deepak Divan, Dr. Russell Callen and Dr. Charles Ume for their time, input, and for serving on my thesis committee.

I would like to acknowledge Eaton Corporation for providing the financial support necessary to conduct this work.

I must also thank the machinists, Lorand Csizar and Louis Boulanger, who were always available and willing to help with the laboratory experimental setup.

I wish to thank Dr. Jose Restrepo and my colleagues, Dr. Wiehan le Roux, Dr. Rangarajan Tallam, Dr. Ramzy Obaid, Dr. Dong-Myung Lee, Dr. Jason Stack, Dr. Jung-Wook Park, Salman Mohagheghi, Satish Rajagopalan and Zhi Gao for their help and accompany throughout this study.

I am deeply indebted to my grandmother, parents, sister, and brother for a lifetime of support, encouragement, and education. Lastly, I would like to thank my wife Yi Liu whose love, support and understanding has helped to make everything I have accomplished possible.

TABLE OF CONTENTS

LIST OF TABLES

LIST OF FIGURES

SUMMARY

The goal of this research is to develop a reliable, cost-effective detection scheme for air gap eccentricity in closed-loop drive-connected induction motors. A literature review of existing methods in motor condition monitoring is presented. The majority of existing detection methods deals with only line-fed motors, which is insufficient for the fault detection of closed-loop drive-connected induction motors. Analysis of existing methods identifies the motivation of this investigation.

The development of the proposed detection scheme begins with an investigation of how the eccentricity-related fault harmonics distribute in a closed-loop motor-drive system. As motor voltage and current are modified by the converter, the appearance of the fault harmonics in the motor voltage and current is affected by the closed-loop speed and current feed-back controllers. Next, the effects on fault detection of the misalignment associated with the mechanical load are discussed. The misalignment is caused by coupling an eccentric rotor with a mechanical load through a flexible coupling and results in a position-varying load torque that can change the distribution of fault harmonics. As a result of the above analysis, a sensorless detection method is proposed based on monitoring the space vector forms of stator voltage and current together, which ensures good detection sensitivity and reliability.

One challenge in this investigation is that operating conditions of a drive-connected motor vary widely. The eccentricity-related harmonic amplitudes change accordingly because of the mechanical resonance of a torsional spring system consisting of a motor and load. The relationship between fault harmonic amplitudes and operating

conditions depends on many factors and cannot be formulated as strict analytical equations. Therefore, an artificial neural network is used to learn the complex relationship and to test motor conditions.

A series of simulations and laboratory experiments are conducted to verify the analysis and to test the performance of the proposed diagnostic scheme. The results validate that the diagnostic scheme is feasible over the entire range of operating conditions of experimental motors.

The effect of air gap eccentricity on surge test data is analyzed. A new off-line method to detect rotor eccentricity faults using a surge tester is experimentally verified.

The conclusions, contributions, and recommendations are summarized at the end.

CHAPTER 1

INTRODUCTION AND OBJECTIVE OF RESEARCH

1.1 Introduction

Electrical machines are a necessary part of our daily life. As important elements in electromechanical energy conversion, they are used in many fields, such as power generation, the paper industry, oil fields, manufacturing, etc. Among electrical machines, induction motors are the most widely used in industry because of their rugged configuration, low cost, and versatility. With their great contributions, induction motors are called the workhorse of industry.

Because of natural aging processes and other factors in practical applications, induction motors are subject to various faults. Those faults disturb the safe operation of motors, threaten normal manufacturing, and can result in substantial cost penalties. The field of motor condition monitoring recognizes those problems, and more and more relative research is being devoted to it by industry and academia. With condition monitoring, an incipient fault can be detected at an early stage. Appropriate maintenance can then be scheduled at a planned downtime, avoiding a costly emergency. This reduces downtime expense and reduces the occurrence of catastrophic failures.

With the rapid developments in digital signal processing and power electronic devices, variable-speed induction motor applications have become common. AC drives can provide qualified control performance with a comparatively low price like DC drives. However, the use of AC drives adds significant challenges to fault detection. Unlike traditional condition monitoring methods dealing with main or line-fed induction motors,

more sophisticated techniques are required for sensitive and reliable fault detection of closed-loop drive-connected induction motors.

1.2 Common Types of Induction Motor Faults

There are several types of faults that may occur in induction motors. According to a survey by EPRI in 1982, about 41% of all induction motor failures are caused by bearing faults, 37% by stator faults, 10% by rotor faults, and 12% by miscellaneous faults [1].

Bearing faults are categorized as inner race faults and outer race faults by the location of occurrences. The most common causes of bearing faults include contamination of lubricant, loss of lubricant, over-loading, and excess heating. The ultimate result is either extreme vibration leading to catastrophic failure, or a complete seizure of the bearing [52].

Stator faults are basically caused by a breakdown of winding insulation, which may result from excess thermal or voltage stress, mechanical vibration, or even an abrasion between the stator and rotor. The weakness of winding insulation may further result in a turn-to-turn short circuit and eventually a winding-to-ground short circuit [53].

There are two types of rotor faults. One is associated with the rotor itself, such as a bar defect or bar breakage. This type of fault occurs from thermal stresses, hot spots, or fatigue stresses during transient operations such as startup, especially in large motors. A broken bar changes torque significantly and is dangerous to the safe and consistent operation of electric machines [54].

The second type of rotor fault is related to air gap eccentricity. Air gap eccentricity is a common effect arising from a range of mechanical problems in induction motors such as load unbalance or shaft misalignment. Long-term load unbalance can cause damage of the bearings and the bearing housing, which will influence air gap symmetry. Shaft misalignment means horizontal, vertical, or radial misalignment between a shaft and its coupled load. With shaft misalignment, the rotor will be displaced from its normal position because of a constant radial force.

1.3 Problem Statement

The research in detecting air gap eccentricity of induction motors began in the 20th century. Existing detection schemes are classified by the type of monitoring parameters. Examples of monitoring parameters include torque, flux, vibration signal, and stator current. Depending on whether the minimum air gap is spatially fixed or not, air gap eccentricity is described as being either static or dynamic. For static eccentricity, the rotor shifts from its normal position at the center of the stator and rotates around its own center. For dynamic eccentricity, the rotor shifts from its normal position, but still rotates around the center of the stator. Figure 1.1 illustrates the different cases of eccentricity.

Air gap eccentricity may result from the assembly and manufacturing processes. For example, static eccentricity is caused by manufacturing tolerances between the center of the stator bore and bearing centers. Dynamic eccentricity in a new motor is controlled by the total indicated reading (TIR) of the rotor [4, 5, 6].

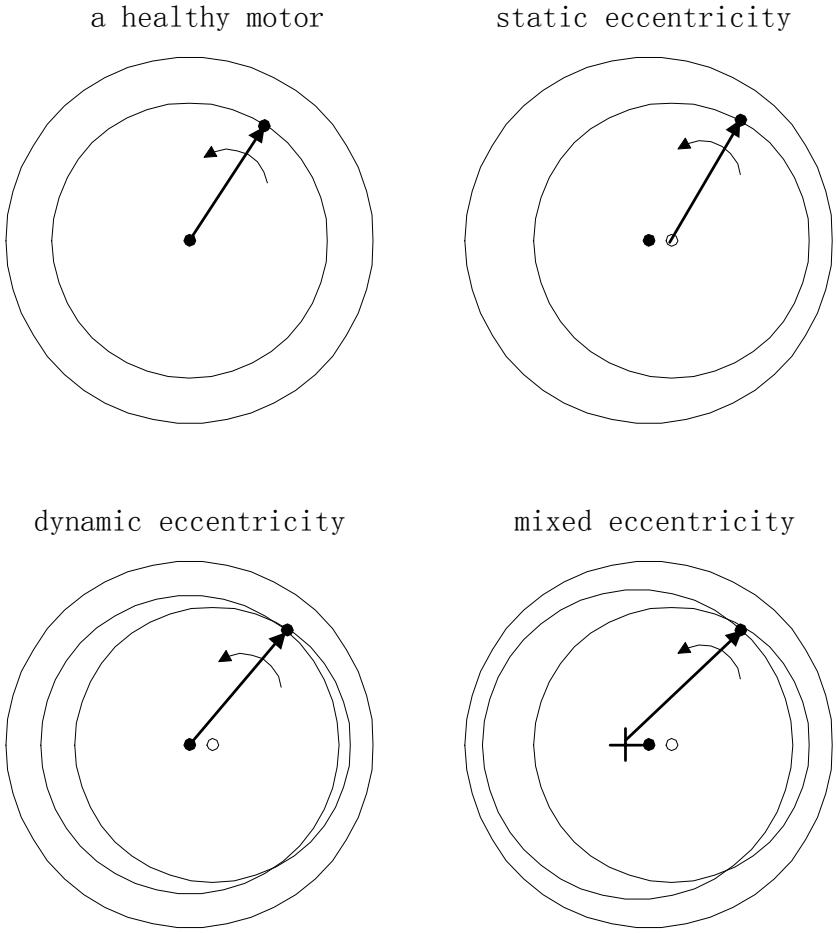

Figure 1.1. Static and dynamic eccentricity of induction motors.

In addition to flaws in the assembly and manufacturing processes, air gap eccentricity is also caused by external mechanical problems in induction motors, such as load unbalance, loose mounting, or shaft misalignment. These mechanical problems cause a radial unbalanced force on the rotor, which pulls the rotor from its normal position and generates a non-uniform air gap. These mechanical problems can be detected by monitoring the air gap [15, 54].

In practice, all three-phase induction motors contain inherent static and dynamic eccentricity. They exist simultaneously in practice and are referred to as mixed eccentricity [2, 18, 19, 28]. Air gap eccentricity causes a ripple torque, which further

leads to speed pulsations, vibrations, acoustic noise, and even an abrasion between the stator and rotor. Therefore, it is critical to detect air gap eccentricity as early as possible.

Among existing methods in induction motor condition monitoring, motor current signal analysis (MCSA) is the most commonly used technique. The advantages of this scheme include low cost and easy operation. In most applications, the stator current of an induction motor is readily available to protect machines against destructive over-currents, ground currents, etc. Therefore, an MCSA scheme can be implemented at no additional cost. For this reason, MCSA is often referred to as *sensorless* condition monitoring. Several industrial case studies based on MCSA are reported in the literature [4, 6, 9, 19], but the majority of the previous work deals only with line-fed induction motors.

The use of a motor drive adds several significant challenges to fault detection above and beyond those faced by conventional line-fed machines. First, the motor and drive operate in a closed-loop fashion. Therefore, their behavior is coupled and their fault signatures interact. Second, since the source of energy to the motor is not a sine wave voltage, the drive controllers modify the motor terminal quantities such as the current and voltage. In a line-fed motor, any change in air gap modulates the induced stator voltage and therefore shows up as harmonics in stator current. However, in a converter-fed motor, any closed-loop speed or current feed-back controller also affects the appearance of fault harmonics. Third, with an AC drive, the mechanical speed of an induction motor can vary widely. This changes the operating condition and eccentricity-related harmonic amplitudes. It is difficult or even impossible to formulate these relationships as strict analytical equations because they depend on several factors, such as installation, motor size, etc. In addition, it is impossible to measure fault harmonic

amplitudes corresponding to all the operating conditions since speed or load may change continuously. With the above problems, MCSA may no longer be sufficient because of the reduced sensitivity. Meanwhile, operating conditions must be considered in the fault detection [14, 47].

Together with the above problems in the diagnostics of induction motors in a closed-loop system, new detection techniques become possible. For example, in a line-fed machine, only motor terminal quantities, such as the stator current, are available for sensorless condition monitoring. However, in a drive-connected motor, many additional parameters of the motor and drive are readily available. These parameters contain fault signature information and can be used in developing an efficient and sensorless detection scheme.

1.4 Objective of the Research

This research focuses on the detection of air gap eccentricity in a three-phase induction motor supplied by a speed-controlled, current-regulated, indirect field-oriented drive. The objective is to design a practical detection scheme that can be adopted in future commercial drives.

Based on the discussion in Section 1.3, the detection scheme should meet the following requirements. First, it should be reliable and sensitive, which allows faults to be detected at an early stage before a catastrophic failure occurs. Second, the operation of the diagnostic scheme should require a minimum amount of expert knowledge. Although some commercial condition monitoring tools are on the market, most of them

provide only information such as the values of certain parameters or graphics of data, whose interpretation needs an experienced engineer. Too much expert knowledge involvement limits the applications of condition monitoring in practical applications, since in most cases experts are not available. An ideal condition monitoring tool should simply tell operators the condition of electrical machines. While it may not be able to predict the exact amount of remaining life, it is possible to notify operators when a potential fault is present so appropriate maintenance can be scheduled. Third, the diagnostic scheme should be cost effective. To have a detection scheme implemented in practical applications, avoiding expensive sensors and invasive operation is necessary.

This research proposes a detection scheme that is sensorless and intelligent and uses only readily available parameters. In the following chapters, the principles of this detection scheme are described. Simulation and experimental results demonstrate that the proposed scheme provides a reliable and accurate prediction about motor conditions over the entire range of operating conditions of experimental motors.

1.5 Outline of the Dissertation

A literature survey and review of previous work in induction motor condition monitoring is presented in Chapter 2. This chapter familiarizes readers with the research topic. The limitations of existing detection methods are analyzed in detail to clarify the motivation of this research.

Chapter 3 introduces the experimental setup. It describes the experimental equipment, such as the induction motor, load system, vector-controlled drive, and data

acquisition system. Furthermore, it explains the methods used to implement air gap eccentricity in induction motors.

Chapter 4 investigates the distribution of eccentricity-related fault harmonics between the stator voltage and current under the influences of drive controllers and mechanical load. First, a brief description of eccentricity-related fault harmonics in a closed-loop system is introduced. It helps understanding basic differences between fault detection for a line-fed induction motor and a drive-connected induction motor. Next, the effects of drive controllers on the distribution of fault harmonics are investigated, and a preliminary sensorless detection scheme is proposed. Finally, the influence of the mechanical load on the distribution of the fault harmonics is investigated. The preliminary detection scheme is modified to ensure good detection sensitivity and reliability. A direct time-stepping coupled finite element analysis (FEA) model is used to simulate air gap eccentricity in a closed-loop drive-connected induction motor. The model incorporates the effects of magnetic nonlinearity and space harmonics because of the machine magnetic circuit topology and winding layouts. Simulation and experimental results are presented to support the analysis and feasibility of the proposed detection method.

Based on the above analysis, Chapter 5 introduces a new detection scheme of air gap eccentricity using an artificial neural network (ANN). With a neural network, the variation of eccentricity-related harmonic amplitudes with changing operating conditions is incorporated into the fault detection. The performance of this detection scheme is tested over the entire range of operating conditions of experimental motors.

Chapter 6 investigates the effects of air gap eccentricity on surge test data. The experimental results show that air gap eccentricity can be unobtrusively observed in surge waveforms. With this observation, a new off-line method to detect rotor eccentricity faults in induction motors is proposed and experimentally validated.

Conclusions, contributions, and recommendations are discussed in Chapter 7.

CHAPTER 2

EXISTING METHODS IN INDUCTION MOTOR CONDITION MONITORING

This chapter reviews and summarizes existing methods in induction motor condition monitoring. The aim of this chapter is to provide theoretical foundations and to clarify the motivation of this research.

2.1 Noise Monitoring

Acoustic noise from air gap eccentricity in induction motors can be used for fault detection. Noise monitoring is accomplished by measuring and analyzing the acoustic noise spectrum. An example of using this method to detect air gap eccentricity is given in [42]. Ellison and Yang verified from a test carried out in an anechoic chamber that slot harmonics in the acoustic noise spectra from a small power induction motor were functions of static eccentricity.

However, the application of noise measurements in a plant is not practical because of the noisy background from other machines operating in the vicinity. This noise reduces the accuracy of fault detection using this method [22, 49].

2.2 Torque Monitoring

Almost all motor faults cause harmonics with special frequencies in the air gap torque. However, air gap torque cannot be measured directly. From the input terminals, the instantaneous power includes the charging and discharging energy in the windings. Therefore, the instantaneous power cannot represent the instantaneous torque. From the output terminals, the rotor, shaft, and mechanical load of a rotating machine constitute a torsional spring system that has its own natural frequency. The attenuations of the components of air gap torque transmitted through the torsional spring system are different for different harmonic orders of torque components. Generally, the waveform of the air gap torque curve is different from the torque measured at the shaft [16, 17]. Hsu [16] proposed a special method to detect cracked rotor bars, and stator unbalance caused by winding defects and unbalanced stator voltages using air gap torque. The air gap torque was presented by measurable motor terminal quantities as

$$Torque[Nm] = \frac{p}{\sqrt{3}}\{(i_A - i_B)\cdot\int[v_{CA} - R(i_C - i_A)]dt - (i_C - i_A)\cdot\int[v_{AB} - R(i_A - i_B)]dt\} \tag{2.1}$$

where i_A, i_B, and i_C are three-phase line currents of an induction motor, v_{CA} and v_{AB} are line-to-line voltages, R is half of the line-to-line resistance, and p is the number of pole-pairs. Frequencies of major torque harmonics associated with the above defects in induction motors are discussed for three extreme cases:

- Under normal operation:

$$\text{Angular frequency of torque}=0 \tag{2.2}$$

- With a single-phase stator:

$$\text{Angular frequency of torque} = -2\omega_s \tag{2.3}$$

- With a single-phase rotor:

$$\text{Angular frequency of torque} = 2s\omega_s \tag{2 .4}$$

where ω_s is the supply frequency in rad/s, and s is the slip. Therefore, the fault condition can be identified by monitoring the special harmonics in the air gap torque.

However, in equation (2.1) it is assumed that the magnetic paths of the three phases are identical. It is well known that only the interaction between stator currents and fluxes produced by rotor currents alone yields torque. Although the interactions between stator currents and fluxes produced by the same stator currents do not produce torque, those stator currents can affect the saturation of magnetic paths. Once the leakage reactances and magnetic paths of the three phases become asymmetrical, errors are induced and the calculation of air gap torque in equation (2.1) is no longer accurate [17].

Kral [33] proposed a current model and a voltage model to estimate the electromagnetic torque of an induction motor, which is called the Vienna Monitoring Method. The difference between the estimated torques from those two models gives an indication of the existence of broken bars.

2.3 Flux Monitoring

Air gap flux of induction motors contains rich harmonics. A flux monitoring scheme can give reliable and accurate information about electrical machine conditions. Any change in air gap, winding, voltage, and current can be reflected in the harmonic spectra.

Verma and Natarajan [43] studied the change of air gap flux as a function of static eccentricity. Binns and Barnard [44] monitored air gap flux and core vibration together, and concluded that the use of the two signals provided useful information for machine analysis. But this research only identified the parameters that were certainly functions of air gap eccentricity, rather than directed to the development of on-line diagnostics [49]. Thomson, Rankin, and Dorrell [49] analyzed the respective relationships among air gap flux, stator current, vibration signal, and air gap eccentricity by strict analytical equations. They derived the frequencies of eccentricity-related harmonics in the air gap flux to be

$$f_{ecc} = f_1[(R \pm n_d)\frac{1-s}{p} \pm n_w] \tag{2.5}$$

$$f_{ecc} = f_1 \pm f_m = f_1(1 \pm \frac{1-s}{p}) \tag{2.6}$$

where equation (2.5) is for static or dynamic eccentricity alone, and equation (2.6) is for mixed eccentricity, f_1 is the supply frequency, R is the number of rotor bars, n_d is the eccentricity index that is equal to zero for static eccentricity and one for dynamic eccentricity, n_w is equal to 1, 3, 5, … which is always chosen as one since these

harmonics are the largest and easiest to monitor, f_m is the rotor mechanical frequency, s is the slip, and p is the number of pole-pairs.

Air gap flux can be measured by search coils installed in the stator core. Because of the enclosed structure of induction motors, this operation requires the disconnection of induction motors from the main supply before dismantling. As such, this is neither practical nor economical for the motors that are already in service. In addition, because of the small air gap in most induction motors, installation of search coils may require significant design modifications that may not be easy to implement and certainly would be expensive.

2.4 Vibration Monitoring

Extensive work has been done in the detection of motor faults by monitoring unbalanced magnetic pull and vibration. The basic idea is that different mechanical faults create unique harmonics with different frequencies and power levels in the vibration signal. Thus, the vibration signal is first collected via a vibration sensor mounted on the stator frame, and then its spectrum is calculated using the fast Fourier transform (FFT). Specific harmonics are then monitored to determine the corresponding motor faults.

Cameron, Thomson, and Dow [49] verified that air gap eccentricity resulted in vibratory harmonics at frequencies of f_m, $2f_m$, $3f_m$, or $4f_m$. Riley, Lin, Habetler, and Kliman [45, 46] identified that there was a monotonic relationship between RMS vibration sum and RMS current sum at a given frequency. This is because the

mechanical vibration modulates air gap at that particular frequency. Those frequency components then show up in inductances and therefore in stator current.

The major weakness of vibration-based condition monitoring is its cost. The vibration sensor, especially the accelerometer, is expensive, and the acquisition of the vibration signal requires a significant investment.

2.5 Current Monitoring

The most economically attractive technology in induction motor condition monitoring is stator current monitoring. In most applications, the stator current of an induction motor is readily available since it is used to protect machines from destructive over-currents, ground current, etc. Therefore, current monitoring is a sensorless detection method that can be implemented without any extra hardware. There are three current monitoring methods: current Park's vector, zero-sequence and negative-sequence current monitoring, and current spectral analysis.

The basic idea of current Park's vector is that in three-phase induction motors, the connection to stator windings usually does not use a neutral. For a Y-connection induction motor, the stator current has no zero-sequence component. A two-dimensional representation of the three-phase currents, referred to as current Park's vector, can then be regarded as a description of motor conditions. Under ideal conditions, balanced three-phase currents lead to a Park's vector that is a circular pattern centered at the origin of coordinates, as shown in Figure 2.1. Therefore, by monitoring the deviation of current

Park's vector, the motor condition can be predicted and the presence of a fault can be detected.

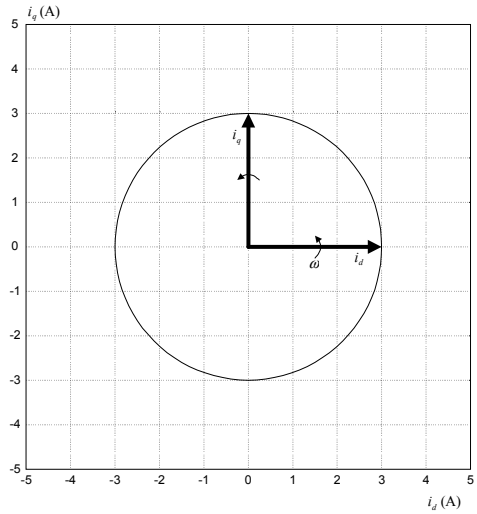

Figure 2.1. Stator current Park's vector of a healthy motor.

Cardoso and Saraiva [30, 31] used the Park's vector of the stator current to detect air gap eccentricity. Mendes and Cardoso [32] detected faults in voltage-sourced inverters using the current Park's vector. Nejjari and Benbouzid [29] analyzed the deviation in the pattern of current Park's vector to diagnosis the supply voltage unbalance of induction motors. However, this method ignores the non-idealities of electrical machines and inherent unbalance of supply voltages. In addition, it is difficult to isolate different faults using this method alone, since different faults may cause a similar deviation in the current Park's vector.

The zero-sequence and negative-sequence currents can be monitored to detect stator winding faults of electrical machines. Stator winding faults, such as turn-to-turn short circuit, can cause an asymmetrical electromagnetic field in electrical machines. This can create zero-sequence and negative-sequence currents, which cannot be observed in a symmetrical and healthy three-phase electrical machine. Similar to the current

Park's vector, this method is vulnerable to unbalanced voltages. Tallam, Habetler, and Harley [13, 53] monitored the negative-sequence voltage to detect a turn-to-turn short circuit in a closed-loop drive-connected induction motor. A neural network was used to learn and to estimate the negative-sequence voltage of a healthy motor, which is used as the threshold. This helped to reduce the effects of machine non-ideality and unbalanced supply voltage. According to [13], most of the turn-to-turn short circuit-related fault signatures exist in the stator voltage because of the regulation of the drive controllers. However, the influence of mechanical load was neglected. In practice, the distribution of fault information between the stator voltage and current depends on drive controllers, as well as mechanical load and operating conditions. Monitoring either stator current or voltage alone cannot ensure an accurate prediction of motor conditions.

Current spectral analysis, or MCSA, is the most commonly used method in the detection of rotor faults of induction motors. Broken bars cause special harmonics at the frequency given by equation (2.7) in the stator current [12, 21].

$$f_{bar} = f_1(1 \pm 2s) \tag{2.7}$$

where f_1 is the fundamental frequency of supply voltage, and s is the slip. Bellini *et al.* [12] investigated the impact of a closed-loop controller on the diagnostics of broken bars in induction motors. They proposed the use of the flux control current in a rotor-flux oriented synchronous reference frame, i_{ds}^e, as the diagnostic index. They assumed i_{ds}^e to be independent of control parameters and to depend on only the degree of asymmetry. But in their research, only a proportional speed controller was considered. Actually, i_{ds}^e

is also affected by i_{qs}^{e}, the torque control current. When an integral speed controller is present, i_{ds}^{e} becomes dependent on the speed bandwidth and therefore it is not the case that i_{ds}^{e} depends only on the asymmetry. Furthermore, the fault harmonics in i_{ds}^{e} are much smaller than those in i_{qs}^{e} in a field-oriented drive because the reference I_{qs}^{e} is the output of a speed controller, while the reference I_{ds}^{e} is a constant. The parameter i_{qs}^{e} contains larger fault harmonics because of speed feedback. Monitoring i_{ds}^{e} alone reduces the detection sensitivity.

As discussed in Section 2.3, the air gap eccentricity results in flux harmonics at the frequencies given by equations (2.5) and (2.6). As these harmonic fluxes move relative to the stator, they induce corresponding current harmonics at the same frequencies in a stationary stator winding [49]. Therefore, those current harmonics can provide an indication of motor health.

The voltage equations modeling an ideal induction machine in a stationary reference frame, assuming no neutral connection, are

$$\begin{cases} v_{qs} = R_s i_{qs} + \dfrac{d}{dt}\lambda_{qs} \\ v_{ds} = R_s i_{ds} + \dfrac{d}{dt}\lambda_{ds} \\ 0 = R_r i_{qr} - \omega_r \lambda_{dr} + \dfrac{d}{dt}\lambda_{qr} \\ 0 = R_r i_{dr} + \omega_r \lambda_{qr} + \dfrac{d}{dt}\lambda_{dr} \end{cases} \tag{2.8}$$

where v_{qs} and v_{ds} are stator voltages, R_s and R_r are stator and rotor resistances, i_{qs}, i_{ds}, i_{qr} and i_{dr} are stator and rotor currents, and ω_r is the rotor electrical velocity in rad/s. The stator and rotor flux linkages are given by

$$\begin{cases} \lambda_{qs} = L_s i_{qs} + L_m i_{qr} \\ \lambda_{ds} = L_s i_{ds} + L_m i_{dr} \\ \lambda_{qr} = L_r i_{qr} + L_m i_{qs} \\ \lambda_{dr} = L_r i_{dr} + L_m i_{ds} \end{cases} \tag{2.9}$$

where L_s and L_r represent the stator and rotor self inductances, and L_m represents the mutual inductance. If the stator voltage is assumed to vary sinusoidally in a line-connected induction motor and the stator copper losses are neglected, then it can be seen from equation (2.8) that the stator flux linkages oscillate at the fundamental frequency f_1. Since the stator flux linkages vary at a single frequency, equation (2.9) implies that any variation in the mutual inductance caused by air gap asymmetry may result in corresponding harmonics in the stator current.

Thomson [4, 5] verified that the use of the current spectrum was successful in diagnosing air gap eccentricity problems in large, high-voltage, three-phase induction motors. Benbouzid [23, 24] investigated the efficacy of current spectral analysis on induction motor fault detection. The frequency signatures of some asymmetrical motor faults, including air gap eccentricity, broken bars, shaft speed oscillation, rotor asymmetry, and bearing failure, were identified. His work verified the feasibility of current spectral analysis. Besides induction motors, current spectral analysis was applied to other types of electrical machines too. For example, Le Roux [60] monitored the

current harmonic component at the rotating frequency (0.5 harmonic) to detect the rotor faults of a permanent magnet synchronous machine.

Schoen and Habetler [7, 8] investigated the effects of a position-varying load torque on the detection of air gap eccentricity. The torque oscillations were found to cause the same harmonics as eccentricity. These harmonics are always much larger than eccentricity-related fault harmonics. It is therefore impossible to separate torque oscillations and eccentricity unless the angular position of the eccentricity fault with respect to the load torque characteristic is known [7, 8].

In current spectral analysis, the actual harmonics measured from a running machine are always compared with known values (thresholds) obtained from a healthy motor. In practical applications, the thresholds change with motor operating conditions. Therefore, Obaid [14] proposed tracking the normal values of a healthy motor at different load conditions. For each load condition, a corresponding threshold was determined and compared with the on-line measurement to determine the motor condition.

Besides the traditional FFT technique in spectral analysis, other techniques in advanced digital signal processing and pattern recognition were applied to motor condition monitoring as well. Yazici and Kliman [11] monitored stator current and applied the short-time Fourier transform (STFT) to detect broken bars and bearing faults in induction motors. Their experimental results supported the advantages of STFT than the traditional FFT because of the non-stationary stator current in practical applications. Kliman and Song [65] used a wavelet analysis of the stator current to remotely monitor DC motor sparking. However, it is difficult to determine suitable wavelet functions if the motor operating conditions change frequently, as in a vector-controlled drive. Haji and

Toliyat [63, 64] used a Bayes minimum error classifier to detect eccentricity and broken bars in induction motors. They assumed that the fault signature had a normal distribution density function. However, the distribution parameters had to be determined empirically.

Unlike direct measurement, in model-based parameter estimation, the thresholds of a healthy motor can be calculated by simulation. Toliyat [62] used the Winding Function Approach (WFA) to simulate an induction motor. The basic idea is to replace the squirrel-cage rotor by *n* independent loops, where *n* is the number of rotor bars. Then, the inductances of the *n* rotor loops and *m* stator phases can be calculated from the MMF, permeance, and air gap. Once the inductances are known, motor current and torque can be calculated. The WFA was applied to detect air gap eccentricity fault in induction motors [18, 19, 20] and in a synchronous machine [61]. Nandi [18] simulated a three-phase induction motor using the WFA and found that rotor slot and other eccentricity-related harmonics in stator current depended on the structure of rotor cage. In order to observe static or dynamic eccentricity-related components in stator current, the number of rotor bars *R* needs to be equal to

$$R = 2p[3(m \pm q) \pm r] \pm k \tag{2.10}$$

where $(m \pm q)$=0, 1, 2, 3, … and r=0 or 1, k=1 or 2.

The finite element analysis is another popular method to simulate electrical machines. Thomson and Barbour [3, 6] used the FEA to predict the level of static eccentricity in three-phase induction motors. Their investigation showed that those predictions were much closer to the measured values in comparison to previous attempts

using the classical MMF and permeance wave approach. Demerdash and Bangura [26] calculated eccentricity-related current harmonics of a squirrel-cage induction motor using a time-stepping coupled finite element state-space method. In their research, the authors calculated the electromagnetic field of an induction motor by FEA at each step in rotation. However, they only considered a motor supplied by an open-loop v/f adjustable-speed drive. For all model-based parameter estimations, diagnostic reliability heavily depends on the accuracy of the model. However, in most applications, accurate parameter information for the electrical machines or drives is not available. It limits the implementation of model-based parameter estimation in practical applications.

Rapidly evolving computing power and continual progress in ANN technology provide new tools for detection automation. Many different ANN-based detection methods were developed and implemented [34-41]. References [36, 37] proposed the use of a fuzzy or neural/fuzzy system to detect motor insulation problem. Such a system helps to give exact reasons for an abnormal phenomenon. But it is difficult to establish suitable fuzzy rules. References [35, 38] used a self-organizing map (SOM) to detect faults by distinguishing a fault pattern from an acquired normal pattern. But it is difficult to find an effective induction rule. That is, although a deviation pattern appears, it is hard to decide whether it is due to the expected fault.

2.6 Conclusions

This chapter presented a review of existing induction motor condition monitoring methods. It has been a broadly accepted requirement that a diagnostic scheme should be

non-invasive and capable of detecting faults accurately at low cost. MCSA has become a widely used method because its monitoring parameter is a motor terminal quantity that is easily accessible. The other broadly accepted requirement is that the diagnostic scheme should require a minimum amount of expert knowledge.

Relatively little research has been done to detect air gap eccentricity faults in closed-loop drive-connected induction motors. Specifically, no work has been done to comprehensively analyze the effects of closed-loop drive controllers and the mechanical load on the detection of air gap eccentricity in induction motors. In this research, these effects will be analyzed in detail, and then a sensorless and reliable diagnostic scheme will be proposed. Its feasibility will be validated experimentally.

CHAPTER 3

EXPERIMENTAL SETUP

To study air gap eccentricity and to test the proposed diagnostic scheme, an experimental setup is designed and built. Experimental results are used to explain test phenomena and to support the analysis in the following chapters. Therefore, it is important to describe the experimental setup at the beginning of this thesis.

3.1 Laboratory Test Equipment

This test setup consists of an induction motor, a commercial vector-controlled drive, a mechanical load, and a data acquisition system. The complete experimental setup is shown in Figures 3.1 and 3.2.

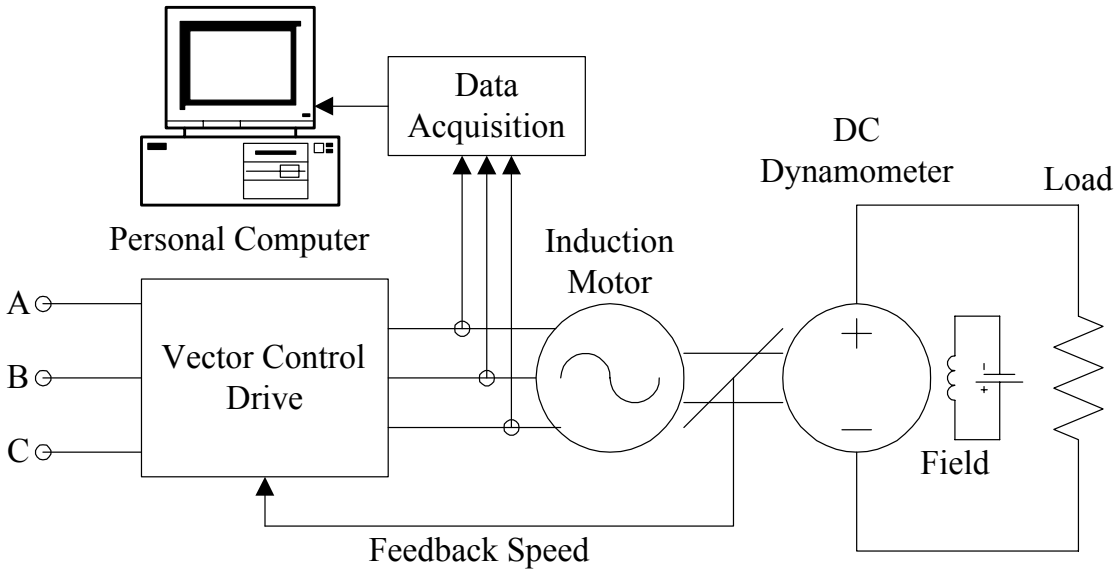

Figure 3.1. Diagram of the experimental setup.

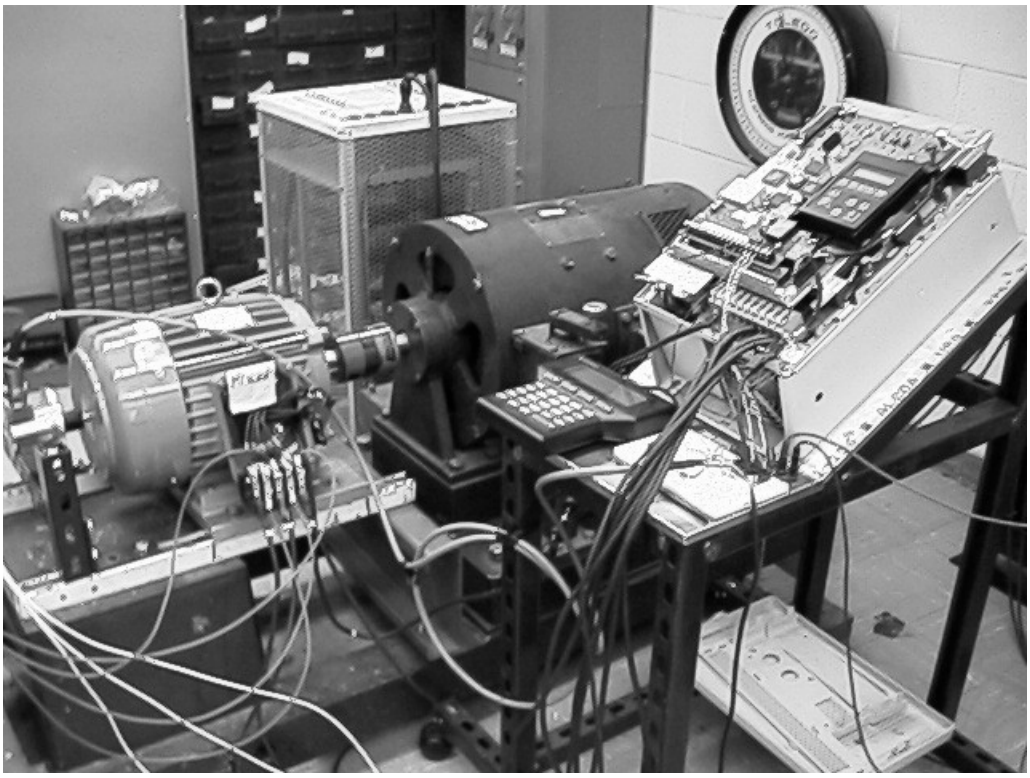

Figure 3.2. Experimental motor-drive system.

3.1.1 Motor and load

Three induction motors are used in this research. One is a healthy motor, and the other two motors contain static and mixed rotor eccentricity, respectively. All motors are 7.5 Hp, four-pole, three-phase induction motors. The main parameters of these motors are shown in Table 3.1.

The mechanical load consists of a DC dynamometer and a resistor bank. The dynamometer is a 10 Hp, 60 Amp, 3600 rpm, DC machine and is controlled by an adjustable 125 V DC supply, connected to its shunt field winding to vary the load on the test motor. The output of the DC dynamometer is connected to resistor banks, and the generated DC power is dissipated as heat.

Table 3.1. Parameters of experimental induction motor

HP	7.5	**Volt**	230
RPM	1755	**Ampere**	18.2
R1 (ohm @25C°)	0.174	**R2 (ohm @25C°)**	0.1597
L1 (mH)	1.3783	**L2 (mH)**	1.7592
Lm (mH)	52.7742	**Air gap length (in)**	0.014
# of stator slots	48	**# of rotor bars**	40

This mechanical load is actually a linear load, in which the load torque varies linearly with speed, and load power varies with speed squared, according to equations (3.1) and (3.2)

$$T_{load} = \frac{\left(k_a k_f i_f\right)^2 \omega_m}{R_a + R_L} \tag{3.1}$$

$$P_{load} = \frac{\left(k_a k_f i_f \omega_m\right)^2}{R_a + R_L} \tag{3.2}$$

where k_a, k_f are design constants of the DC dynamometer, i_f is the field current, ω_m is the mechanical speed, R_a is the armature resistance of the DC dynamometer, R_L is the load resistance, and P_{load} is the output power. Therefore, the load can be changed in three ways: varying motor speed, switching on/off the resistance bank, and adjusting field current. With i_f and ω_m fixed, the load power is increased when load resistance R_L is reduced, and the largest load power is reached when R_L is equal to the armature resistance R_a.

3.1.2 Vector-controlled drive

In the experiments, the induction motors are fed from a 460 V AC power supply through a commercial vector-controlled drive. Its main parameters are shown in Table 3.2.

Table 3.2. Parameters of the experimental AC drive

Input Volt	380-480 VAC	**Drive Hp**	20
Current Bandwidth	2000 rad/s	**Speed Bandwidth**	0-30 rad/s
Output Frequency	0-250 Hz		

The experimental AC drive is a high-performance, microprocessor-based, field-oriented AC drive. It is designed to be a low-cost drive for stand-alone applications and is user friendly besides having an easy-to-use start up sequence for simple, out-of-box installation. The micro-controlled field-oriented current loop has a fixed bandwidth of 2000 rad/s, which is not accessible to users. The customized parameters pertinent to the experiments in this research include reference speed and bandwidth of a digital speed loop. Before starting up, the drive goes through auto-tuning. Auto-tuning is a procedure that involves running a group of tests on the motor/drive combination. Some of the tests check the drive hardware, while others configure drive parameters to maximize the performance of the attached motor. The experimental AC drive uses auto-tuning to determine leakage inductance, stator resistance, flux current, and load inertia. All these parameters are then used to tune speed and current PI controllers. The drive also includes a user interface, through which users can control electric motors remotely. The experimental AC drive can work either in the speed-control or in the torque-control mode,

where the reference torque is calculated by a speed PI controller or fed from external control devices. In this research, the drive is always used in the speed-control mode.

Indirect field orientation requires a feed-back speed from an encoder mounted on the shaft. The experimental AC drive provides an optional board for the encoder interface. Motor speed is measured through an Allen-Bradley 845S incremental optical encoder installed on the motor shaft, as shown in Figure 3.3. Principles of an optical encoder are illustrated in Figure 3.4. The encoder is constructed with a light source, a sensor, a rotary disc, and a stationary mask. The rotary disk has alternate opaque and transparent sectors. As the disc rotates with shaft, the mask periodically passes and blocks light. The output signal from the sensor is used to decide the speed and direction of rotation.

3.1.3 Data acquisition and storage

Two types of signals are collected in the experiments: stator current and stator voltage via current sensors LEM® LA-55P and voltage sensors LEM® LV-25P, respectively. By appropriately choosing the measuring resistance, the ratios of current and voltage sensors are adjusted to be 10:1 and 100:1, respectively. Two phase currents and two line-to-line voltages are measured. Because the experimental motors do not have a neutral connection, the remaining third phase can be calculated from these two phase signals. Each of the signals measured is anti-alias low-pass filtered, amplified, and then simultaneously sampled through four channels of a data acquisition (DAQ) board and stored directly into a desktop computer. The whole system is shown in Figure 3.5.

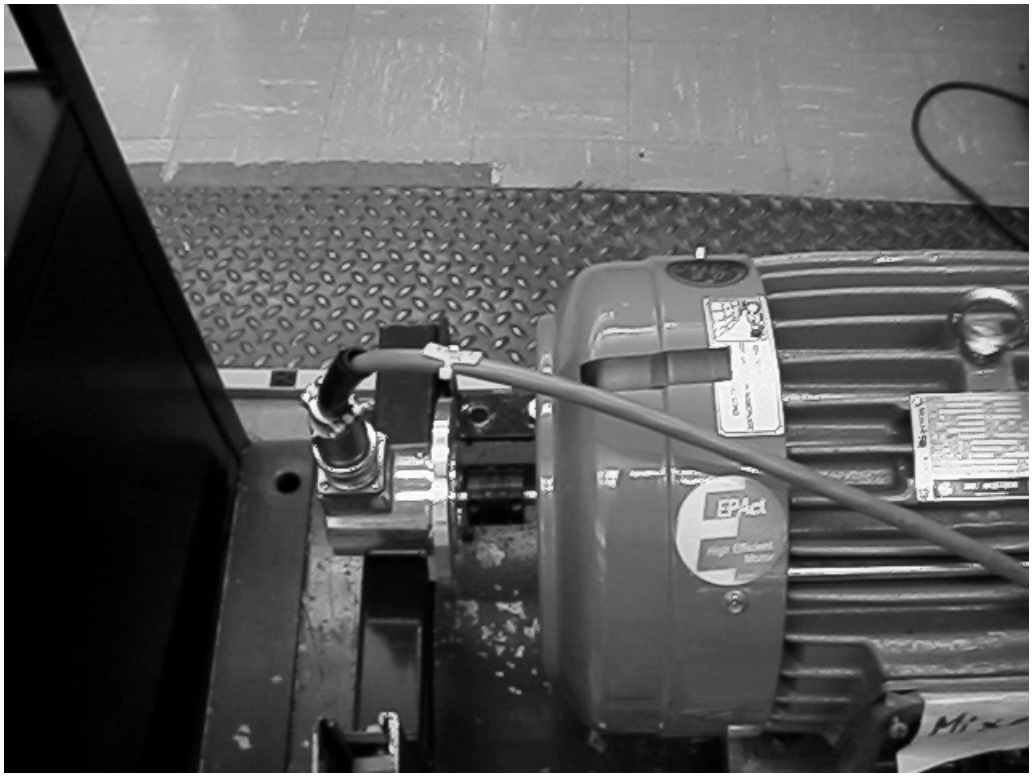

Figure 3.3. AB 845S optical encoder.

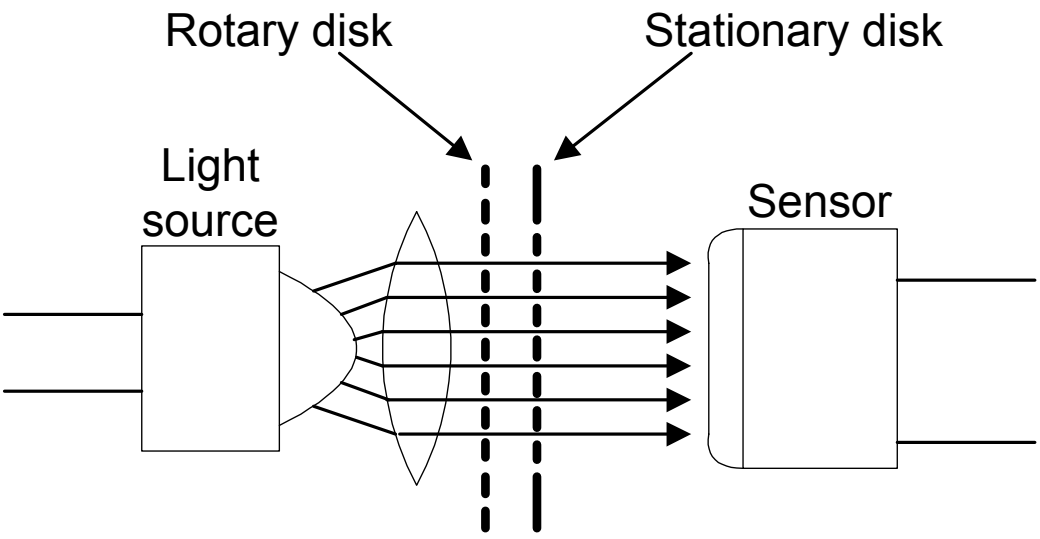

Figure 3.4: Principle of an optical encoder

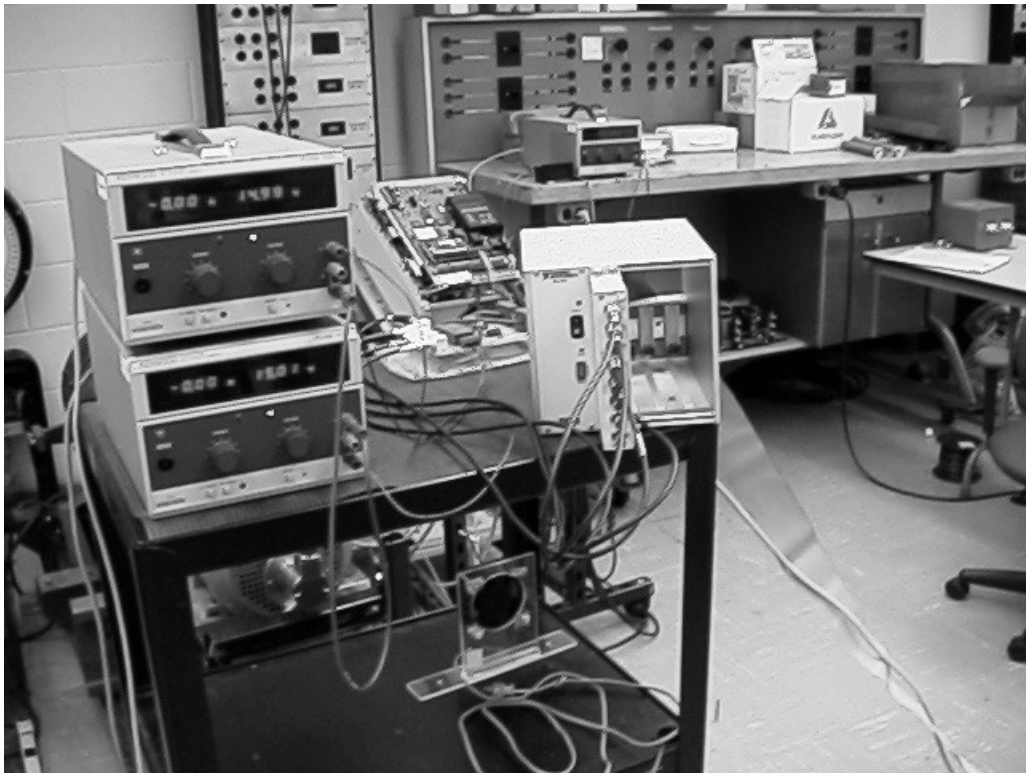

Figure 3.5: Data acquisition system

Experimental data are acquired by a National Instruments SCXI™ integrated measurement system. This system is composed of an SCXI™-1305 AC/DC coupling BNC terminal block, an SCXI™-1141 module, and an SCXI™-1000 chassis. The SCXI™-1305 block has eight BNC connectors and one SMB connector. Signal sources can be configured as either floating or ground referenced, and either AC or DC coupled. The SCXI™-1141 module has eight elliptic low-pass filters and eight differential-input amplifiers. The DAQ board PCI-6025E, cabled to the SCXI™-1141 module, reads the signal from each channel. The data acquisition process is controlled and monitored using National Instruments LabVIEW™ software. Once the data acquisition is complete, a Matlab® program is used to process and analyze the data.

3.2 Implementation of Air Gap Eccentricity

3.2.1 Implementing static eccentricity

As given in Table 3.1, the normal air gap between the stator and rotor in the experimental induction motors is small, which is 0.014 in (0.0356 cm). The small air gap makes it very difficult to implement rotor eccentricity. For example, at the beginning of the experiments, if there was air gap eccentricity, the rotor was always pulled onto the stator once the motor was energized because of the unbalanced magnetic pull (UMP). To solve this problem, the rotor has to be uniformly machined to 0.039 in (0.099 cm) to increase the air gap.

The parts of an induction motor are shown in Figure 3.6. The static eccentricity is created by first machining the bearing housing of one end bell eccentrically, and then inserting a 0.010 in (0.0254 cm) offset shim between the housing and the bearing [19, 28, 48]. In this way 25.6% static eccentricity is created.

3.2.2 Implementing dynamic eccentricity

Dynamic eccentricity is also created inside experimental motors in order to generate mixed eccentricity. Dynamic eccentricity is created by first machining the shaft under the bearing eccentrically, and then inserting a 0.015 in (0.0381 cm) offset sleeve between the bearing and the shaft. The degree of dynamic eccentricity is 38.4%.

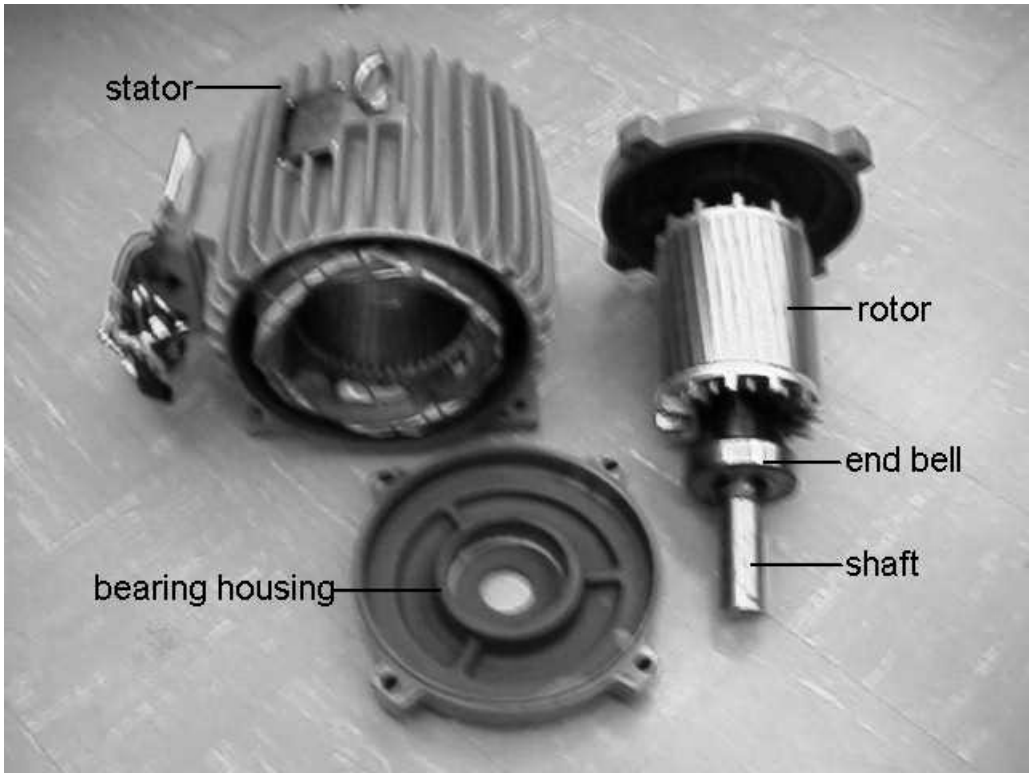

Figure 3.6. Components of induction motors.

3.3 Conclusions

This chapter introduced the experimental setup used in the experiments of this investigation. The experimental equipment was introduced. Methods used to implement static eccentricity and dynamic eccentricity were also described.

CHAPTER 4

DISTRIBUTION OF ECCENTRICITY-RELATED FAULT HARMONICS

This chapter first describes eccentricity-related fault harmonics in a closed-loop motor-drive system. The effects of the drive controllers and the mechanical load on the distribution of fault harmonics between stator voltage and current are analyzed next. Finally, the analysis is verified by simulation and experiments.

4.1 Introduction

Vector-controlled drives calculate motor variables in a synchronous reference frame. In a synchronous frame, an induction motor can be modeled as

$$v_{qds}^{e} = r_s i_{qds}^{e} + j\omega_s \lambda_{qds}^{e} + \frac{d\lambda_{qds}^{e}}{dt} \tag{4.1}$$

$$T_{em} = \frac{3pL_m}{L_r} \lambda_{dr}^{e} i_{qs}^{e} \tag{4.2}$$

$$J_{eq} \frac{d\omega_m}{dt} = T_{em} - T_{load} \tag{4.3}$$

where v_{qds}^{e} is the stator voltage space vector, i_{qds}^{e} is the stator current space vector, λ_{qds}^{e} is the stator flux linkage space vector, λ_{qds}^{e} is the rotor flux linkage space vector, ω_s is the

synchronous electrical angular speed, T_{em} is the electromagnetic torque, p is the number of pole-pairs, J_{eq} is the equivalent load inertia, ω_m is the mechanical speed, and T_{load} is the load torque. With eccentricity, the air gap between the rotor and stator becomes non-uniform, which can be approximated by [49, 55]

$$g = g_0[1 - \delta_s \cos\theta - \delta_d \cos(\omega_m t - \theta)] \tag{4.4}$$

where g_0 is the normal air gap length, δ_s is the degree of static eccentricity, δ_d is the degree of dynamic eccentricity, ω_m is the mechanical speed, t is time, and θ is the angle measured from a base point. Air gap permeance is defined as

$$P = \frac{\mu A}{g} = \frac{\mu A}{g_0[1 - \delta_s \cos\theta - \delta_d \cos(\omega_m t - \theta)]} \tag{4.5}$$

where μ is the air gap permeability, and A is the air gap area. Since δ_d and δ_s are small, equation (4.5) can be approximated as

$$P = \frac{\mu A}{g} = \frac{\mu A}{g_0}[1 + \delta_s \cos\theta + \delta_d \cos(\omega_m t - \theta)] \tag{4.6}$$

Then, the field flux linkage is calculated as

$$\lambda = \int n \, d\phi = \int n \frac{\mu}{g} MMF \, dA \tag{4.7}$$

where *MMF* is the field magnetomotive force, and *n* is the turns function. In equation (4.2), eccentricity causes ripple torque, while in equation (4.3), the ripple torque, in turn, leads to a speed pulsation. Equations (4.4-4.7) show that air gap eccentricity results in harmonics in field flux linkage. With speed feedback and controller action, the eccentricity-related fault harmonics spread to the controller variables and the motor supply voltage. All the variables in the motor and drive contain fault information.

To be precise, for speed, electromagnetic torque, and the controller variables in a synchronous reference frame, the frequency of the main mixed eccentricity-related harmonics is given by equation (4.8), and the frequency of the main static eccentricity-related harmonics is given by equation (4.9)

$$f_{ecc} = f_m = f_1 \frac{1-s}{p} \tag{4.8}$$

$$f_{ecc} = f_1[(R \pm n_d)\frac{1-s}{p} \pm n_w - 1] \tag{4.9}$$

For motor terminal quantities in a stationary reference frame, the above harmonics are located at frequencies given by equations (4.10) and (4.11), respectively

$$f_{ecc} = f_1(1 \pm \frac{1-s}{p}) \tag{4.10}$$

$$f_{ecc} = f_1[(R \pm n_d)\frac{1-s}{p} \pm n_w] \tag{4.11}$$

4.2 Effects of Drive Controllers

A typical vector-controlled drive has two control loops, each with a PI controller, an inner current loop, and an outer speed loop, as shown in Figure 4.1. The vector-controlled drive calculates the spatial angular position of rotor flux from the feed-back speed and stator current. Then, the d-axis is aligned with the rotor flux, which is referred to as "field-orientation." In this way, sinusoidal variables are modulated to be DC, and the steady state error can be efficiently eliminated using PI controllers. Furthermore, the motor torque can be controlled by adjusting the decoupled flux current, i_{ds}^{e}, and the torque current, i_{qs}^{e}, so that vector-controlled drives can emulate the operation of DC drives. Because of its special configuration, a vector-controlled drive is also called a speed-controlled, current-regulated, indirect field-oriented drive.

The PI controller functions like a low-pass filter, and the bandwidth determines its regulation ability. The controller generates an effective control signal only when the input signal is inside its bandwidth. In practice, the speed bandwidth, BW_{ω}, is usually up to a few Hz because of the limited current capacity of the drive. The current PI controller forms the inner loop and its bandwidth, BW_I, is much larger. Therefore, the cascade controllers are able to respond correctly to smooth out the error [13, 56]. Regarding equations (4.8) and (4.9), there are three possible relationships between the controller bandwidths and the eccentricity-related frequencies:

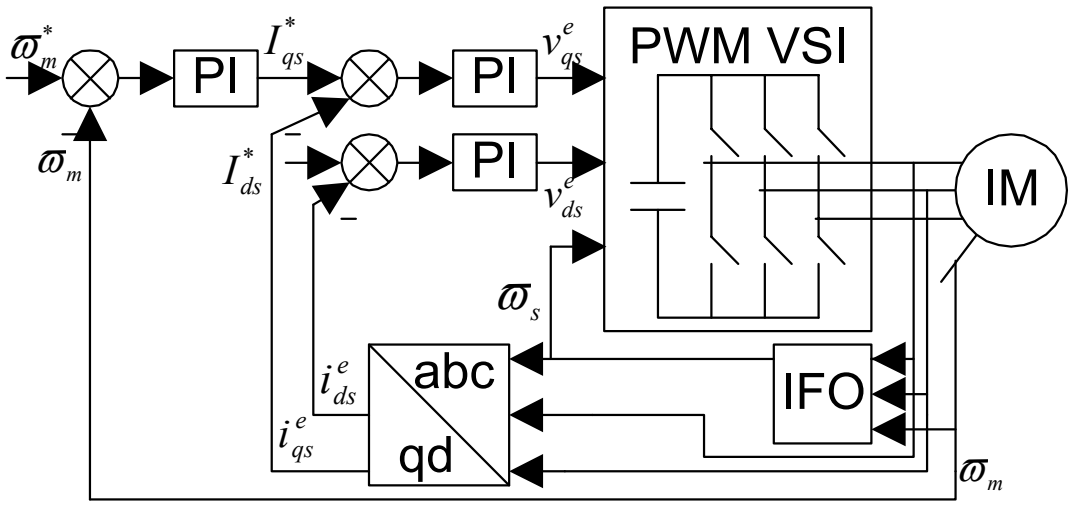

Figure 4.1. Block diagram of a speed-controlled, current-regulated, indirect field-oriented drive.

Case 1: $BW_I > 2\pi f_{ecc} > BW_\omega$

In this case, the speed pulsation resulting from air gap eccentricity is beyond the bandwidth of the speed controller, and the regulation ability of the speed controller is therefore weak. Ideally, the output of the speed controller, which is the reference torque current, contains only low-level eccentricity-related harmonics. The reference flux current is always a constant value except for operation in field weakening.

On the other hand, the regulation ability of the current controller is relatively strong. They force the actual stator current to track the references to contain low-level harmonics as well. Consequently, according to equation (4.1), through flux linkage, the harmonics in the non-uniform air gap will cause larger fault harmonics in the stator voltage. The fault harmonics in voltage or current are defined *large* or *small* with respect to the fundamental component and noise. Because the fault harmonics always have small magnitudes, larger harmonics are easier to monitor, and therefore detection reliability and sensitivity are improved.

Case 2: $BW_I > BW_\omega > 2\pi f_{ecc}$

In this situation, the regulation abilities of both the speed and current PI controllers are strong. The fault signal in the feed-back speed makes the speed PI controller output a corresponding control signal. Hence, the harmonic level of the motor current becomes higher. However, it is not a common case in practice since the speed bandwidth is fixed after installation. Its variation is limited even when adjusted manually.

Case 3: $2\pi f_{ecc} > BW_I > BW_\omega$

In this case, the regulation abilities of both the speed and current controllers are weak. The fault harmonics in the feedback speed are filtered by both the speed and current PI controllers. Only low-level harmonics exist in the motor voltage. This is equivalent to a line-fed motor, which means that most fault information exists in the stator current.

In most cases, except for operation at a very low speed, the mixed eccentricity of equation (4.8) always matches the first case, and the static eccentricity of equation (4.9) matches the third case. To detect mixed eccentricity, it is necessary to focus on monitoring voltage harmonics. Since voltage harmonics are larger than current harmonics, the detection is more sensitive and reliable. This explains why MCSA may be insufficient to detect rotor eccentricity in a closed-loop drive-connected induction motor. Similarly, when detecting static eccentricity, one should focus on monitoring current harmonics.

4.3 Effects of Mechanical Load

In practice, an induction motor is typically coupled to a mechanical load through a flexible coupling. At an early stage of rotor eccentricity faults, the shaft of the motor shifts from its normal position, while the shaft of the mechanical load is still fixed. The coupling between these two shafts actually allows a misalignment, as shown in Figure 4.2.

In rotation, the misalignment leads to a position-varying load torque given by

$$T_{load} = T_L + k\sin(\omega_m t) \tag{4.12}$$

where T_L is a constant load, k is the amplitude of the load oscillation caused by misalignment, and ω_m is the mechanical speed that is equal to $2\pi f_1(1-s)/p$. To compensate for this exterior load oscillation, the controllers command the motor to generate a corresponding torque component according to equation (4.2). Therefore, the special frequency components caused by the misalignment are at the same frequency as the eccentricity-related fault harmonics and overlap with each other [7, 8]. As torque is proportional to current using vector control, this misalignment increases the current harmonics and may even make the current harmonics larger than the voltage harmonics.

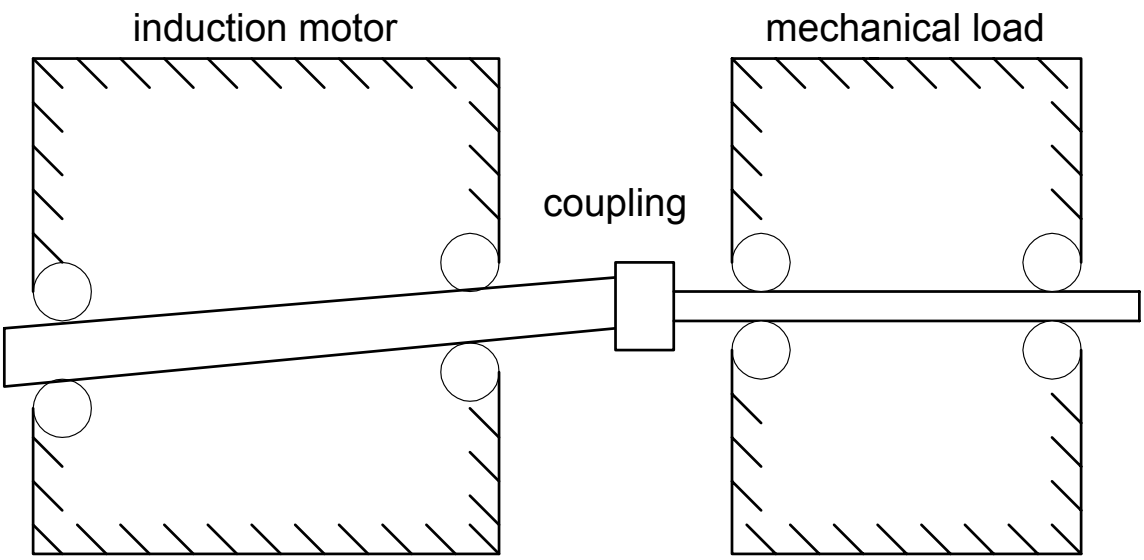

Figure 4.2. Coupling between an induction motor and a mechanical load in case of rotor eccentricity.

In summary, the distribution of eccentricity-related fault harmonics between the stator voltage and current depends on the drive as well as the mechanical load. Either voltage or current may contain larger fault harmonics. Reliable fault detection cannot be achieved based on just monitoring one parameter. In addition, in some applications, especially small induction motors, the actual motor terminal voltages are not readily available. Instead, the voltage space vector, v_{qds}^{e} , which is available in the drive controllers, can be used as the monitoring parameter. Therefore, a combination of monitoring voltage and current space vectors together, i.e., v_{qds}^{e} and i_{qds}^{e}, is able to ensure good detection sensitivity and reliability. Since both space vectors are readily available in the drive controllers, this diagnostic scheme is sensorless and will not add any extra cost to the existing instrumentation system of the drive.

4.4 Modeling Air Gap Eccentricity in Closed-Loop Drive-Connected Induction Motors

4.4.1 Introduction

Two methods are commonly used to simulate air gap eccentricity in induction motors: the winding function approach (WFA) and finite element analysis (FEA) [3, 18-20, 26].

The idea of the WFA is first to model the air gap asymmetry by equation (4.4). Inductances of stator and rotor windings can then be calculated from the air gap, the turn function, the winding function, and the air gap area. Substituting the inductances into voltage and flux linkage equations, (2.8) and (2.9), which model an induction motor, any fault signal in the motor terminal quantities can be calculated. Once the inductances are determined, the simulation can be done by any computational software, such as Matlab® or Simulink®. Readers can refer to the references [18-20] for more detail of this simulation method. The weakness of WFA is its accuracy. For example, WFA cannot simulate magnetic nonlinearities in the stator or rotor. Generally, the nonlinearities can only be approximated by Carter's coefficient. In addition, it is impossible to analyze an air gap asymmetry caused by stator slots and rotor bars, since the surfaces of stator and rotor are treated as smooth and circular in WFA.

FEA is another common simulation method for air gap eccentricity in electrical machines [3, 26]. FEA can incorporate the effects of magnetic nonlinearities and space harmonics because of machine magnetic circuit topology and winding layouts. The basic idea of FEA is to divide the whole motor, including the stator, rotor, shaft, and air gap, into triangle or rectangular finite elements (FE). In each FE, the partial differential

equations that model the motor are replaced by linear interpolation functions. The linear interpolation functions within all FEs are solved together with the boundary conditions. Today, more and more commercial FEA software packages are on the market. They usually provide a friendly user interface so that customers no longer necessarily spend time writing their own code for analyzing a motor. Once several motor design parameters are determined, a motor model can be built up and numerical analysis can be conducted. In this research work, Ansoft® Maxwell 2D software is used to simulate air gap eccentricity in a closed-loop drive-connected induction motor.

4.4.2 Finite element analysis of induction motors

The flow chart of the simulation program is shown in Figure 4.3. First, an induction motor is designed using Ansoft® RMxrpt, which is electrical machine design software. The user must decide the design parameters. The RMxprt can then design the motor, calculate performance curves, output winding layout, and create a corresponding FEA model. The user-input design parameters include motor rated power, rated voltage, rated frequency, number of poles, stator material, number of stator slots, size of slots, stator winding layout, rotor material, number of rotor bars, size of bars, shaft material, and the size of the shaft. The main outputs from RMxprt include stator resistance, stator leakage reactance, rotor resistance, rotor leakage reactance, magnetic reactance, rotor lamination geometry, and various motor performance curves.

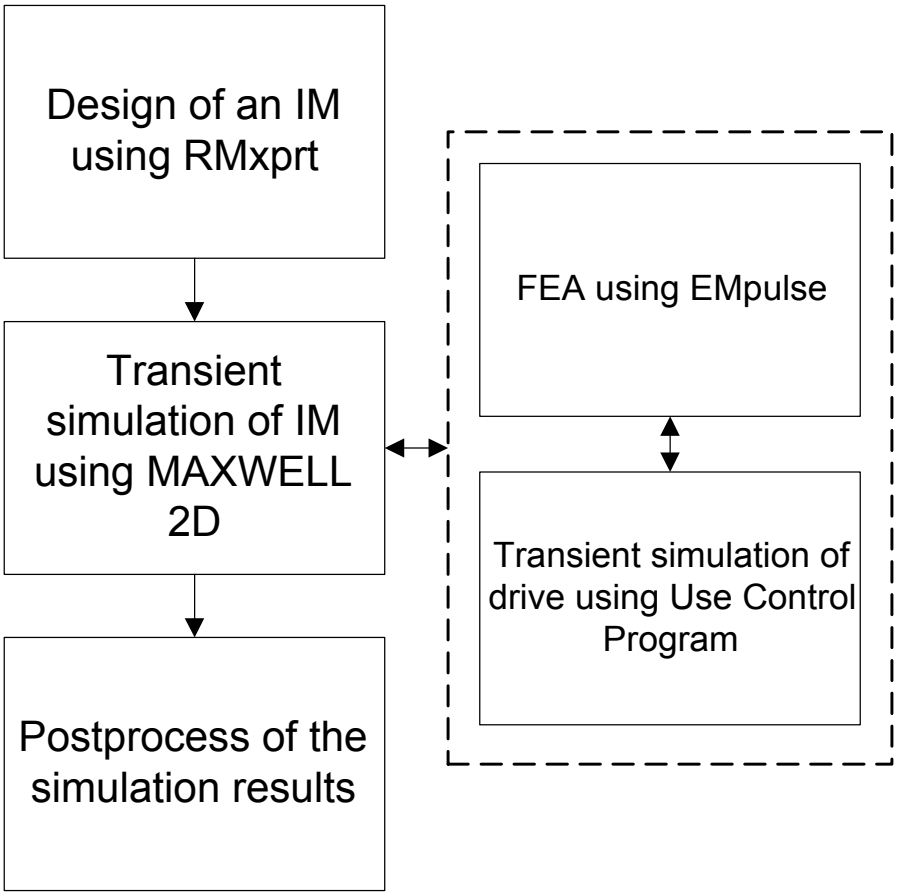

Figure 4.3. Flow chart of the simulation program.

In this research, a 70.87 kW, 460 V, two-pole, three-phase induction motor is designed using Ansoft® RMxrpt. The 2D model of this motor can be seen in Figure 4.4. The shaft is the red center circle. The green cylinder, with the inner diameter the same as the diameter of the shaft, is the rotor material. The outer green cylinder is the stator. The lamination geometry of the motor is shown in Figure 4.5.

The stator has 36 slots with a double-layer, 60^{o} spread distribution winding. One pole pitch is 18 slots, since this is a two-pole machine. Each coil spans 16 slots, making this winding short-pitched by two slots. The coil sides belonging to the same phase have the same color, as seen in Figure 4.4. For example, the coil sides belonging to the a-

phase are all red, while the a-phase returning coil sides are orange. The motor has a squirrel-cage rotor with a total of 25 bars. The magnetic nonlinearities are simulated by defining the stator and rotor as nonlinear materials. Skewing is not considered. The typical performance curves of this induction motor are shown in Figures 4.6 to 4.10.

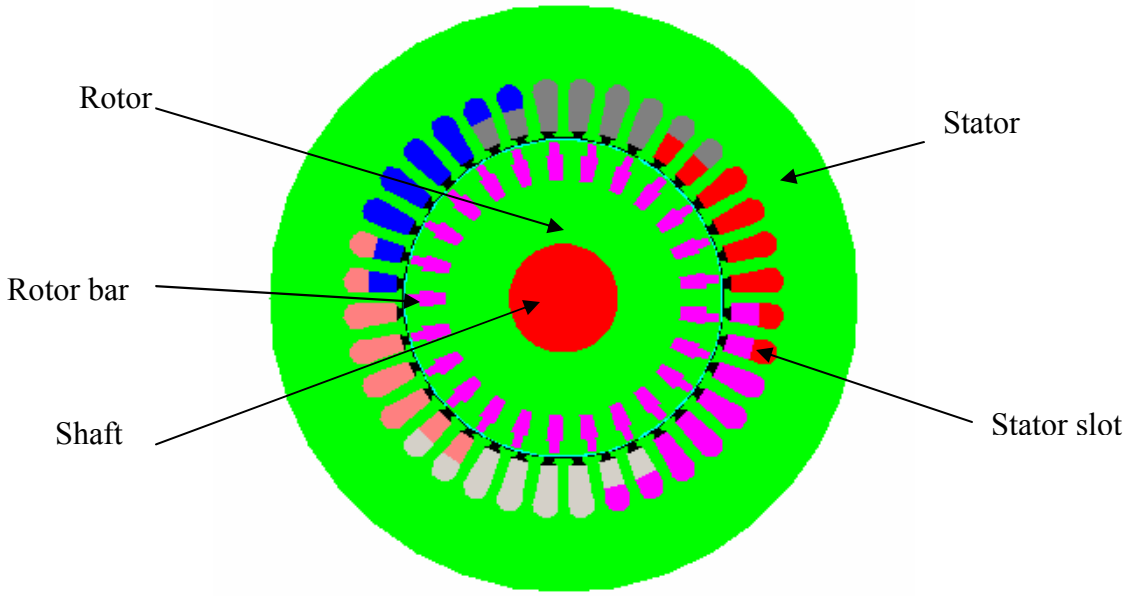

Figure 4.4. 2-D model of the simulation motor.

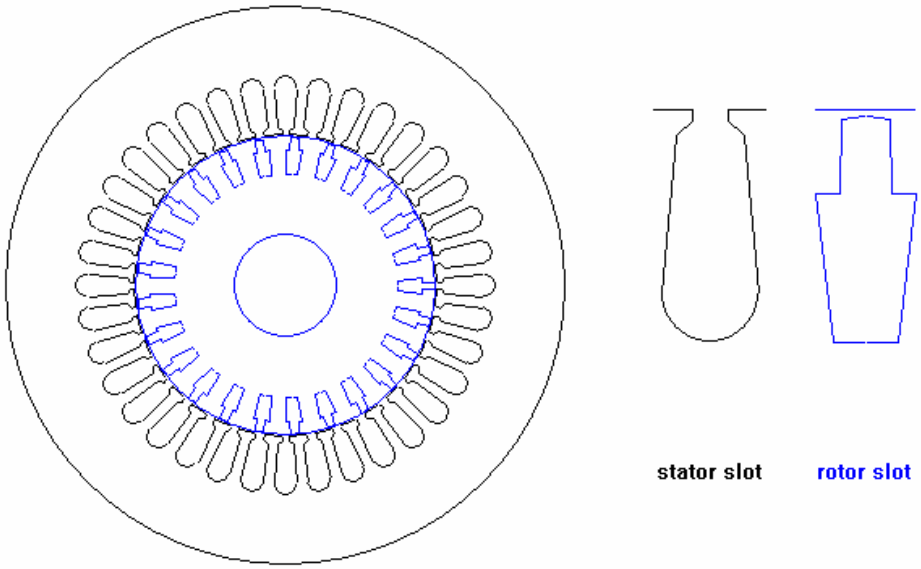

Figure 4.5. Lamination geometry of the simulation motor.

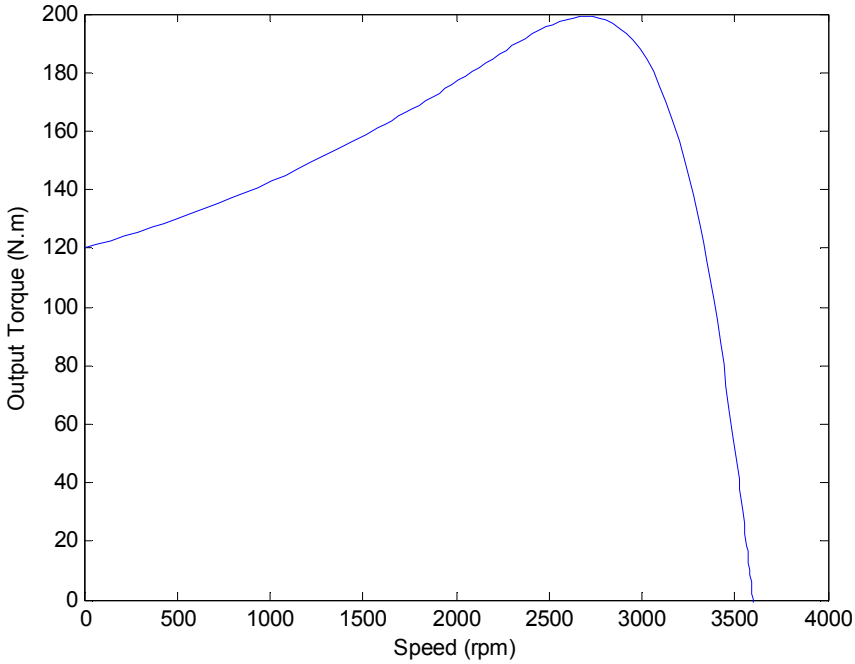

Figure 4.6. Performance curve of the motor in simulation: torque vs. speed.

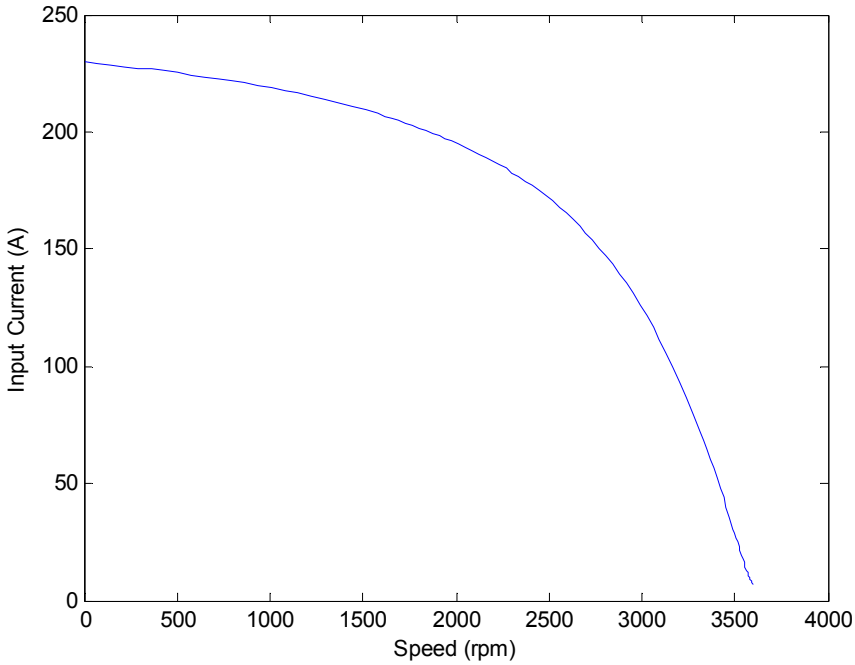

Figure 4.7. Performance curve of the motor in simulation: current vs. speed.

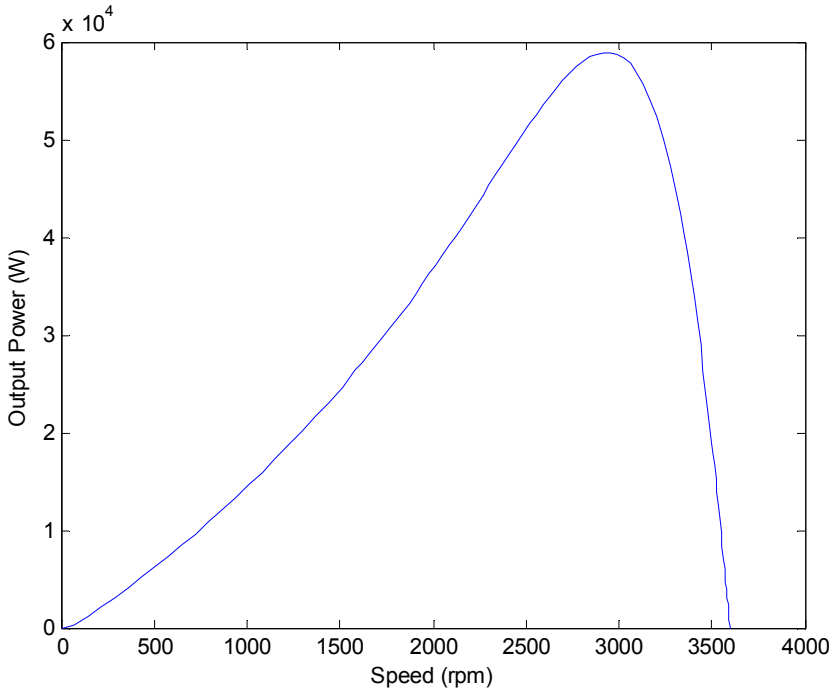

Figure 4.8. Performance curve of the motor in simulation: power vs. speed.

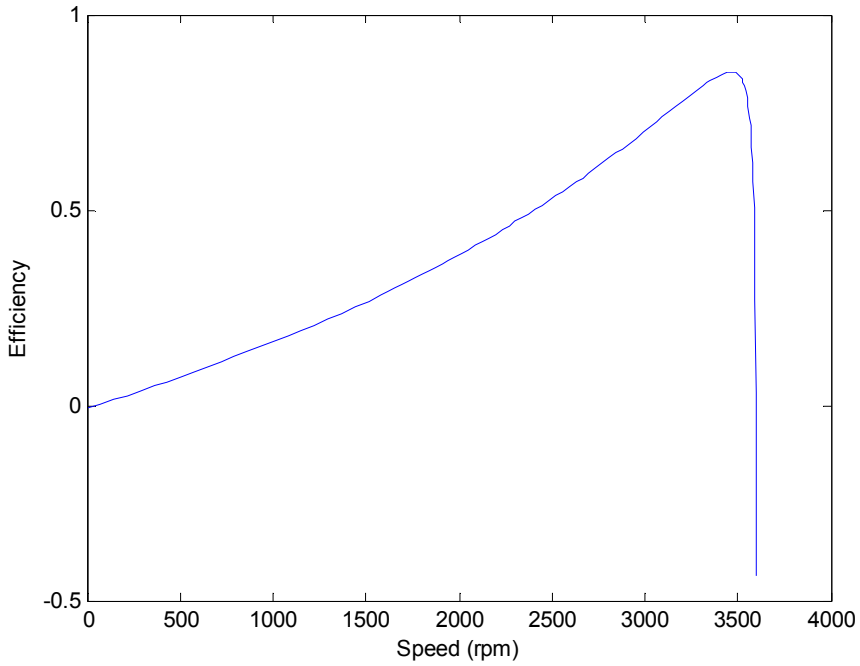

Figure 4.9. Performance curve of the motor in simulation: efficiency vs. speed.

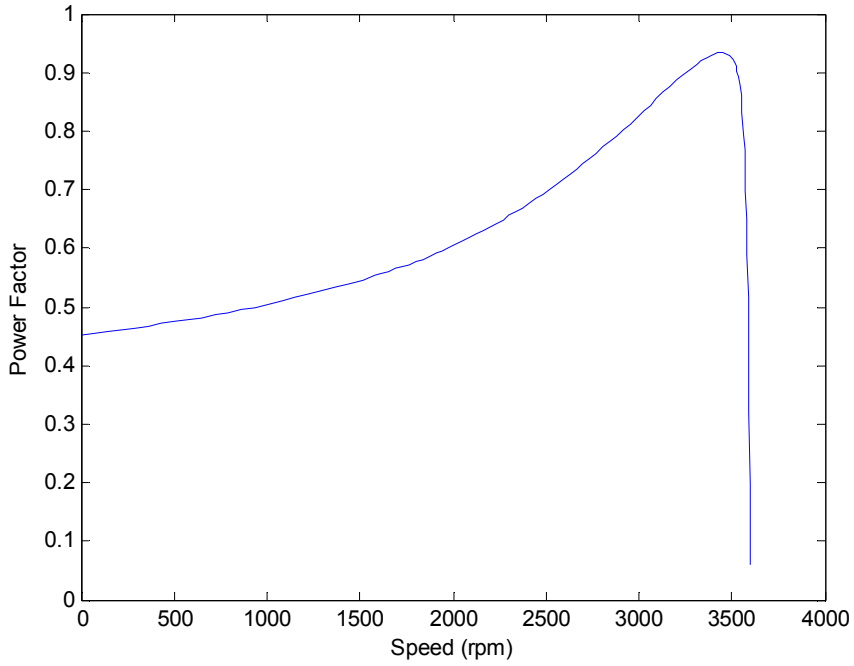

Figure 4.10. Performance curve of the motor in simulation: power factor vs. speed.

Once the motor is designed and a corresponding FEA model is created, the finite element analysis can be conducted in Maxwell 2D. To do this, material properties and excitation source need to be decided first. Then, Maxwell 2D works as follows, as shown in Figure 4.11:

- To create the required finite element mesh, either automatically or from user-defined seeding requirements;
- To iteratively calculate the desired field solution and special quantities of interest, including force, torque, current, and speed;
- With EMpulse, to simulate the transient motion of the system;
- To allow customers to analyze, manipulate, and display field solutions.

Maxwell 2D uses a software package called EMpulse to solve two-dimensional electromagnetic problems. EMpulse is a time-domain analysis software package that

solves coupled non-linear electromagnetic field, circuit, and motion problems using a time-stepping finite element approach. Air gap eccentricity can be implemented in simulation by moving the rotor and its rotational center from their normal positions.

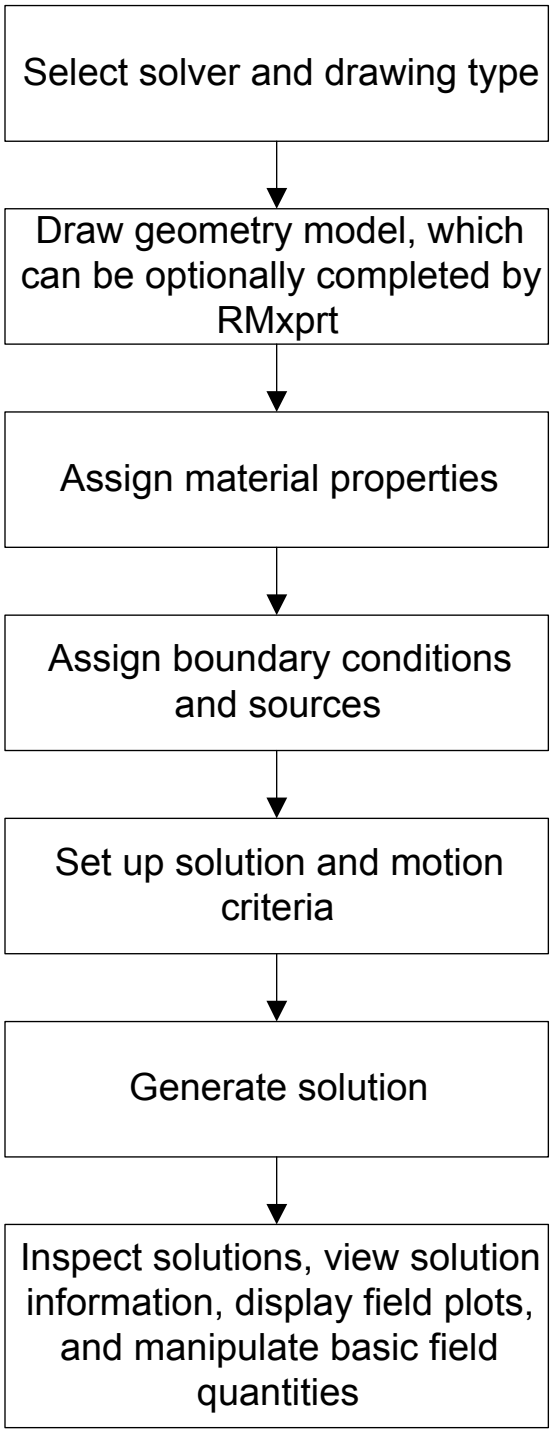

Figure 4.11. Flow chart of Maxwell 2D.

4.4.3 Modeling vector-controlled drives

EMpulse has the capability to interact with an external control program. This program can be written in any language such as Fortran, C, C++, Pascal. The only requirement is that the program must be compiled into an executable program. In this research, the vector-controlled drive shown in Figure 4.1 is simulated by a control program written in C language. The flow chart of this program is shown in Figure 4.12. At the first time step, EMpulse reads the values specified in Maxwell 2D material manager, boundary manager, and solve setup modules. After solving for the fields, EMpulse writes mechanical speed and stator current data to a file named solution.ctl and then calls the control program. The control program calculates the control variables and then writes the supply voltage data into a file called user.ctl. EMpulse reads the values from this file for the simulation of the next step. Once EMpulse finishes solving the fields, it copies the values from solution.ctl to a file called previous.ctl. Thus, the control program has access to the solutions of both the current time step and the previous time step [27, 59].

Switching harmonics in PWM are mainly located at

$$f_h = (jm_f \pm k) f_1 \tag{4.13}$$

where f_1 is the fundamental frequency, m_f is the frequency modulation ratio, and j, k are integers. Compared with equations (4.8) and (4.9), switching harmonics have much higher frequency than eccentricity-related harmonics. Therefore, in the simulation, the PWM voltage-sourced inverter is assumed ideal to save simulation time and memory.

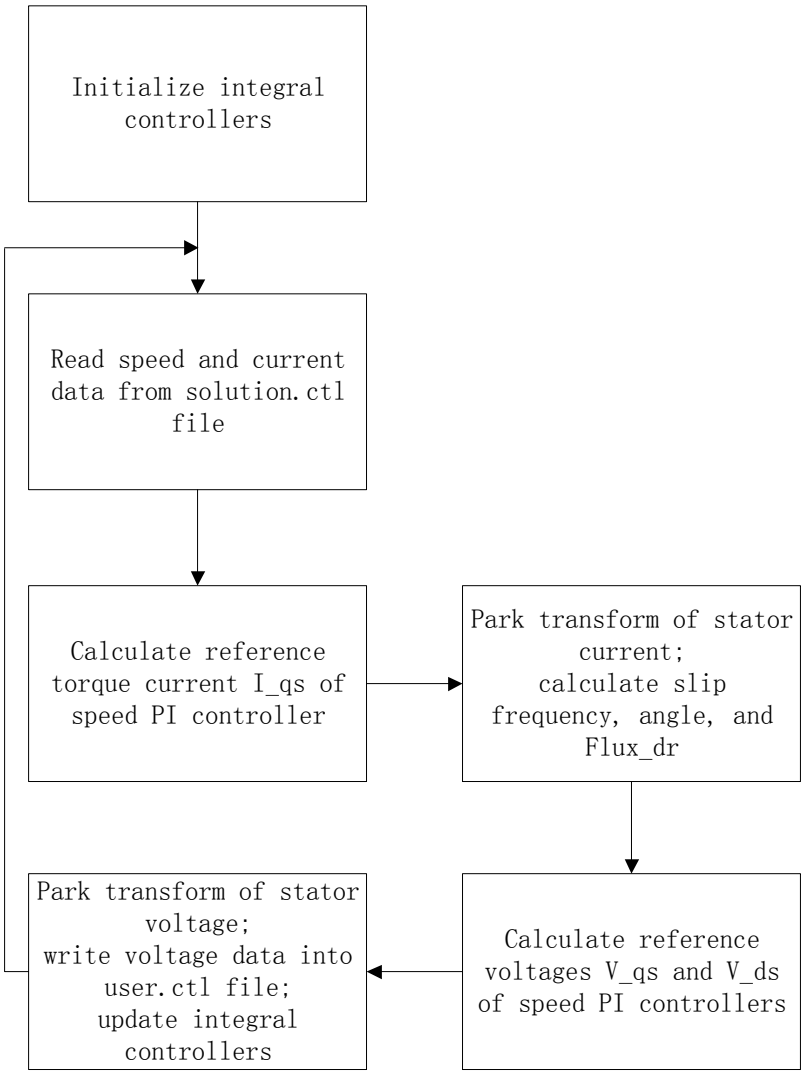

Figure 4.12. Flow chart of the drive control program.

The field orientation in vector control is calculated from the feed-back speed and stator current according to equations (4.14) to (4.16).

$$\lambda_{dr}^{e} = \frac{R_r L_m}{R_r + L_r P} i_{ds}^{e} \tag{4.14}$$

$$s\omega_s = \frac{R_r L_m i_{qs}^{e}}{L_r \lambda_{dr}^{e}} \tag{4.15}$$

$$\omega_s = s\omega_s + \omega_r = s\omega_s + p\omega_m \tag{4.16}$$

where P is a derivative operator, R_r is the rotor resistance, L_m is the magnetic inductance, L_r is the rotor inductance, and ω_r is the rotor electrical speed in rad/s. Parameters, such as L_m, R_r, the rotor time constant $\tau_r = L_r / R_r$, and the reference flux current, I_{ds}^*, are determined by the auto-tuning function of the drive. Particularly, τ_r is calculated from a single phase excitation test, R_r from a DC current test, L_m and I_{ds}^* from a no-load test. In the simulation, all the parameters are calculated in RMxprt.

The proportional and integral gains of the speed and current PI controllers are calculated from bandwidth (BW) and phase margin (PM) [56]. The design should begin from the inner current loop and work toward the outer speed loop.

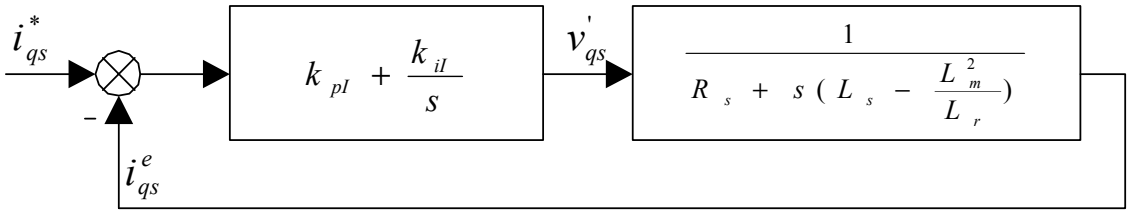

Figure 4.13. Design of current PI controller.

As shown in Figure 4.13, the open-loop transfer function of the current loop is

$$G_{I,OL}(s) = (k_{pI} + \frac{k_{iI}}{s}) \times \frac{1}{R_s + s(L_s - \frac{L_m^2}{L_r})} \tag{4.17}$$

where R_s is the stator resistance, and L_s is the stator reactance. The bandwidth and phase margin are equal to

$$\left|G_{I,OL}(jBW_I)\right| = 1 \tag{4.18}$$

$$\angle G_{I,OL}(jBW_I) = -180 + PM \tag{4.19}$$

Therefore, the integral and proportional gains are calculated to be

$$k_{iI} = BW_I \frac{\sqrt{R_s^2 + [BW_I(L_s - \frac{L_m^2}{L_r})]^2}}{\sqrt{\tan^2\{PM_I - \frac{\pi}{2} + \tan^{-1}[BW_I(L_s - \frac{L_m^2}{L_r})/R_s]\} + 1}} \tag{4.20}$$

$$k_{pI} = \frac{k_{iI}}{BW_I}\tan\{PM_I - \frac{\pi}{2} + \tan^{-1}[BW_I(L_s - \frac{L_m^2}{L_r})/R_s]\} \tag{4.21}$$

Since the current loop has a much larger bandwidth than the speed loop, once designed, the current loop can be considered an ideal transfer block in the design of the speed PI controller. The design of the speed loop is shown in Figure 4.14. Similarly, the integral and proportional gains can be calculated from bandwidth and phase margin as follows:

$$k_{i\omega} = \frac{BW_\omega^2 J_{eq}}{p \times \frac{L_m^2}{L_r} i_{ds}^* \sqrt{1 + \tan^2(PM_\omega)}} \tag{4.22}$$

$$k_{p\omega} = \frac{k_{i\omega}}{BW_{\omega}} \tan(PM_{\omega}) \tag{4.23}$$

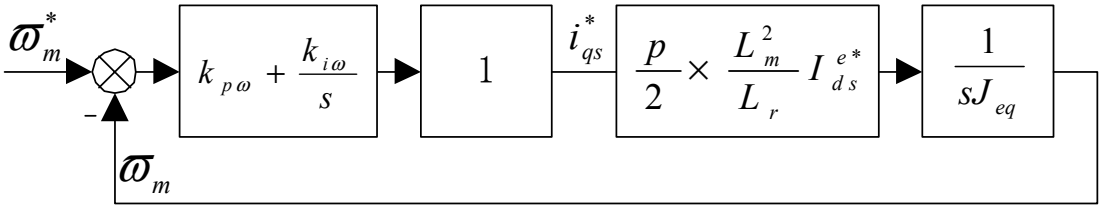

Figure 4.14. Design of speed PI controller.

It is noted that the above calculations use the Park transform given by

$$\begin{bmatrix} d \\ q \end{bmatrix} = \sqrt{\frac{2}{3}} \begin{bmatrix} \cos(\theta_{da}) & \cos(\theta_{da} - \frac{2\pi}{3}) & \cos(\theta_{da} - \frac{4\pi}{3}) \\ -\sin(\theta_{da}) & -\sin(\theta_{da} - \frac{2\pi}{3}) & -\sin(\theta_{da} - \frac{4\pi}{3}) \end{bmatrix} \begin{bmatrix} a \\ b \\ c \end{bmatrix} \tag{4.24}$$

where θ_{da} is the angle between the d-axis and stator a-axis. With different values of θ_{da}, the above integral and proportional gains will take on different forms.

4.5 Simulation Results

Four sets of simulation results are introduced: one for a healthy motor, one for a motor with a mixed rotor eccentricity fault, one for a motor with eccentricity and a position-varying load torque, and one for a motor with static eccentricity. In all four simulations, the reference speed is changed step-wise from zero to 3000 rpm at zero

seconds. The speed and current bandwidths of the drive are equal to 16 rad/s and 2000 rad/s, respectively.

4.5.1. Simulation of a healthy motor

In this simulation, a healthy induction motor drives a linear load whose torque is equal to $0.02n$, where n is the motor speed in rpm. The simulation results are shown in Figures 4.15 to 4.22.

Figures 4.15 and 4.16 demonstrate the motor start-up from standstill to a steady speed of 3000 rpm in around 1.5 sec. In Figure 4.17, the torque reaches a steady state value of 60 N·m, which is equal to the load torque. In Figures 4.18 to 4.20, the stator voltage, current, and flux linkage are shown to be symmetrical for a healthy three-phase induction motor. The controller variables, such as the flux and torque currents, and d-q reference voltages, are shown in Figures 4.21 and 4.22. They are modulated to be DC values in the synchronous reference frame. The controller variables contain harmonics even for a healthy motor because of the effects of stator slots, rotor bars, and non-sinusoidal windings.

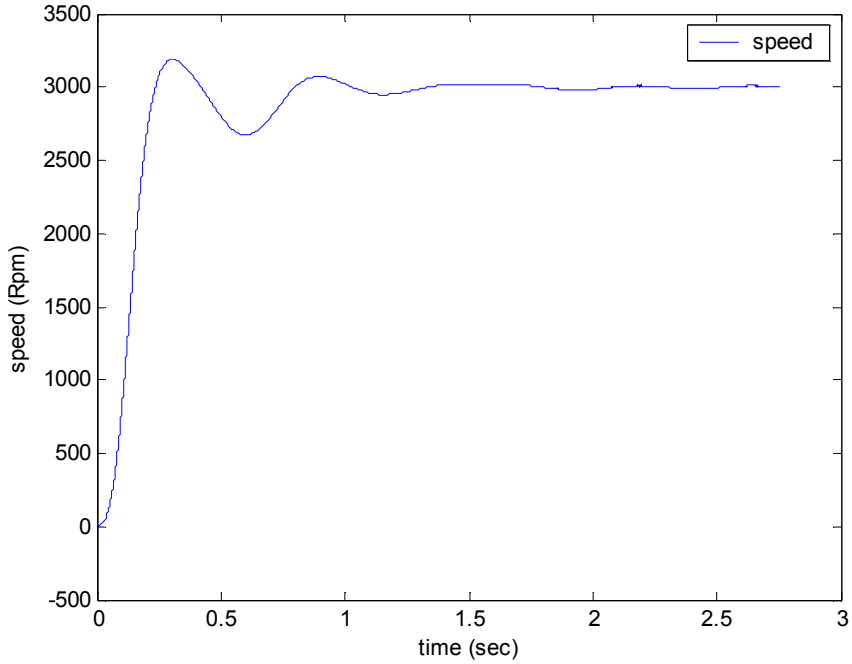

Figure 4.15. Simulated speed vs. time for a healthy motor.

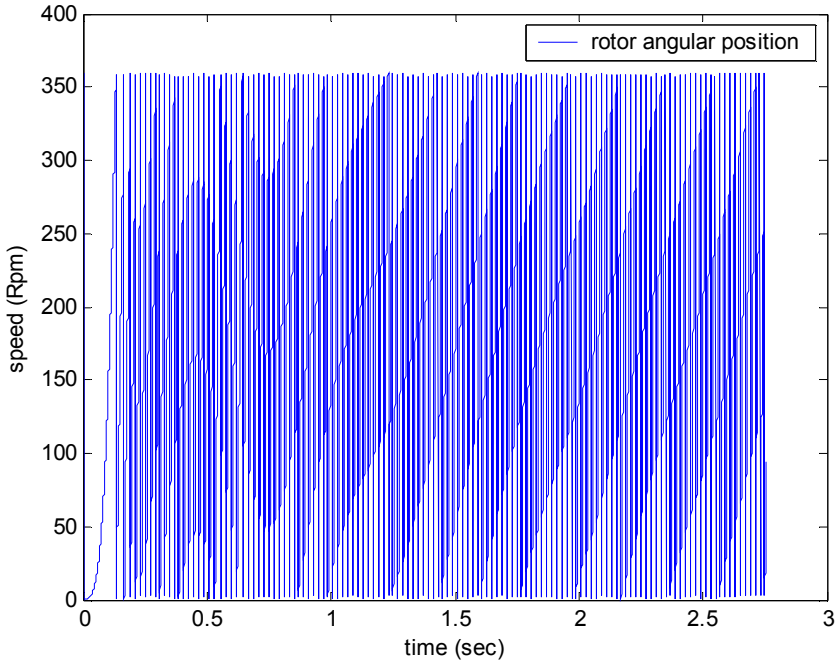

Figure 4.16. Simulated rotor position vs. time for a healthy motor.

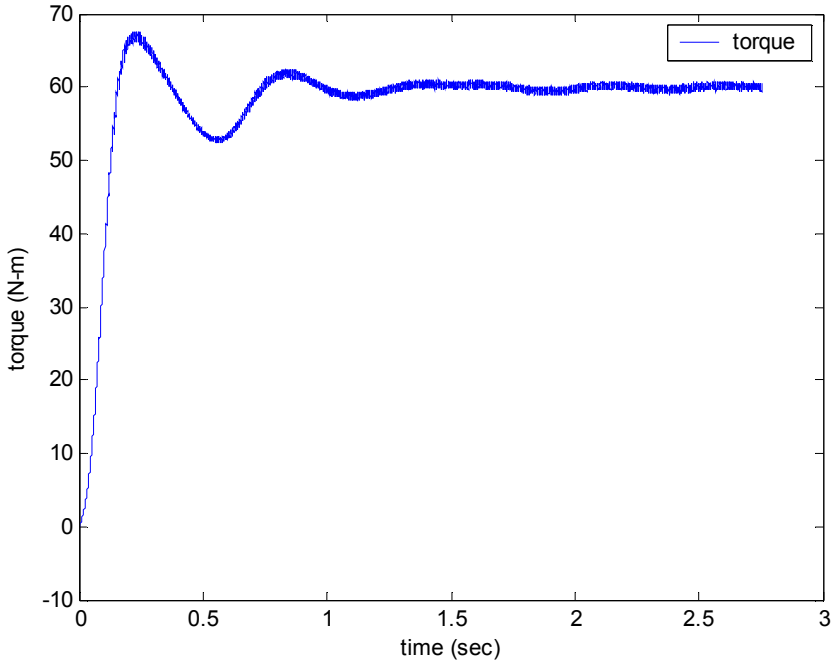

Figure 4.17. Simulated torque vs. time for a healthy motor.

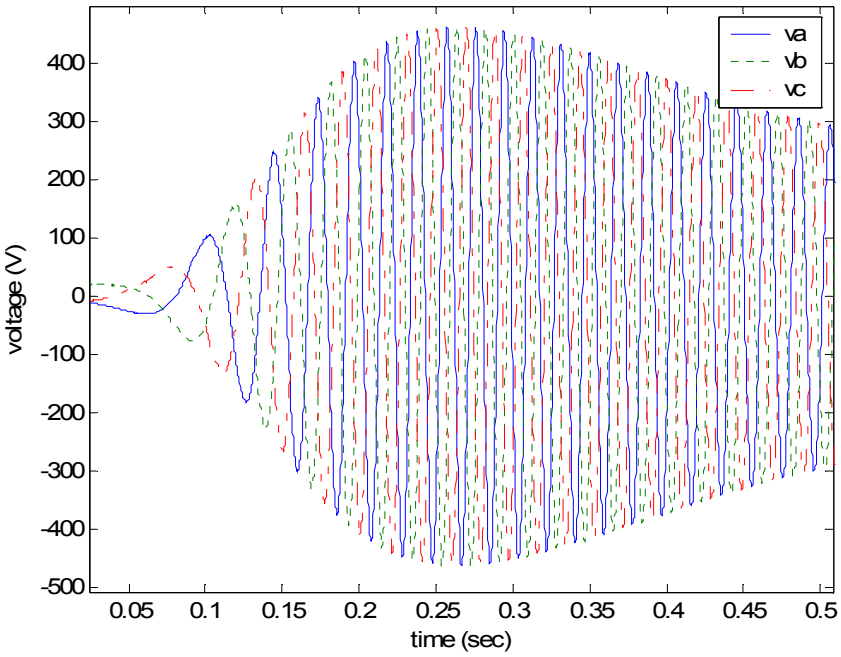

Figure 4.18. Simulated phase voltage vs. time for a healthy motor.

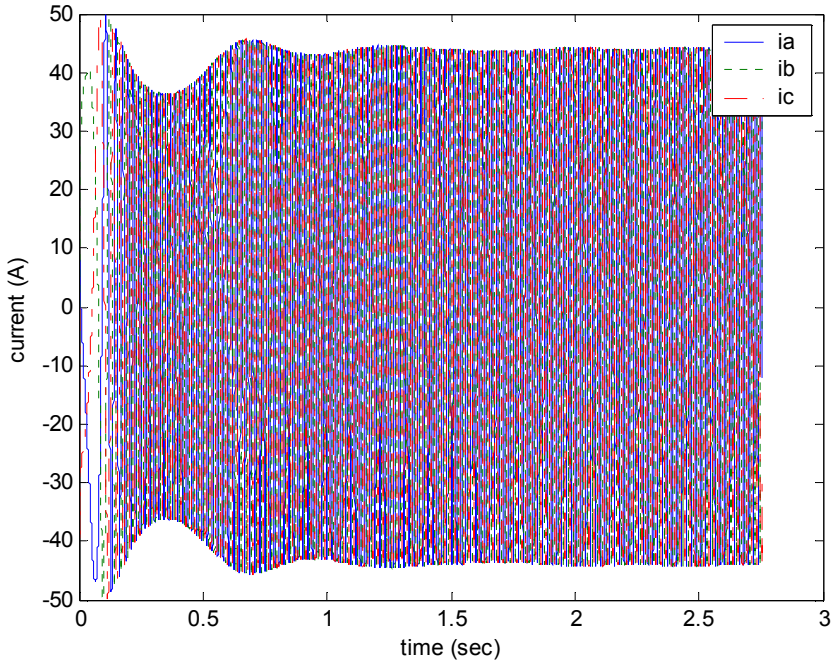

Figure 4.19. Simulated phase current vs. time for a healthy motor.

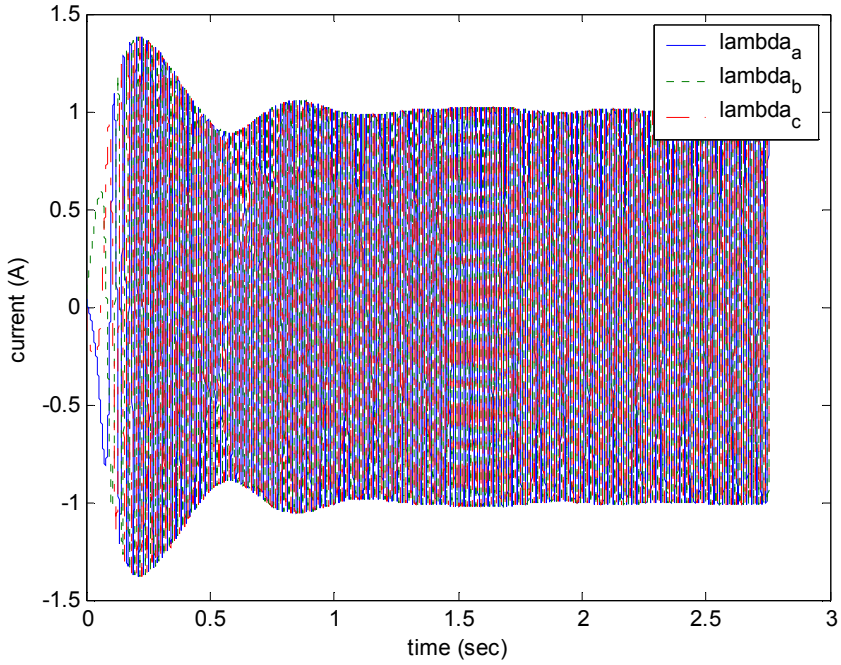

Figure 4.20. Simulated flux linkage vs. time for a healthy motor.

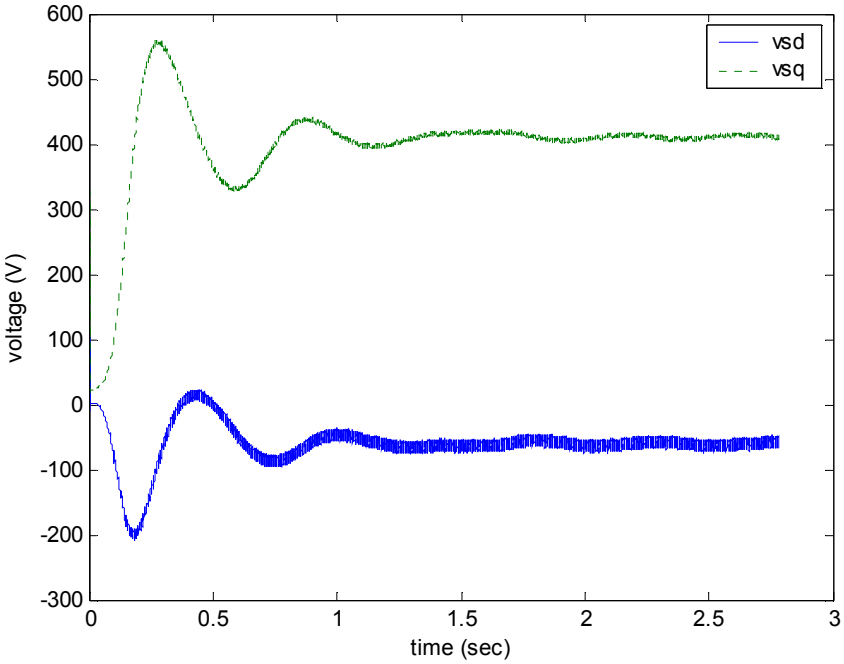

Figure 4.21. Simulated regulation voltage vs. time for a healthy motor.

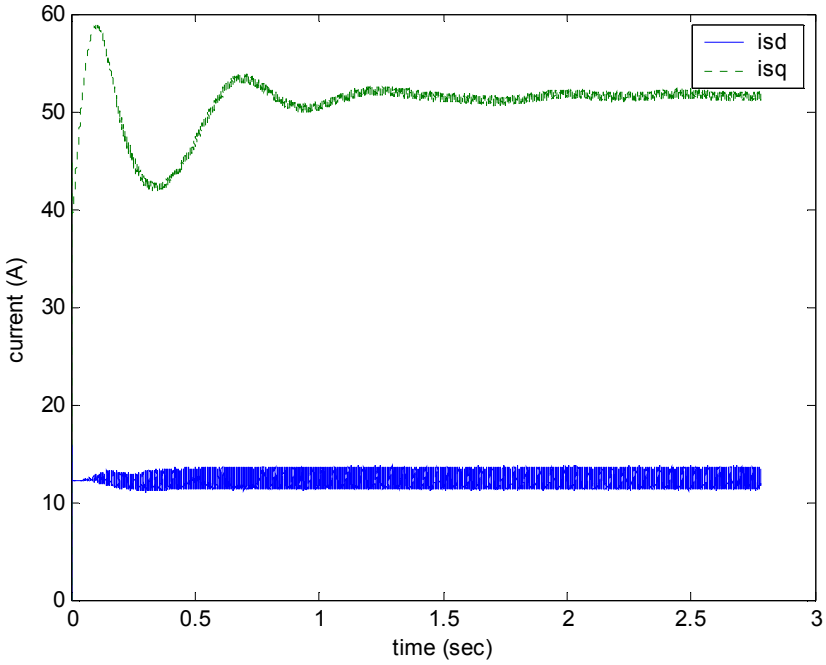

Figure 4.22. Simulated regulation current vs. time for a healthy motor.

4.5.2. Simulation of a motor with a mixed eccentric rotor

In the second simulation, a mixed eccentricity rotor is created by moving the rotor to left from its normal position by 10% of the normal air gap, and its rotational center right by 30% of the normal air gap. The motor is still driving the same load, whose torque is equal to $0.02n$, where n is the motor speed in rpm. The simulation results are shown in Figures. 4.23 and 4.24.

Compared to Figure 4.17, the torque contains more oscillation spikes in Figure 4.23 because of air gap eccentricity. After the motor reaches a steady state, the stator voltage and current space vectors are analyzed in the frequency domain. As shown in Figure 4.24, the eccentricity-related frequency is located at 50 Hz in the synchronous reference frame according to equation (4.8). The harmonic amplitudes are normalized to the fundamentals so that the harmonic level can be easily identified. In this simulation, the current harmonic is 0.031%, and the voltage harmonic is 0.12%. The stator voltage harmonic is almost fives times that of the current harmonic because of the influence of speed and current PI controllers.

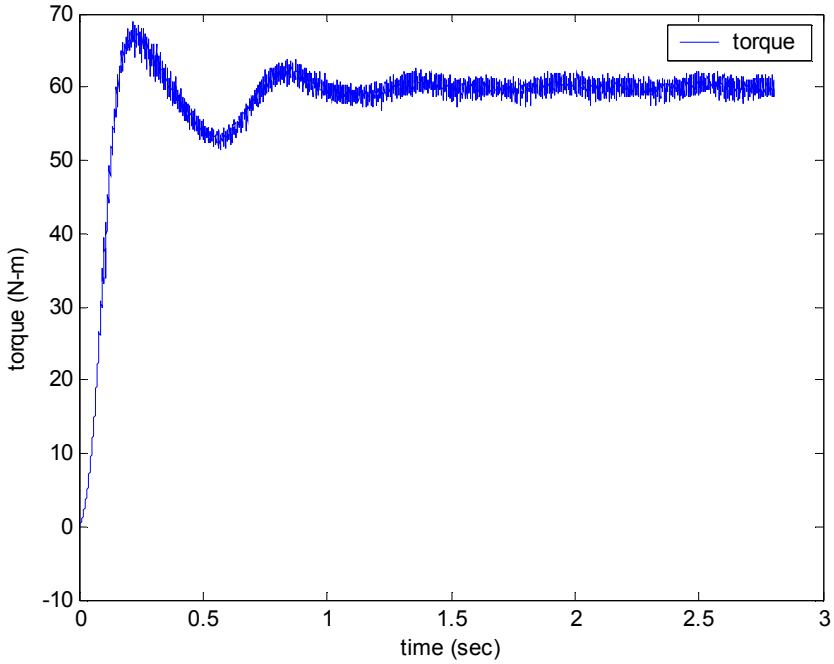

Figure 4.23. Simulated torque vs. time for a faulty motor with a mixed eccentric rotor.

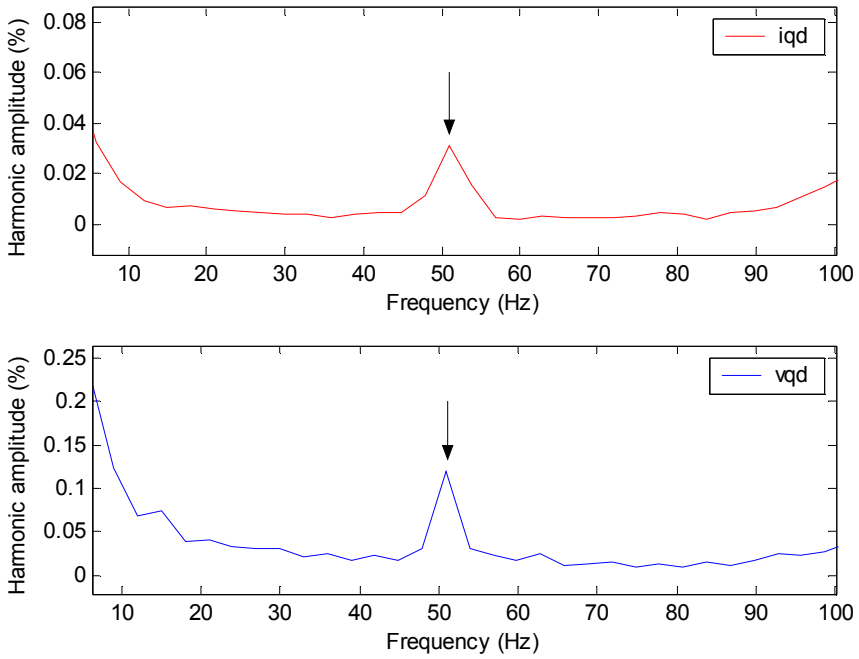

Figure 4.24. Space vector spectral analyses for faulty motor with a mixed eccentric rotor.

4.5.3. Simulation of a motor with mixed eccentricity and a position-varying load

The influence of the mechanical load is evaluated in this simulation. Besides air gap eccentricity, the load torque is set to $0.02n + 10\sin(\theta_m)$ for the sake of simulating a position-varying load caused by misalignment, where θ_m is the rotor position. The spectra of the voltage and current space vectors are shown in Figure 4.25. To compensate for the position-varying load, the motor is commanded to generate a corresponding torque. The current and voltage harmonics therefore increase to 0.39% and 0.35%, respectively. Compared to the results in the second simulation, the current harmonic now becomes larger than the voltage harmonic.

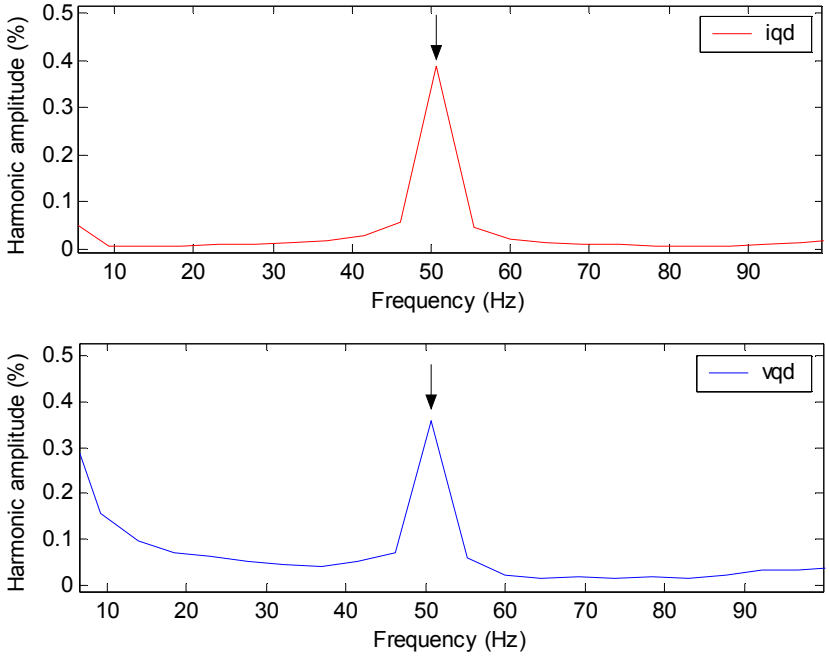

Figure 4.25. Space vector spectral analyses for a faulty motor with mixed eccentricity and a position-varying load.

4.5.4 Simulation of a motor with a static eccentric rotor

Although the focus of this investigation is mixed eccentricity, a motor with static eccentricity is simulated to verify the analysis in Section 4.2. Static eccentricity is created by moving the rotor and its rotational center left from the center of the stator by 30% of the normal air gap. The load torque is still equal to $0.02n$. The spectra of the voltage and current space vectors are shown in Figure 4.26. The eccentricity-related frequencies are located at 1250 Hz and 1144.4 Hz in the synchronous reference frame according to equation (4.9). The current harmonics are 0.081% and 0.028%, while the voltage harmonics are 0.045% and 0.015%, respectively. For static eccentricity, the drive-connected induction motor responds like a line-fed motor. Therefore, more fault information exists in the stator current.

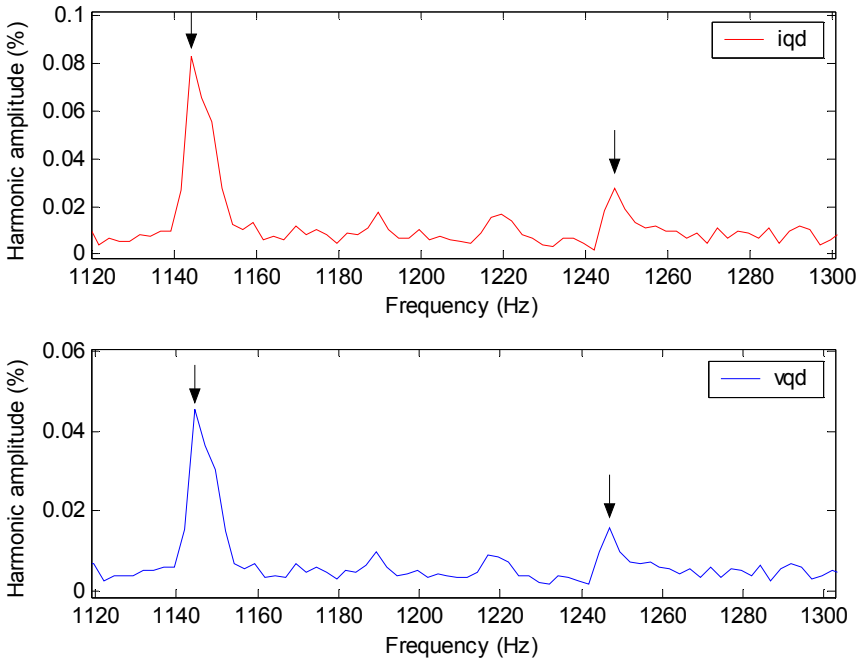

Figure 4.26. Space vector spectral analyses for a faulty motor with a static eccentric rotor.

4.6 Experimental Results

Four experiments are conducted to verify the analysis of the effects of drive controllers and the mechanical load on fault detection. Air gap eccentricity is implemented, as described in Chapter 3. Current bandwidth of the drive is equal to 2000 rad/s, and speed bandwidth is determined by the auto-tuning function of the drive.

4.6.1 No-load test

The motor is supplied by the converter, but not coupled to any load, as shown in Figure 4.27. This test is designed to specifically investigate the effects of the drive controllers. The speed bandwidth is set to 25 rad/s by the auto-tuning feature. As shown in Figures 4.28 and 4.29, when the motor is running at speeds of 300 rpm and 1200 rpm, the frequency of eccentricity-related harmonics is located at 5 Hz and 20 Hz in the synchronous reference frame, respectively. The frequency is shown on the x-axis, and the y-axis is the harmonic amplitudes normalized to the fundamentals. For the operation at 300 rpm, the current and voltage harmonics are 0.001 and 0.0055, respectively. For the operation at 1200 rpm, the current and voltage harmonics are 0.0009 and 0.0013, respectively. According to the analysis in Section 4.2, the converter controllers push more fault information into the voltage. Therefore, voltage harmonics are larger than current harmonics for operation at both 300 rpm and 1200 rpm.

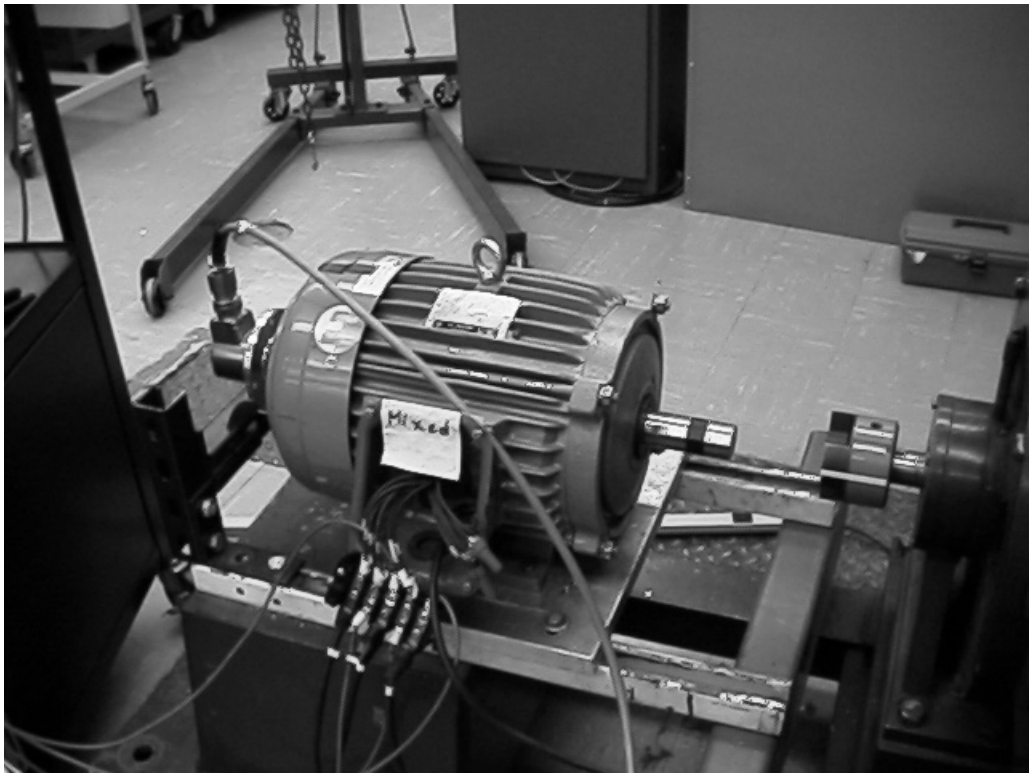

Figure 4.27. Experimental setup of no-load test.

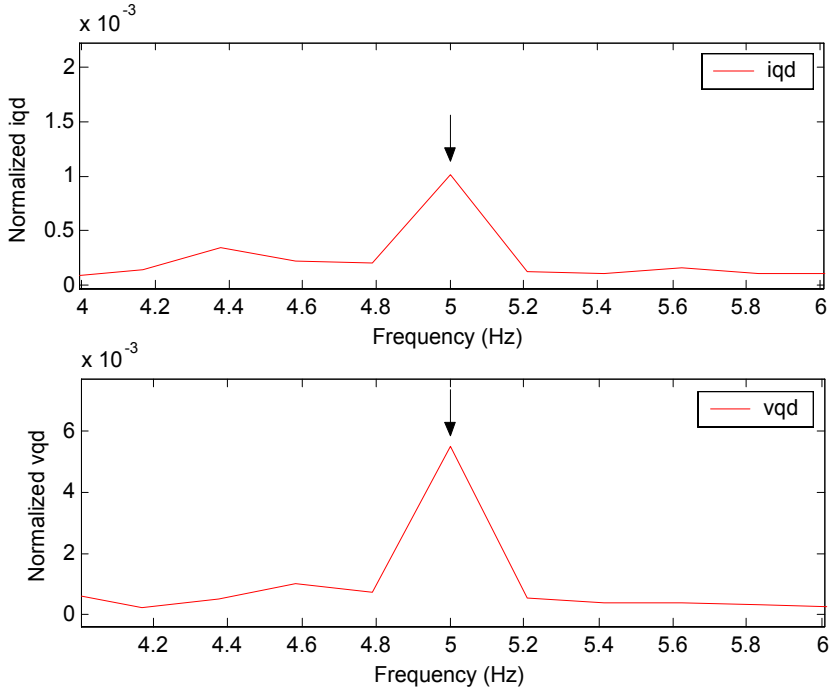

Figure 4.28. Experimental results of no-load test, 300 rpm and BW_{ω}=25 rad/s (auto-tuning).

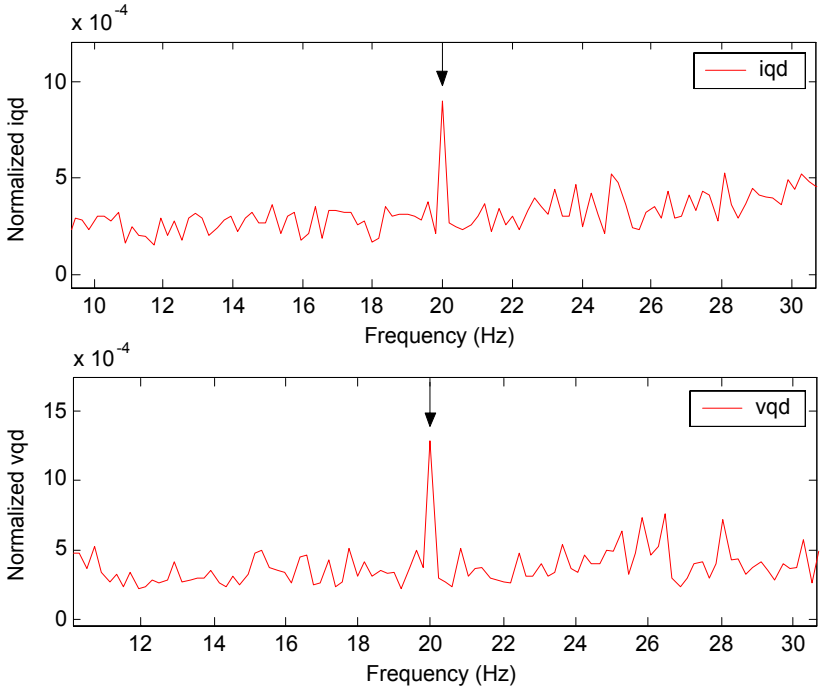

Figure 4.29. Experimental results of no-load test, 1200 rpm and BW_{ω}=25 rad/s (auto-tuning).

4.6.2 Motor loaded with a speed controller bandwidth equal to 16 rad/s (load test)

In the second experiment, the motor is used to drive a DC dynamometer, as shown in Figure 4.30. The output of the dynamometer is connected to resistor banks. The field voltage of the dynamometer is adjusted to 100 V. Because of the air gap eccentricity of the motor, the connection between the motor and dynamometer compose a misalignment. Compared to the first test, since the total inertia of the motor and load increases, the speed bandwidth is reduced to 16 rad/s after auto-tuning. As shown in Figures 4.31 and 4.32, although the motor still runs at 300 and 1200 rpm, the distribution of fault signals between the stator voltage and current is different in comparison to Figures 4.28 and 4.29. For the operation at 300 rpm, the current and voltage harmonics are 0.0295 and 0.027, respectively. For the operation at 1200 rpm, the current and voltage harmonics are 0.014 and 0.0077, respectively. The position-varying load caused

by a misalignment has a dominant influence on the distribution of fault harmonics, and now the current harmonics become larger.

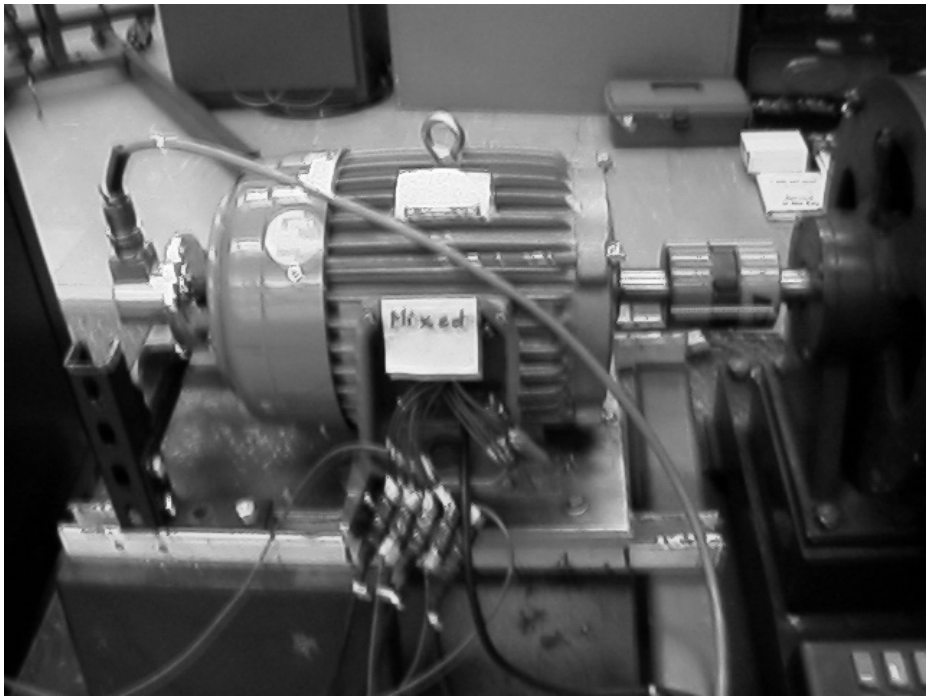

Figure 4.30. Experimental setup of load test.

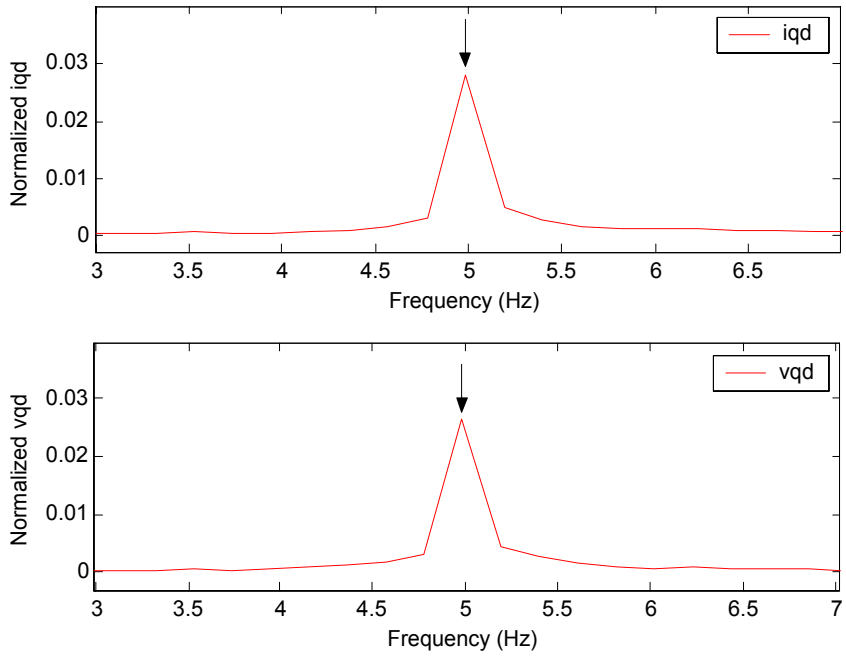

Figure 4.31 Experimental results of load test, 300 rpm and BW_{ω}=16 rad/s (auto-tuning).

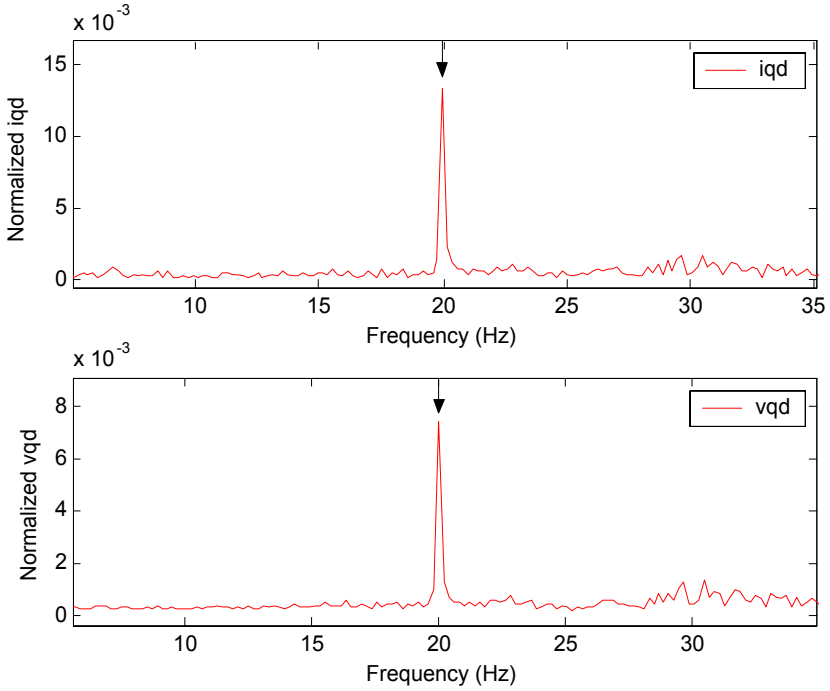

Figure 4.32 Experimental results of load test, 1200 rpm and BW_{ω}=16 rad/s (auto-tuning).

4.6.3 Motor loaded with a speed controller bandwidth equal to 5 rad/s (load test)

In some applications, the speed bandwidth may be adjusted manually to achieve the required operational performance. For example, a lower speed bandwidth helps to avoid cogging but results in a slower response. In the third experiment, the motor still drives the same mechanical load as that in the second experiment. However, the speed bandwidth is manually reduced to 5 rad/s. Experimental results for the operation at 1200 rpm are shown in Figures 4.33 and 4.34. In both the synchronous and stationary reference frames, the voltage harmonics are larger than the current harmonics, as expected. This is because the reduced speed bandwidth limits the ability of drive controllers to compensate for the load oscillation caused by a misalignment. Therefore, the voltage harmonics can remain large.

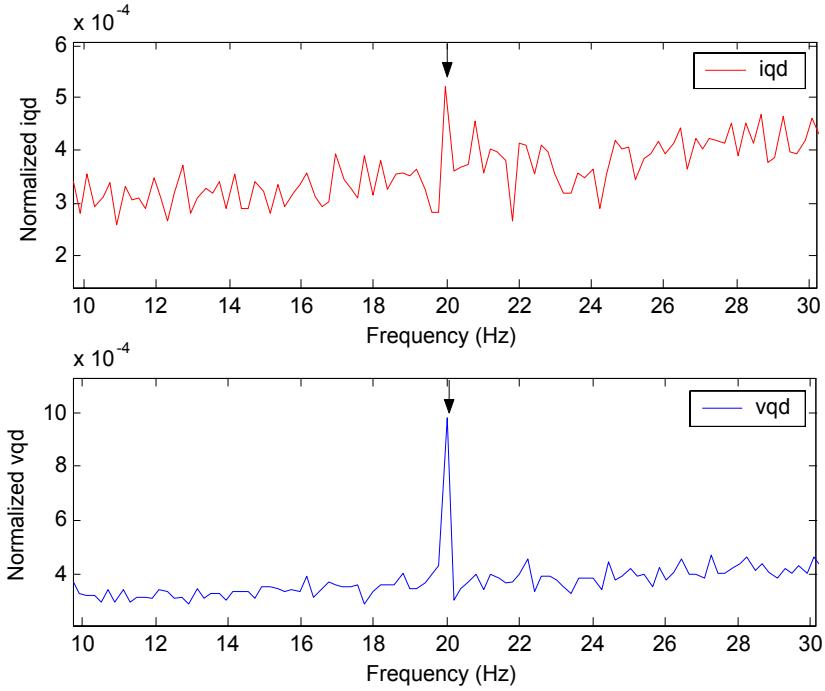

Figure 4.33. Experimental results of load test, 1200 rpm and BW_{ω}=5 rad/s (manual).

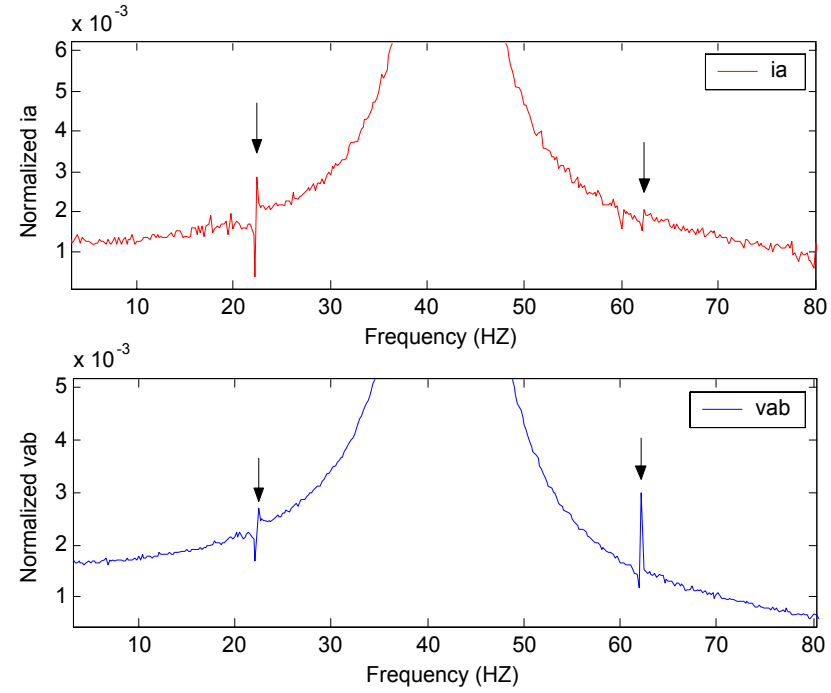

Figure 4.34. Experimental results of load test, 1200 rpm and BW_{ω}=5 rad/s (manual).

4.6.4 Unbalanced disc test

A disc with holes is mounted on the motor shaft between the motor and flexible coupling. By placing bolts into the holes of the disc, an unbalance is created. By moving the bolts further from the center of the disc, a load unbalance is increased. This causes slight air gap eccentricity since there is a force pushing the rotor outwards in the radial direction. However, this also creates a position-varying load torque. Since the motor is no longer coupled to a dynamometer, the total inertia of the motor and load decreases and the speed bandwidth is then increased to 25 rad/s after auto-tuning.

When the motor is running at 300 rpm, 600 rpm, and 1200 rpm, the main eccentricity-related frequency is located at 5 Hz, 10 Hz, and 20 Hz, respectively. As shown in Figures 4.36 to 4.38, the voltage harmonics are 0.00135, 0.005, and 0.00148, while current harmonics are 0.0011, 0.0008, and 0.00064, respectively. The voltage harmonics remain larger than the current harmonics. This is because, although there is a load oscillation on the motor, the load oscillation is not large enough to reverse the distribution of fault signals between the stator voltage and current. These results prove once again that the distribution of fault harmonics depends on both the drive controllers and the mechanical load. Reliable fault detection cannot be achieved by monitoring either voltage or current alone.

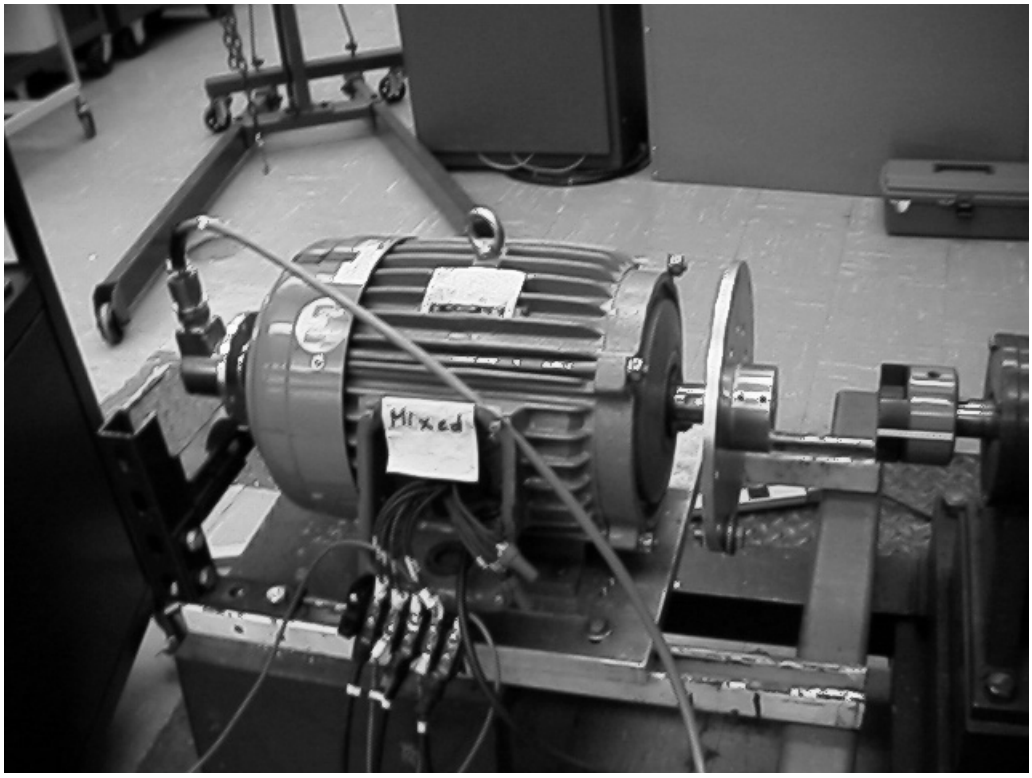

Figure 4.35. Experimental setup of unbalanced disc test.

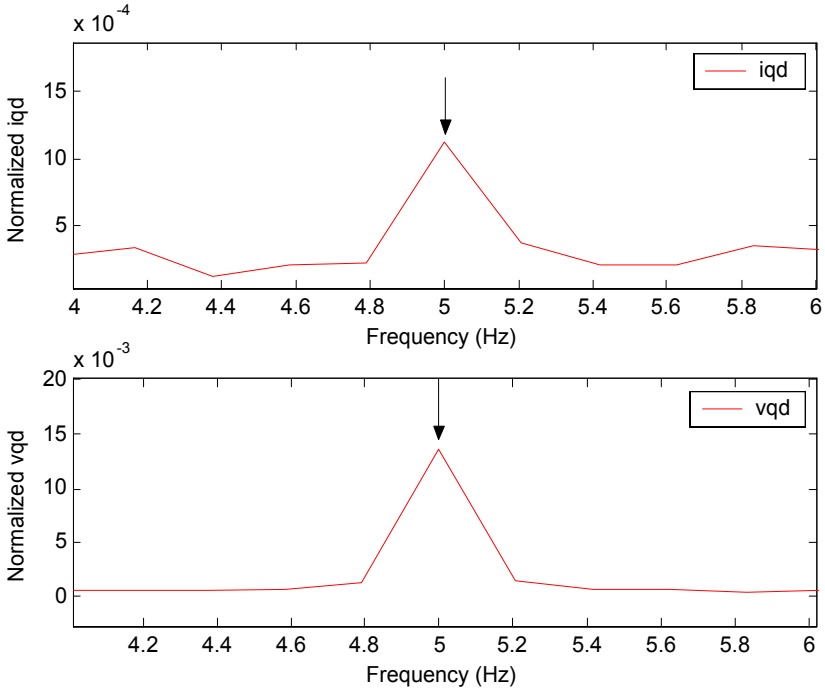

Figure 4.36. Experimental results of unbalanced disc test, 300 rpm and BW_{ω}=25 rad/s (auto-tuning).

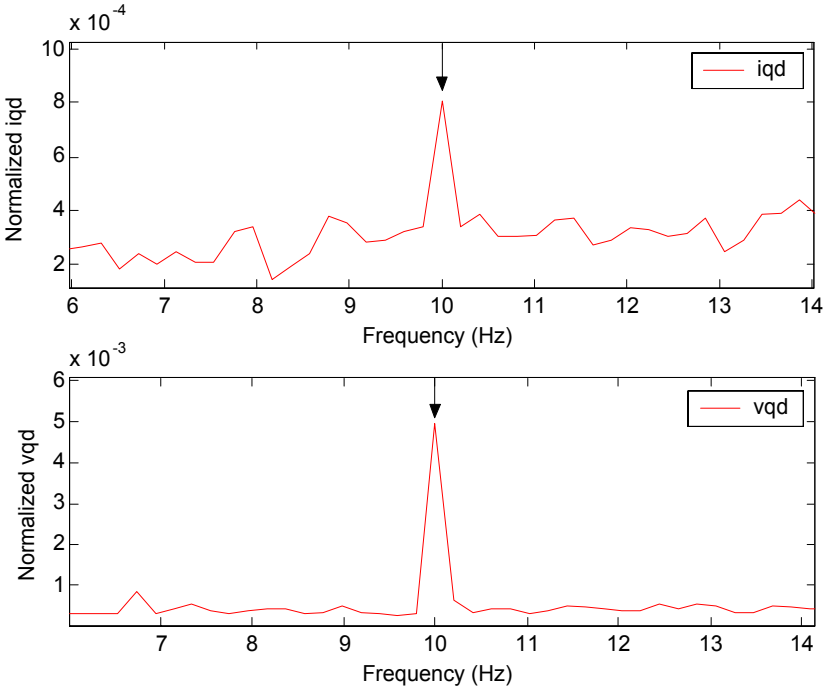

Figure 4.37. Experimental results of unbalanced disc test, 600 rpm and BW_{ω}=25 rad/s (auto-tuning).

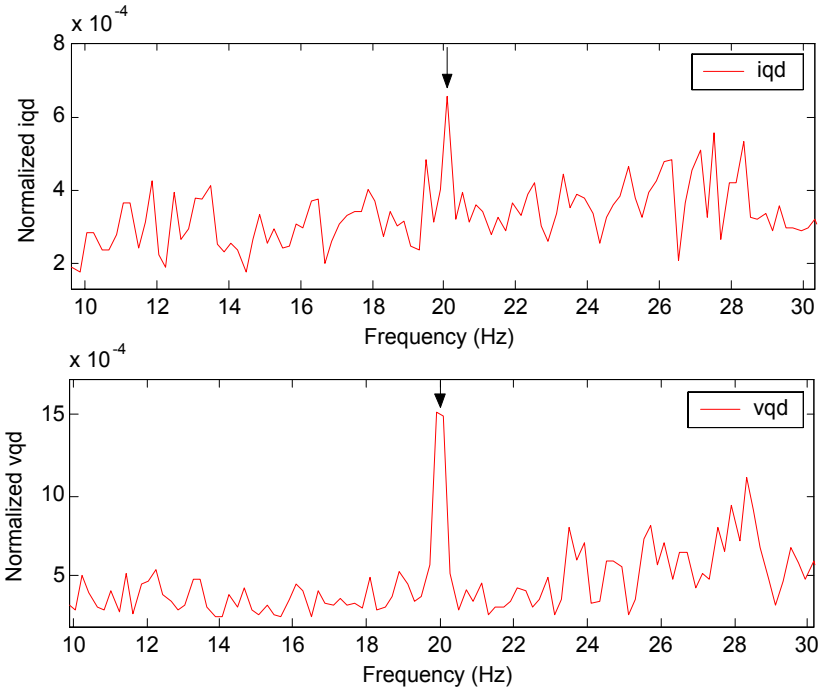

Figure 4.38. Experimental results of unbalanced disc test, 1200 rpm and BW_{ω}=25 rad/s (auto-tuning).

The first and second experiments are conducted at several different speeds, and the results are shown in Figure 4.39. The upper diagram in Figure 4.39 refers to the no-load test and shows that the voltage harmonics remain larger than the current harmonics, as shown in Figures 4.28 and 4.29. Without the mechanical load, the distribution of fault harmonics is basically determined by the drive controllers. However, in the lower diagram corresponding to the load test, the current contains larger harmonics because of the misalignment associated with the mechanical load. The distribution of fault harmonics strongly depends on the operating conditions. Monitoring voltage and current harmonics together is able to ensure good detection reliability and sensitivity.

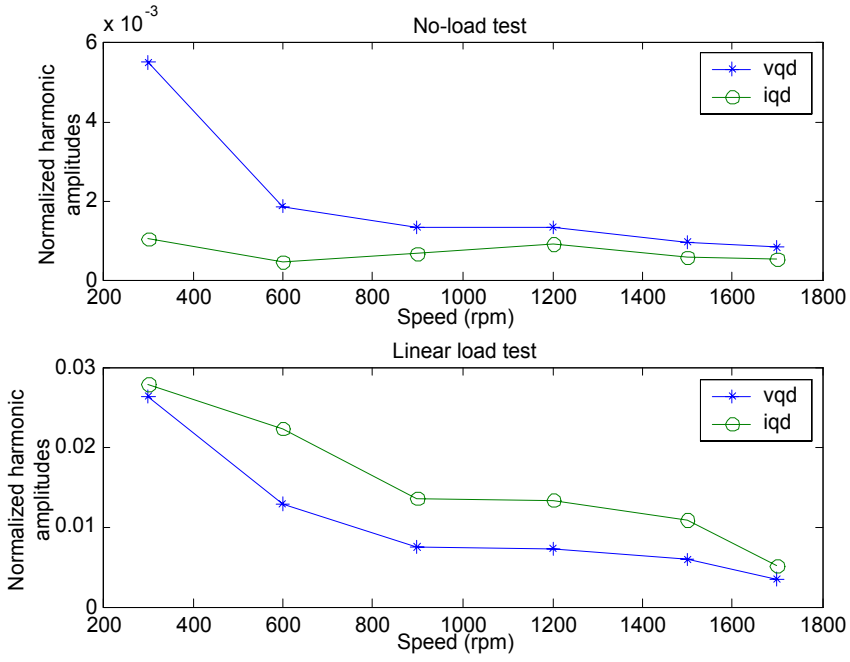

Figure 4.39. Harmonic magnitudes vs. speed in no-load test and load test.

4.7 Conclusions

This chapter analyzed the effects of drive controllers and mechanical load on the distribution of fault harmonics between the stator voltage and current. It showed that the distribution of fault harmonics strongly depended on the operating conditions. Under some operating conditions, current harmonics were much smaller than voltage harmonics, in which traditional MCSA monitoring only stator current was insufficient to provide reliable and sensitive detection. Regarding practical limits, a detection scheme was proposed based on monitoring fault harmonics in both the voltage and current space vectors together. This detection scheme is sensorless and can be implemented at no additional cost.

A direct time-stepping coupled finite element analysis model was then introduced to simulate air gap eccentricity in a closed-loop drive-connected induction motor. This model could simulate the effects of magnetic nonlinearities and space harmonics because of the machine magnetic circuit topology and winding layouts.

Experiments were conducted. The simulation and experimental results validated the analysis of the distribution of fault harmonics and the feasibility of the proposed detection scheme.

CHAPTER 5

DETECTION OF AIR GAP ECCENTRICITY USING AN ARTIFICIAL NEURAL NETWORK

5.1 Introduction

With an adjustable speed drive, motor operating conditions, such as speed and mechanical load, vary widely. The amplitudes of fault harmonics change with operating conditions accordingly, as shown in Figure 4.39. The fault harmonic amplitudes change with speed as the motor and mechanical load form a torsional spring system. This torsional spring system has its own natural frequency and resonates with different amplitudes at different operating conditions. The resonance modifies the air gap and consequently the eccentricity-related fault harmonics. The resonance depends on several factors, such as the inertia of the motor and its mechanical load. If the load is composed of multiple parts connected together by compliant couplings, the resonance also depends on each inertial part, the inter-connection, and installation [57]. The relationship between the fault harmonic amplitudes and operating conditions is too complex to be formulated as strict analytical equations. Furthermore, it is even impossible to measure fault harmonic amplitudes corresponding to all operating conditions experimentally, since the speed and load may change continuously.

To monitor motor conditions, actual measurements on a running motor need to be compared with thresholds obtained on a healthy motor [3, 6, 10]. The thresholds are eccentricity-related harmonic amplitudes of the healthy motor. The relationship between thresholds and operating conditions is therefore necessary in order to establish a reliable

condition monitoring system. This investigation proposes the use of an artificial neural network to learn this complex relationship through training. Once the training is complete, the neural network can estimate the corresponding eccentricity-related harmonic amplitudes for other operating conditions. If the training is based on the experimental data of a healthy motor, the estimations can be used as thresholds to assess the motor condition. Compared with traditional methods such as a look-up table, the neural network provides more accurate estimation because of its non-linear interpolation. Meanwhile, the neural network does not require large memory storage, because it is usually composed of only a few neurons.

The detection algorithm consists of four steps: data acquisition and preprocessing, feature extraction, threshold calculation, and fault detection. The neural network is used in the third and fourth steps. Experimental results are included to verify the feasibility of this detection scheme.

5.2 Data Acquisition and Preprocessing

The most effective method for analyzing data in the frequency domain is the Fourier transform. The discrete Fourier transform (DFT) is typically used for discrete sampling systems. A common requirement of spectrum analysis using the Fourier transform is that the signal, x, is stationary. However, in the detection, the frequency and magnitudes of the stator voltage and current of a drive-connected induction motor always change. They are non-stationary.

To improve the accuracy of spectrum analysis, the short time Fourier transform (STFT) is developed [11]. The STFT partitions the sampled data with a sliding window of a short width. In each window, the signal is assumed stationary and is analyzed in the frequency domain using the DFT. For most variable speed applications in industry, excluding servo motors, assuming a steady state of 1-2 seconds is reasonable since the mechanical system usually has a large inertia time constant. In this investigation, the window is selected to be 2 seconds at a sampling rate of 20 kHz. This window provides enough resolution in the spectrum analysis for speeds higher than 150 rpm. Several indices can be used to determine whether there is a variation of operating condition in each window. For example, if changes in the frequency or magnitude of the fundamental current remain less than preset tolerances, the collected data is considered stationary.

The experimental AC drive used in this research does not provide access to the controller parameters, such as the voltage and current space vectors. The space vectors are calculated from two line-to-line voltages and two phase currents measured at motor terminals. The experimental motor does not have a neutral. The third phase can be calculated from the two phase measurement, and then three-phase currents are transformed into α-β reference frame according to

$$\begin{bmatrix} \alpha \\ \beta \end{bmatrix} = \frac{2}{3} \begin{bmatrix} 1 & -\frac{1}{2} & -\frac{1}{2} \\ 0 & \frac{\sqrt{3}}{2} & -\frac{\sqrt{3}}{2} \end{bmatrix} \times \begin{bmatrix} a \\ b \\ c \end{bmatrix} \tag{5.1}$$

where a, b, and c are the currents in a three-phase reference frame, and α and β are the currents in a two-phase reference frame. The α-β reference frame is actually a stationary

reference frame parallel to the rotational, synchronous d-q reference frame oriented to the rotor flux, as shown in Figure 5.1.

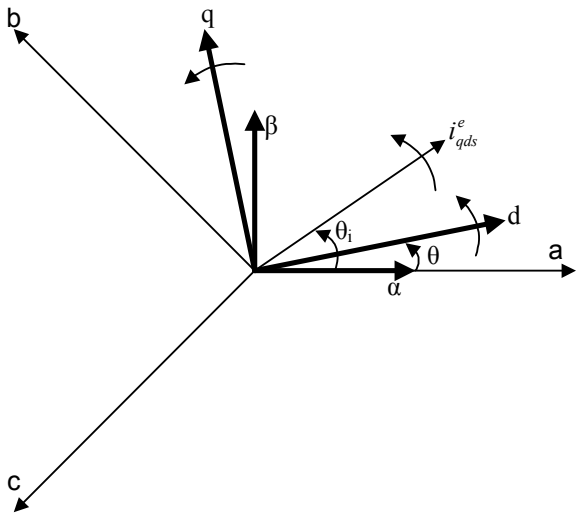

Figure 5.1. Relationship of three reference frames: a-b-c, α-β, and d-q.

The current space vector, i^e_{qds}, and its phase angle, θ_i, with respect to the stationary α-axis are first calculated from i_α and i_β. The d-axis is first assumed to coincide with i^e_{qds}, and the phase angle between the d-axis and α-axis is equal to θ_i initially. The actual phase angle of the rotor flux is defined as θ, which is also the actual phase angle of the d-axis in a field-oriented frame. Since the current phasor i^e_{qds} rotates synchronously with the d-q reference frame, θ_i and θ are stationary relative to each other. There is a constant phase angle between them.

The experimental AC drive provides the value of the actual reference flux current, I^*_{ds}, which can be read from the user interface. It is a constant value. The quantity i^e_{ds} is calculated by changing angle θ_i. Whenever $\hat{I}^*_{ds}$ (the average value of i^e_{ds}) becomes equal

to the given I_{ds}^{*}, the field orientation is achieved. The process for the above calculation is shown in Figure 5.2.

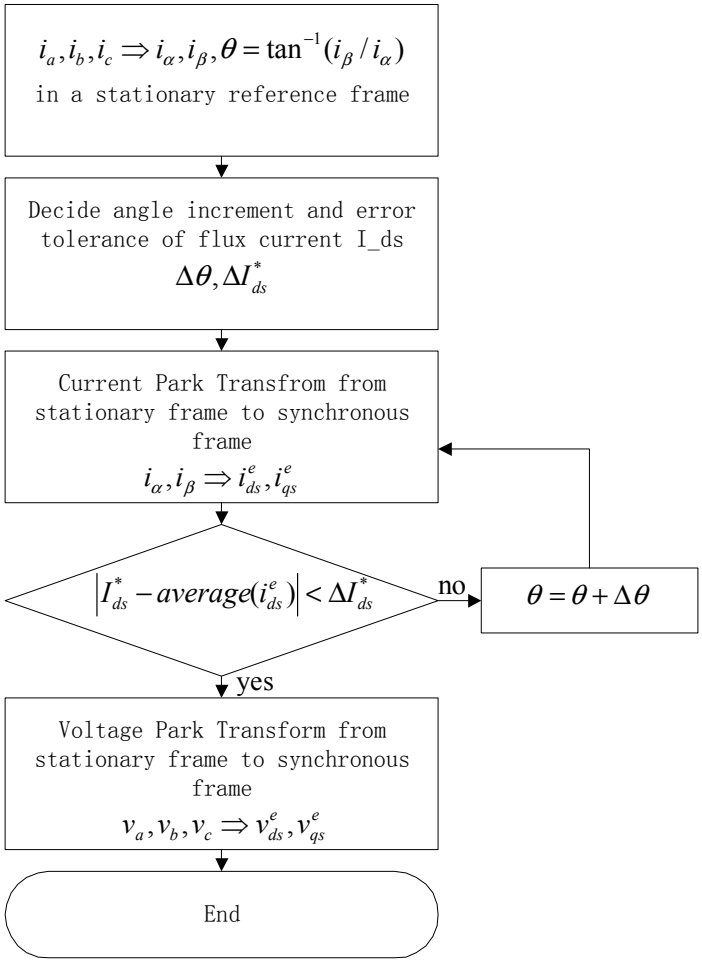

Figure 5.2. Flow chart of reference frame transform in the data preprocessing phase

5.3 Feature Extraction

Once the spectra of the stator voltage and current space vectors, v_{qds}^{e} and i_{qds}^{e}, are calculated, the parameters can be analyzed in the frequency domain. To reduce the large amount of spectral information to a usable level, a frequency filter is used to extract feature components pertinent to the detection of air gap eccentricity. This filter is a

window centered at the eccentricity-related frequency given by equation (4.8), with a width of 2 Hz and amplitude of one. The feature components can be calculated in several ways, for example, averaging all the FFT components within that window, or selecting the maximum component within that window as used in this investigation. The maximum components are denoted as $v_{f_{ecc}}$ and $i_{f_{ecc}}$ for the voltage and current, respectively.

5.4 Training and Testing of the Artificial Neural Network

After the feature components of the stator voltage and current space vectors are extracted, an artificial neural network is used to learn the relationship between the feature components and operating conditions and to predict motor conditions. A neural network is composed of simple processing elements (PE) operating in parallel. The network function is determined largely by the connections between elements. A neural network can be trained to perform a particular function by adjusting the values of the connections (weights) between each element.

This investigation uses a supervised three-layer feed-forward network that uses back-propagation as a training algorithm. The input layer represents the system inputs. The single hidden layer provides the learning capability of the network. The output layer consists of one neuron $\hat{y}$ that is an estimation of $(\hat{v}_{f_{ecc}} + \hat{i}_{f_{ecc}})$. The neural network is first trained with samples of a healthy motor. Once the training is complete, the weights are frozen and the neural network represents the relationship between operating conditions and eccentricity-related harmonic magnitudes of a healthy motor. Once air gap

eccentricity sets in, the amplitudes of the measured eccentricity-related harmonics y of the stator voltage and current space vectors will become continuously larger than $\hat{y}$ of the healthy motor predicted by the neural network.

Various techniques can be utilized to train the neural network to learn harmonic amplitudes, $y = v_{f_{ecc}} + i_{f_{ecc}}$, corresponding to different operating conditions. The basic idea is to adjust the weights to minimize the mean square error (MSE) between neural network outputs $\hat{y}$ and actual measurements y.

The structure of the neural network is determined heuristically. For example, it is known that signal y is affected by operating conditions. However, the parameters representing operating conditions need to be determined and sent to the inputs. The activation functions need to be selected based on the property of fault harmonics. The process to determine the neural network is explained below.

5.5 Experimental Results

The neural network training data are collected on a healthy motor when the speed changes from 150 rpm to 1755 rpm (motor nameplate speed) at intervals of 25 rpm, while the field voltage of the dynamometer changes from 90 V to 125 V at intervals of 5 V. There are a total of 520 operating points.

Two sets of validation data are collected on both a healthy and a faulty motor. The first set of validation data is sampled when the speed is equal to {150, 300, 450, 600, 750, 900, 1050, 1200, 1350, 1500, 1650, 1755 rpm}, while the field voltage for each

speed is set equal to {90, 95, 100, 105, 110, 115, 120, 125 V}, giving a total of 96 points. The second set of validation data is sampled when the speed is equal to {600, 712, 887, 900, 1037, 1189, 1200, 1362, 1500, and 1563 rpm}, while the field for each speed voltage is set equal to {90, 95, 100, 105, 110, 115, 120 V}, giving a total of 70 points. The first set of validation data is collected at the same speed as the training data to validate the learning ability of the neural network. The second set of validation data is collected at different speeds to validate the ability of the neural network to interpolate.

Three types of neural networks are trained and tested with above experimental data.

5.5.1. Type 1 neural network

The structure of the first neural network is shown in Figure 5.3. The output of the network is $\hat{y}$, the sum of the eccentricity-related harmonics of the stator voltage and current space vectors, each normalized to their respective fundamental values. The neural network has two inputs: the motor speed and the fundamental frequency of the stator current, both normalized to the nameplate values of the motor. These two parameters actually determine the slip according to

$$s = 1 - \frac{p\omega_m}{60 f_1} \tag{5.2}$$

where s is the slip, p is the number of pole-pairs, ω_m is the speed, and f_1 is the fundamental frequency. One value for slip corresponds to one point at the mechanical characteristic of the induction motor.

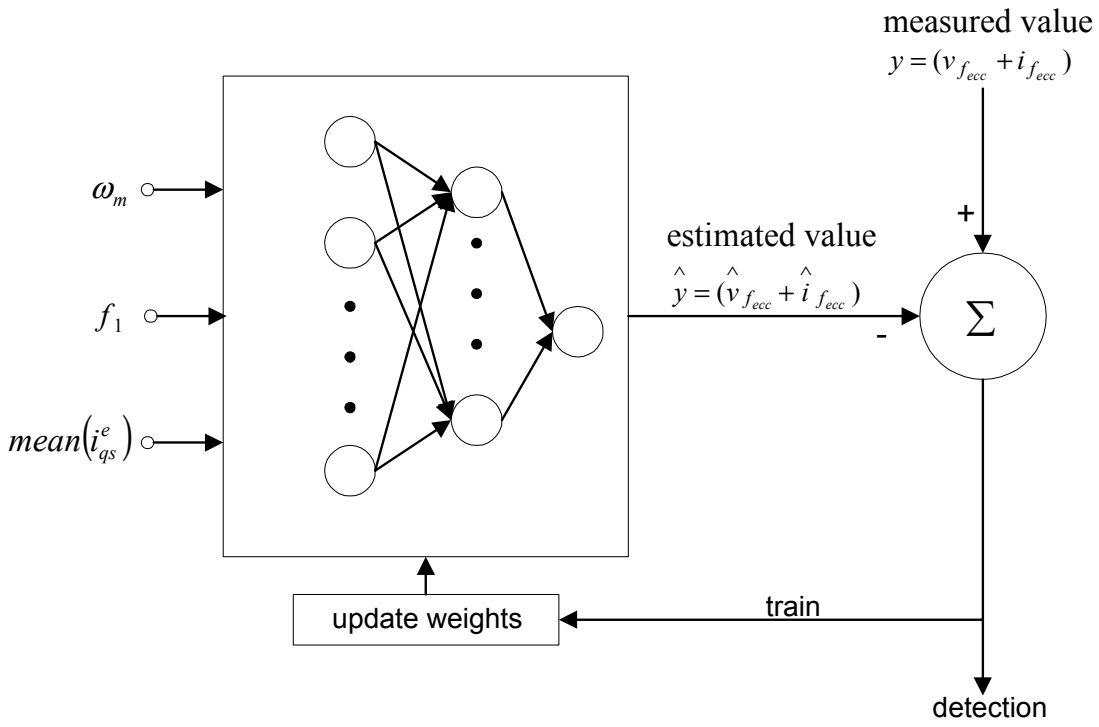

Figure 5.3. Structure of the artificial neural network.

The neurons in the hidden layer use the hyperbolic tangent sigmoid activation function and the output neuron uses a linear activation function, as shown by Figures 5.4 and 5.5. Their mathematical definitions are given by

$$f(n) = \frac{2}{(1+e^{-2n})} - 1 \tag{5.3}$$

$$f(n) = n \tag{5.4}$$

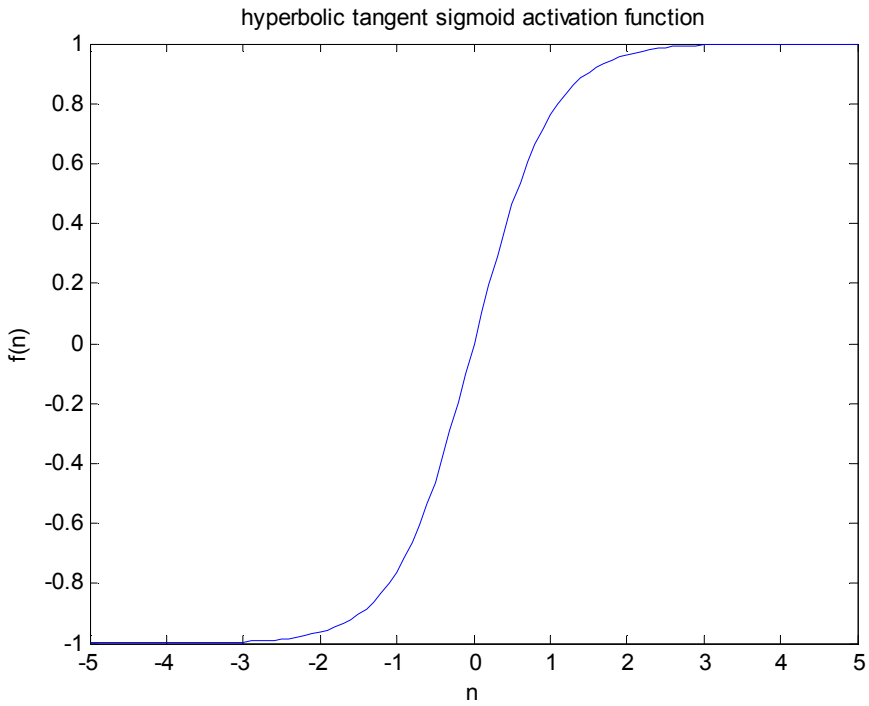

Figure 5.4. The hyperbolic tangent sigmoid activation function.

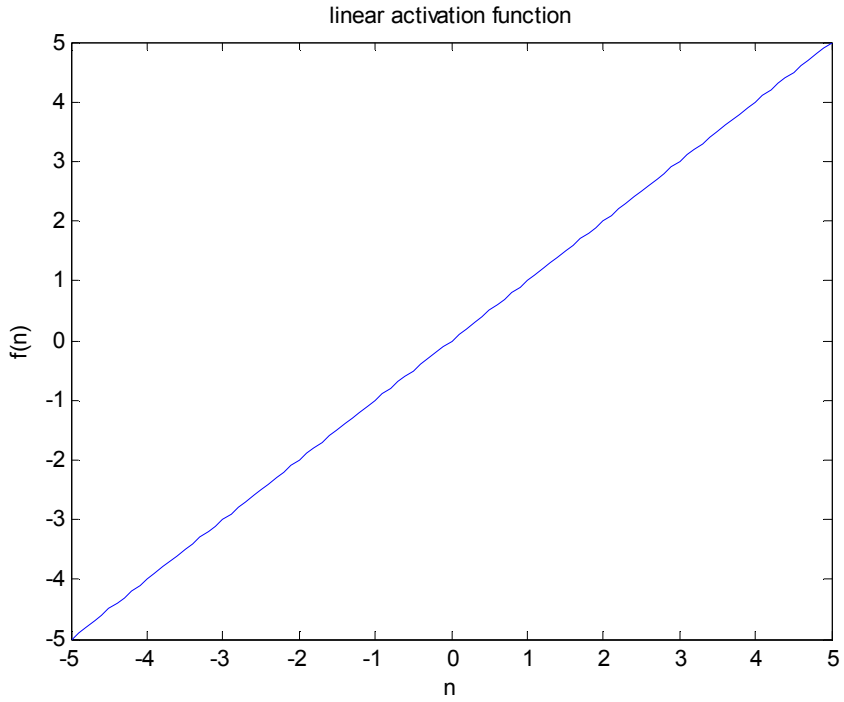

Figure 5.5. The linear activation function.

The training is complete after 2000 epochs. The training results are shown in Figures 5.6 and 5.7. Figure 5.6 shows that the training error is stable after 1400 epochs. The weights are then frozen and the 520 data points in the training set are passed through the neural network to verify $\hat{y}$ for this small training error, as illustrated in Figure 5.7. Because of the error, it is necessary to conduct the testing at several different operating conditions rather than at only one point. An air gap eccentricity fault is determined only when measurements are consistently larger than estimated thresholds. In this way, the effect of estimation errors in fault detection is reduced.

The eccentricity fault is now introduced and the faulty motor is operated at 96 operating points that are included in the training set of 520. The results appear in Figure 5.8. The upper diagram corresponds to the validation data collected on a faulty motor, while the lower one corresponds to the validation data collected on a healthy motor. In the upper diagram, $\hat{y}$ is compared with $1.2\,y$, which is the estimated threshold of a 20% margin above the healthy motor values. Since $\hat{y}$ remains consistently larger than the estimated threshold, the eccentricity fault can be detected. In the lower diagram, $\hat{y}$ is compared with y to verify the learning ability of the neural network. The experimental measurements y are equal to estimations $\hat{y}$ at most operating points.

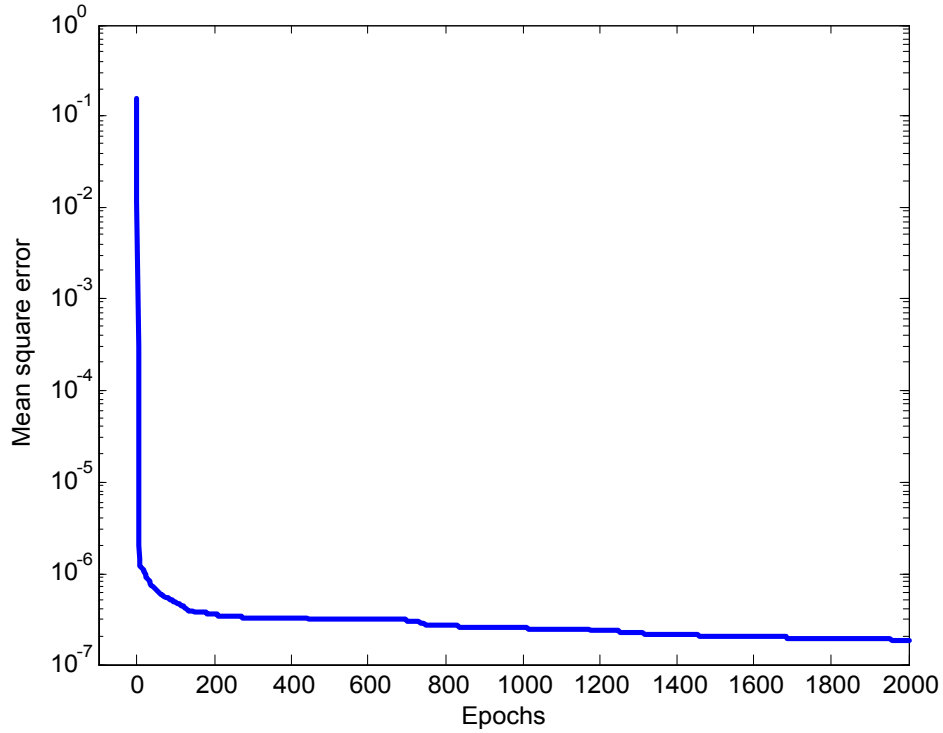

Figure 5.6. Training process of the neural network.

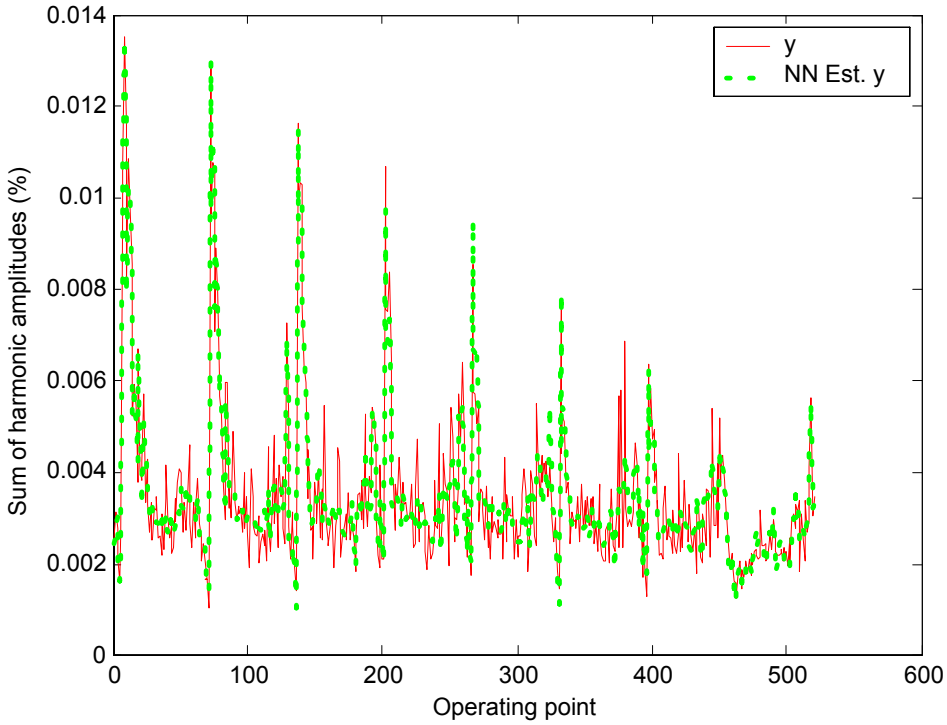

Figure 5.7. Training results of the neural network.

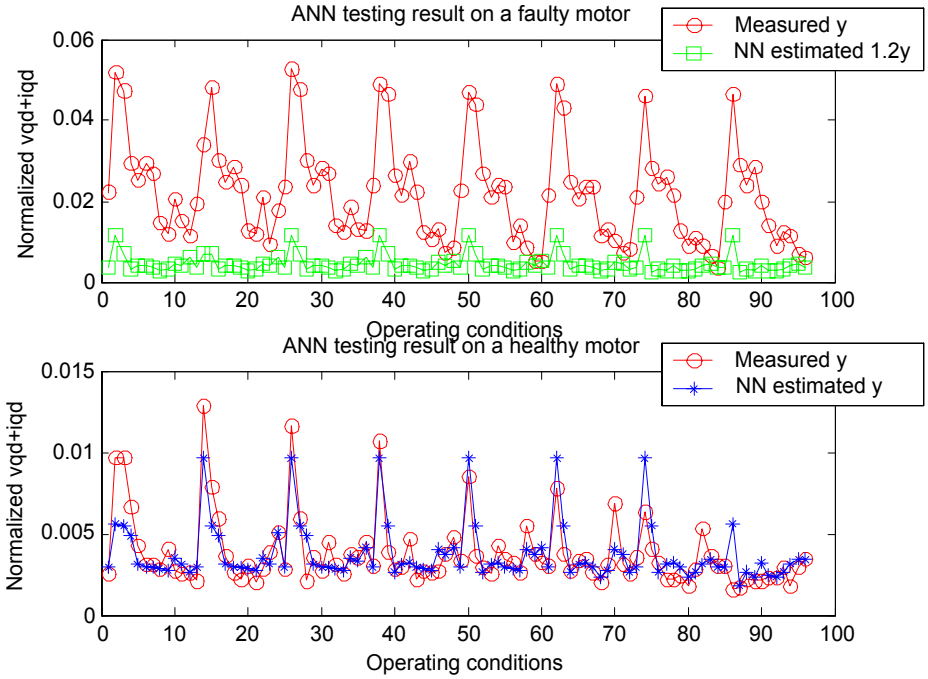

Figure 5.8. Experimental results of Type 1 neural network with the first set of validation data.

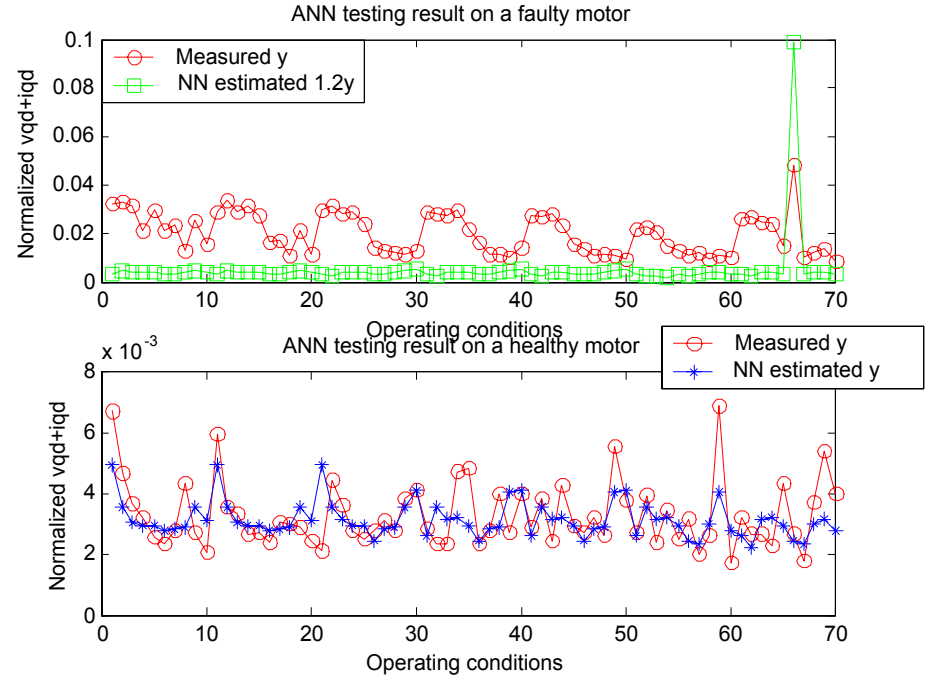

Figure 5.9. Experimental results of Type 1 neural network with the second set of validation data.

The experimental results of the second set of validation data are shown in Figure 5.9. Now the faulty motor is operated at different points than the training set of 520. The neural network cannot detect the faulty motor because the estimated threshold becomes larger than the measurement at point 66. The experimental results of the healthy motor are shown in the lower diagram of Figure 5.9. There are errors between y and $\hat{y}$ because the speeds of the test data and the training data are different. However, the errors will not cause a wrong prediction of mistaking the healthy motor as a faulty motor since y is not consistently larger than $\hat{y}$.

5.5.2. Type 2 neural network

With AC drives, the fundamental frequencies of the voltage and current change with speed. This variation changes the slip-torque characteristic of an induction motor, as shown in Figure 5.10. The linear load used in this investigation intersects the different motor curves at different operating points in Figure 5.10. Thus, the two inputs of the Type 1 neural network in Section 5.5.1 are not enough to represent an operating condition since they can decide only the slip. The Type 2 neural network has three input components: the speed, the fundamental frequency of the stator current, and the q-axis torque current i_{qs}^{e}, all normalized to the nameplate values. Again, the first two inputs determine the slip. Since the output torque is proportional to i_{qs}^{e} in the vector control, the torque is determined by the third input. Now the neural network is able to identify an operating point by torque and slip together.

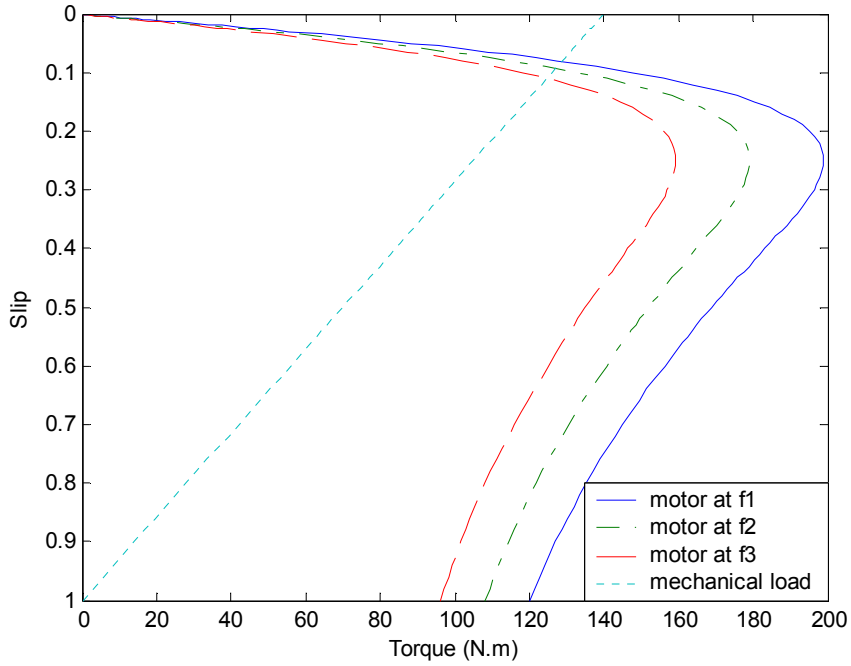

Figure 5.10. Slip-torque characteristics of the motor and load with AC drives.

Once again, the neural network is trained and tested. The experimental results are shown in Figures 5.11 and 5.12. In Figure 5.11, the performance of neural network is tested by the first set of validation data. The neural network distinguishes the faulty motor from the healthy motor, as it does for the Type 1 neural network. However, compared to Figure 5.9, the Type 2 neural network corrects the wrong estimation at point 66 made by the Type 1 neural network tested with the second set of validation data, as shown in the upper diagram of Figure 5.12. Measurements y become consistently larger than estimations $\hat{y}$ and the motor is predicted to be faulty. This proves that the third input i_{qs}^{e} helps improving the performance of the neural network.

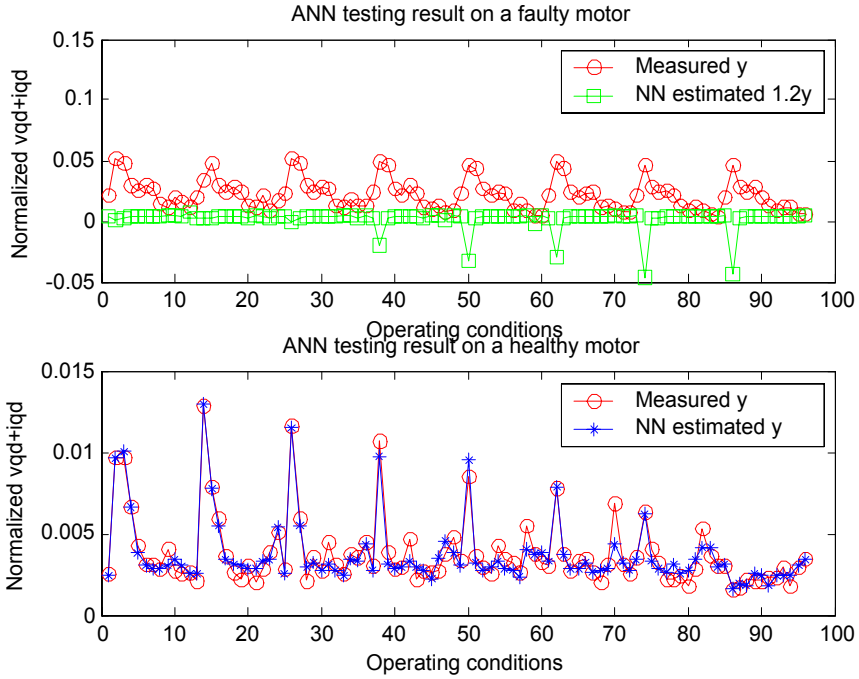

Figure 5.11. Testing results of Type 2 neural network with the first set of validation data.

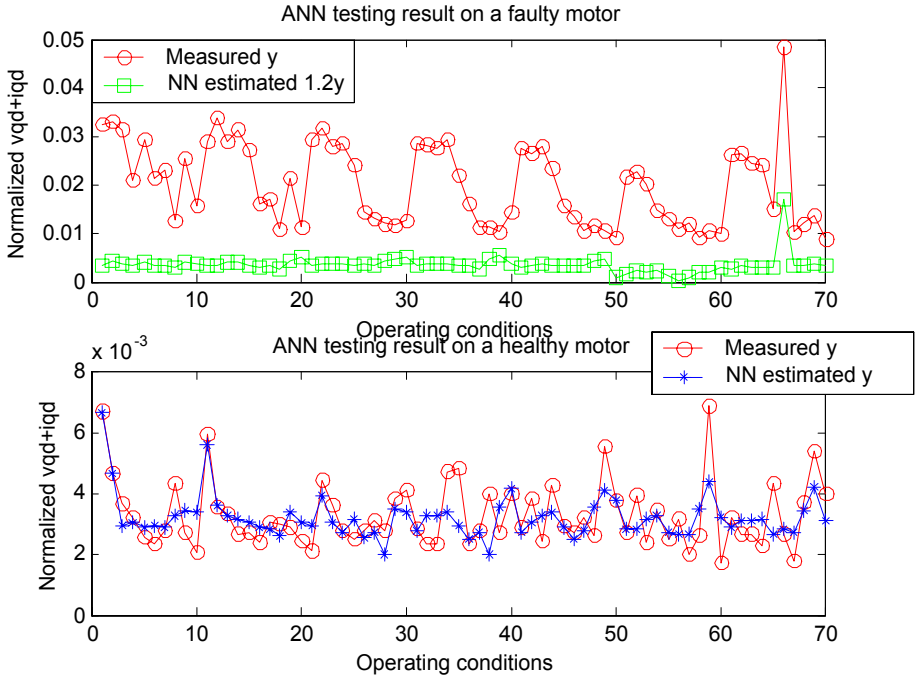

Figure 5.12. Testing results of Type 2 neural network with the second set of validation data.

5.5.3. Type 3 neural network

The training data $y = v_{f_{ecc}} + i_{f_{ecc}}$ collected on a healthy motor have small magnitudes. In the Type 3 neural network, y is scaled by a preset constant (*e.g.*, 100) to fall within the range of the sigmoid functions, which improves the performance of the neural network. In addition, as shown in the upper diagram of Figures 5.11 and 5.12, the neural network gives negative estimations $\hat{y}$ at some operating conditions for a faulty motor. However, the actual eccentricity-related harmonics are always larger than zero. Negative outputs should be avoided to prevent the weights from being updated in the wrong direction. The linear activation function of the output neuron is therefore replaced by a logarithmic sigmoid activation function of equation (5.5) whose output is always positive as shown in Figure 5.13.

$$f(n) = \frac{1}{(1+e^{-n})} \tag{5.5}$$

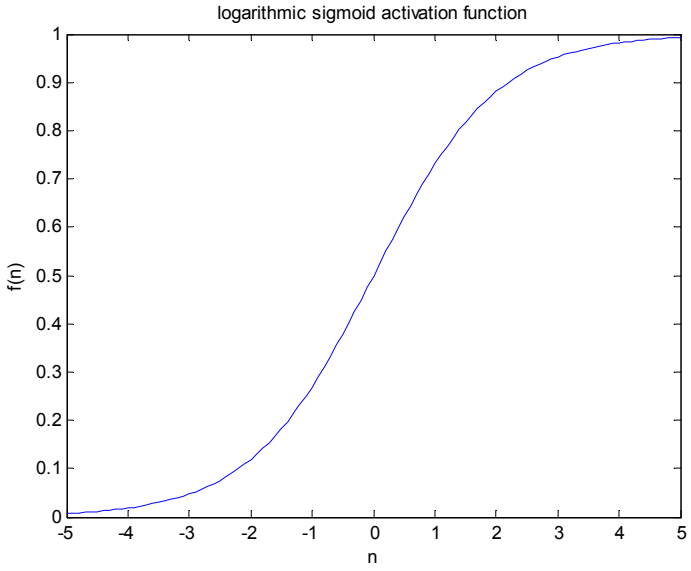

Figure 5.13. The logarithmic sigmoid activation function.

The testing results are shown in Figures 5.14 to 5.19. Figures 5.14 and 5.19 show the experimental results with the first and second sets of validation data in 2-D, respectively. They support that the neural network can detect the faulty motor correctly, same as the Type 1 and Type 2 neural networks. However, the negative output from the neural network is now eliminated. Figures 5.15 and 5.16 give the same testing results as the first set of validation data in 3D by plotting the estimation against field voltage and speed. In Figure 5.15, the measurement surface for the faulty motor remains above the estimation surface for the healthy motor. However, the two surfaces exchange their positions in Figures 5.16 since the measurement surface and estimation surface both apply to a healthy motor. Figures 5.17 and 5.18 confirm the diagnostic performance of the neural network when the motor runs from low to full speed and light to full load. The two different patterns given by the neural network can be distinguished by software. It is clear that the Type 3 neural network is feasible for detecting rotor eccentricity faults over the entire range of operating conditions of the experimental induction motors, including those conditions where it has not been trained.

In practice, it is unlikely that a motor drive could be taken from no-load to full load, at many different speeds, simply to train the neural network. Figure 5.20 explains how this can be overcome by simply training with a data set gathered during the first few hours or days after commissioning [53]. After this training, the training data changes only when a new operating condition appears. Once new data is added into the training set, the neural network is trained again.

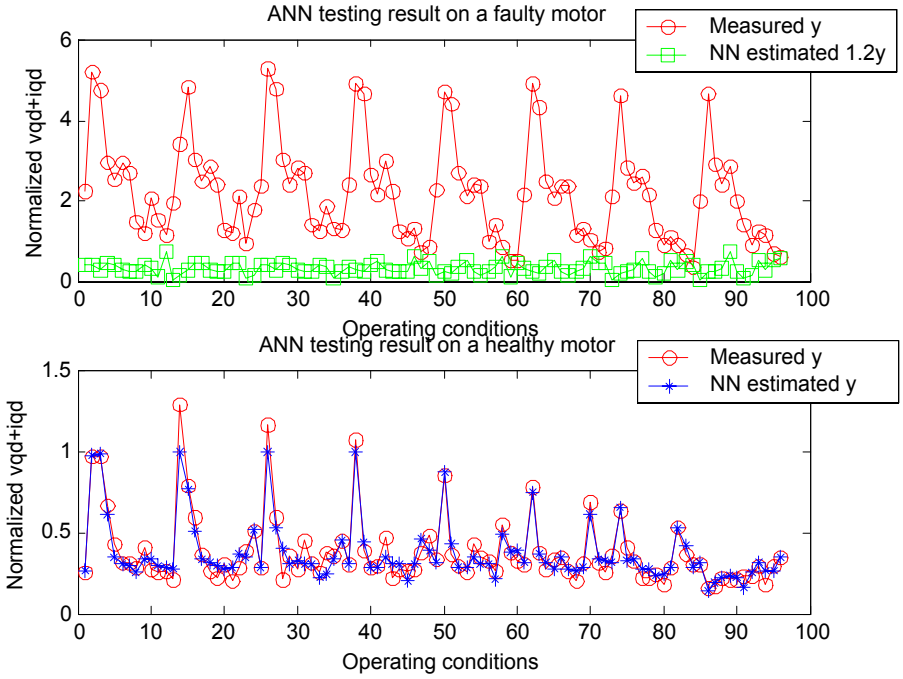

Figure 5.14. Testing results of Type 3 neural network with the first set of validation data.

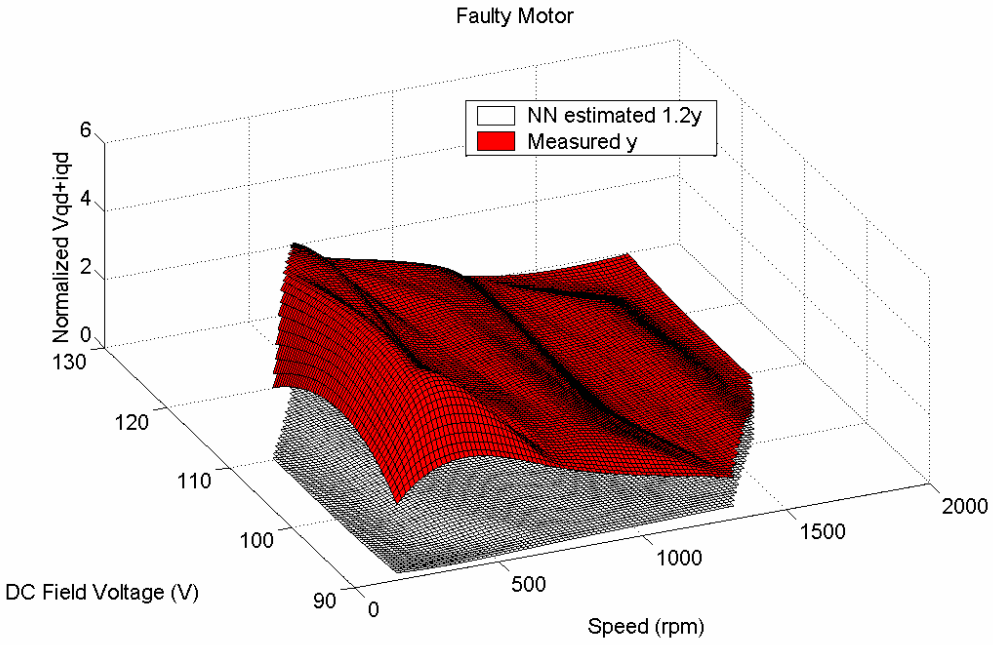

Figure 5.15: Testing results of Type 3 neural network with the first set of validation data on a faulty motor shown in 3D.

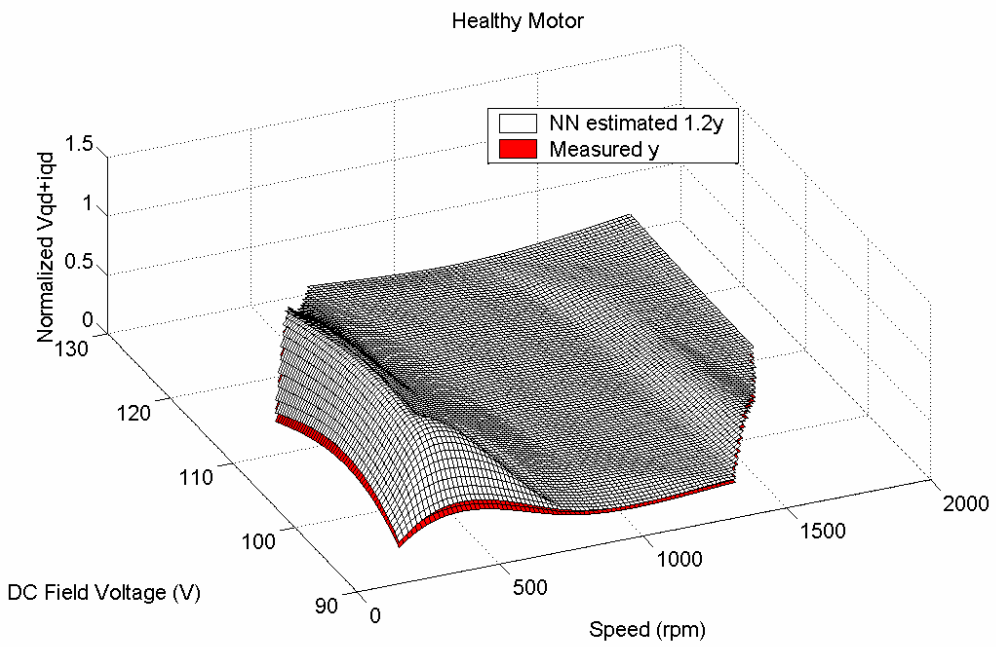

Figure 5.16: Testing results of Type 3 neural network with the first set of validation data on a healthy motor shown in 3D.

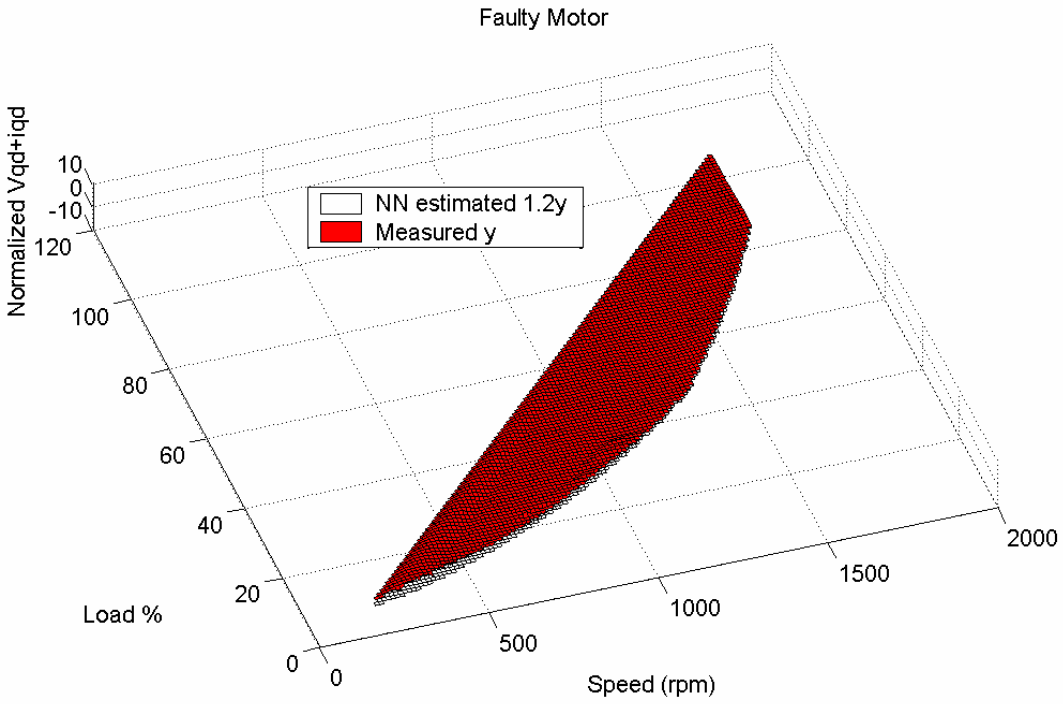

Figure 5.17: Testing results of Type 3 neural network with the first set of validation data on a faulty motor shown in 3D.

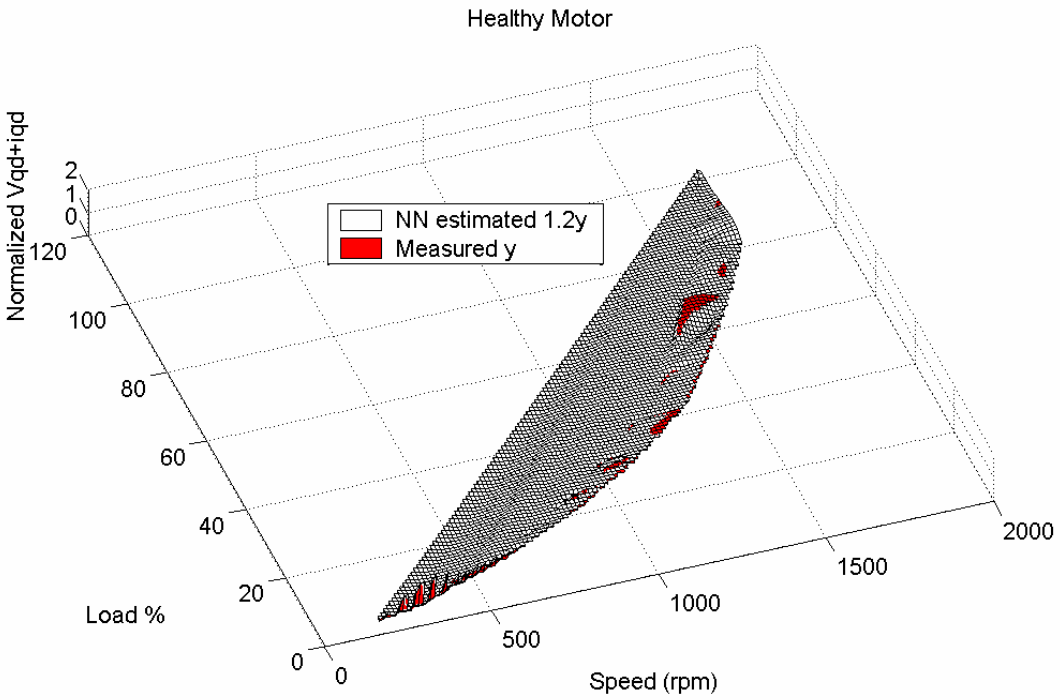

Figure 5.18: Testing results of Type 3 neural network with the first set of validation data on a healthy motor shown in 3D.

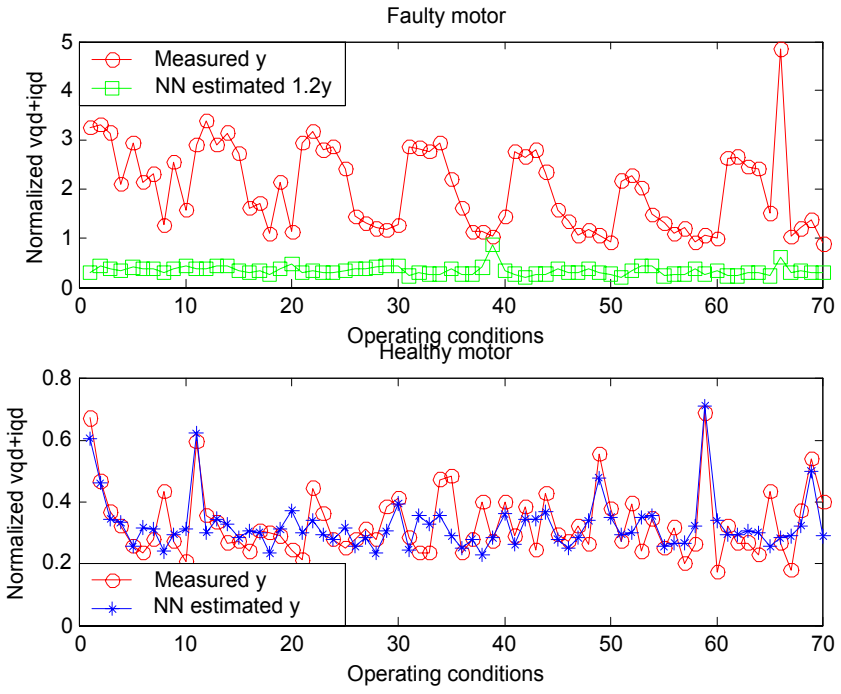

Figure 5.19: Testing results of Type 3 neural network with the second set of validation data.

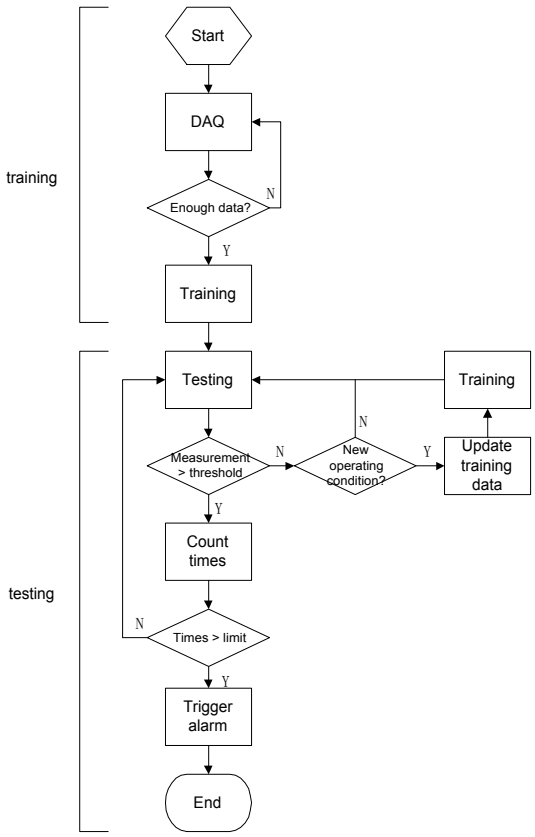

Figure 5.20. Flow chart of the detection scheme including updating processes

5.6 Conclusions

This chapter described a detection scheme with the use of an artificial neural network. The detection was based on monitoring the fault harmonics of the stator voltage and current space vectors together.

The artificial neural network was used to learn the complex relationship between fault harmonic amplitudes and operating conditions. Once the learning was complete, the neural network could estimate the thresholds corresponding to different operating conditions, which was then used to predict motor conditions. The design process of the neural network was illustrated. The training and testing results showed that the Type 3

neural network gave the best performance. The experimental results validated that the Type 3 neural network was feasible for fault detection over the entire range of operating conditions of the experimental motors.

CHAPTER 6

EFFECT OF AIR GAP ECCENTRICITY ON SURGE TEST DATA

6.1 Introduction

In many cases, an inexpensive and reliable off-line method for eccentricity detection can be useful, especially for routine and detailed maintenance. On-line methods are typically based on monitoring special frequency components in motor stator voltage and current, and require data sampled with high resolution and noise immunity. This chapter illustrates the relationship between air gap eccentricity and surge test waveforms that are commonly used for detecting stator winding insulation problems. Air gap eccentricity makes surge waveform rotor-position dependent. In this way the eccentricity can be clearly seen without any spectral analysis of voltage or current, but still in a completely unobtrusive manner. In this way eccentricity can be detected with minimal noise interference and a high degree of reliability using test equipment that many users already have on hand.

Surge testing is performed with an impulse generator, which contains an oscilloscope-type display to observe the "surge waveform" in progress. In general, the impulse generator consists of a capacitor and a controllable switch. The capacitor is first charged to a high DC voltage. In a surge test, once the switch is turned on, a steep voltage front (high dv/dt) is applied to the stator windings by quickly discharging the capacitor. The current flows into one phase and out from the other two phases. The

surge voltage waveform across the stator windings during the test can be described by its peak values and zero crossing points [50, 51].

6.2 Detection of Air Gap Eccentricity Using the Surge Test

During surge testing, the stator and impulse generator's internal capacitor form a series resonating tank circuit, as shown in Figure 6.1, consisting of the stator winding inductance, L_s, stator winding resistance, R_s, and impulse generator's internal capacitor, C. The surge voltage waveform across the stator windings is a damped sinusoid during this transient electromagnetic process. The rotor squirrel-cage windings are coupled into the stator circuit. The stator and rotor windings interact like the primary and secondary windings of an air transformer. Since the coupling between the stator and rotor is through the air gap, any non-uniformity or change in the air gap is evident in the surge waveform.

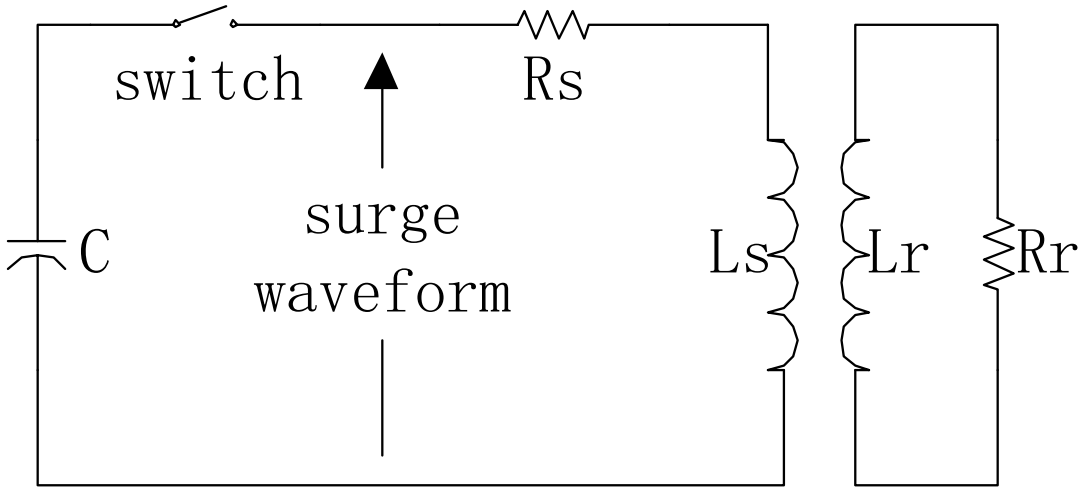

Figure 6.1. Equivalent circuit of the surge test.

6.3 Experimental Results

The test system, shown in Figures 6.2 and 6.3, consists of a commercial digital surge tester [51], a stepper motor, an induction motor, and a computer. Air gap eccentricity is created by inserting offset shims into the motor, as described in Chapter 3. The stepper motor is used to precisely control and vary the angle of the rotor with respect to the stator. The two motors are coupled together with a serpentine belt. By way of control signals from a computer, the two motors rotate with an angular step of 1.8º per pulse. At each of the 200 angular positions in one revolution, a surge test is carried out and the surge waveform is recorded to illustrate how the surge test characteristics are affected by the rotor position. The damping speed of the surge waveforms, i.e., the zero-crossing points, on two different induction motors with and without air gap eccentricity, is then compared.

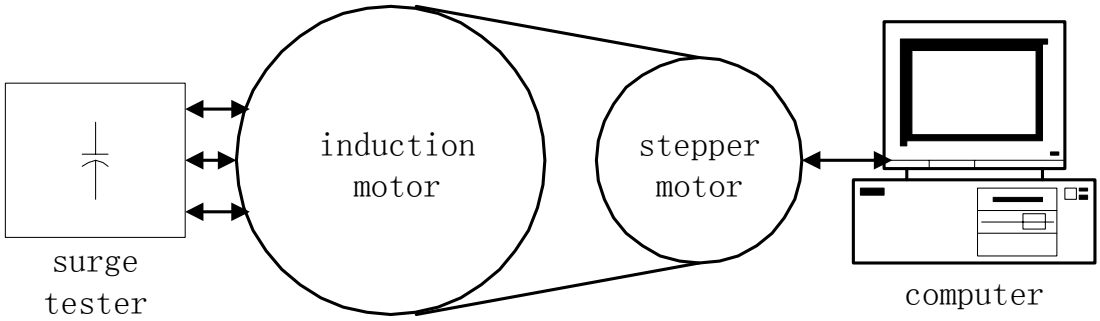

Figure 6.2. Block diagram of the surge test setup.

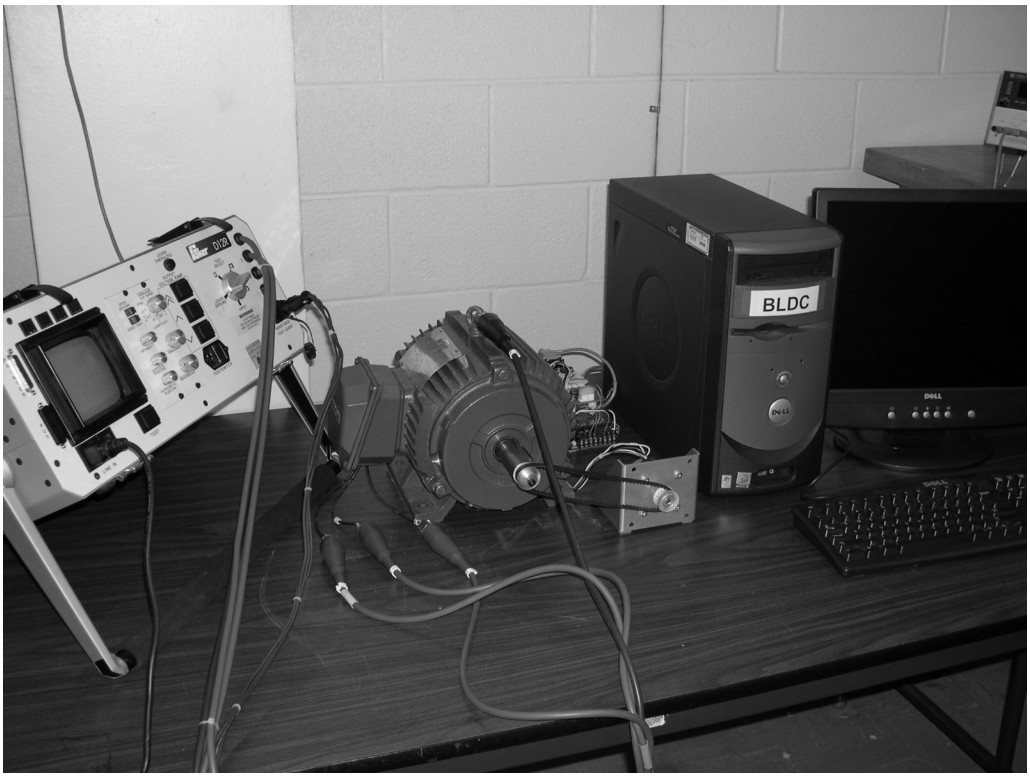

Figure 6.3. Surge test experimental system.

Experimental results are shown in Figures 6.4 to 6.6. The voltage waveform during a surge test is shown in Figure 6.4. In the surge test, the capacitor is first charged to 1920 V, which is determined by [51]

$$V_{surge} = 1000 + 2 * V_{rated} \tag{6.1}$$

Then, the capacitor discharges and the voltage reduces resonantly to zero until around 700 μs, the same as in the above analysis.

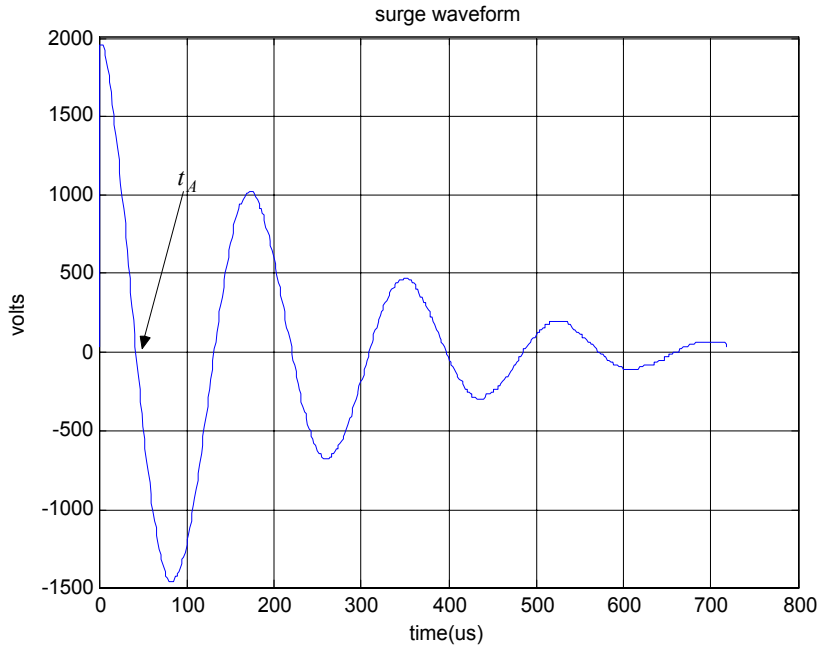

Figure 6.4. Surge waveform of the induction motor.

The time t_A taken at the first zero-crossing point, illustrated in Figure 6.4, for each angular position is recorded. How this time t_A changes as the motor undergoes one complete revolution is shown in Figures 6.5 and 6.6 for a healthy motor and for a faulty motor with an eccentric rotor, respectively. In Figure 6.5, the upper-most plot corresponds to the surge test of phase *a*, the middle one to phase *b*, and the bottom one to phase *c*. The zero-crossing point t_A oscillates around 42.3 μs because the air gap between the rotor and stator changes slightly in rotation because of the stator slots and rotor bars. However, the characteristics of the faulty motor in Figure 6.6 are totally different. The oscillation in Figure 6.5 appears in Figure 6.6 as spikes on the flat curve, but with a much smaller magnitude, and is superimposed on a lower-frequency wave caused by air gap eccentricity. This low-frequency wave repeats itself four times per rotor revolution because it is a four-pole machine. The experimental results in Figure 6.6

for three phase windings are identical, but are phase shifted according to the winding layout.

Various pattern recognition techniques may be used to provide a metric that clearly indicates the differences between Figures 6.5 and 6.6. In this research, the fundamental frequencies of these waveforms are compared to detect the air gap eccentricity. The spectra of the six waveforms in Figures 6.5 and 6.6 are now shown in Figures 6.7 and 6.8. In Figures 6.7 and 6.8, the DC components have been filtered in order to easily observe other harmonics. The frequency spectra of the waveforms for phases a, b, and c are similar for the healthy motor. For the faulty motor, the three spectra are also similar. The fundamental component of the healthy motor is located at 0.16 Hz, with amplitude of 0.49 μs, as shown in Figure 6.7. However, as shown in Figure 6.8, the fundamental component of the faulty motor reduces to 0.015 Hz, with smaller amplitude of 0.15 μs.

This is because in the rotation, the variation of air gap caused by rotor eccentricity is larger than that caused by stator slots and rotor bars. Thus, the change of t_A is mainly determined by the air gap eccentricity. For the experimental motors, the number of stator slots and rotor bars is much larger than the number of poles. Therefore, the fundamental frequency of the healthy motor is much larger, almost 10 times that of the faulty motor. A simple classifier can be used to detect the faulty motor by software.

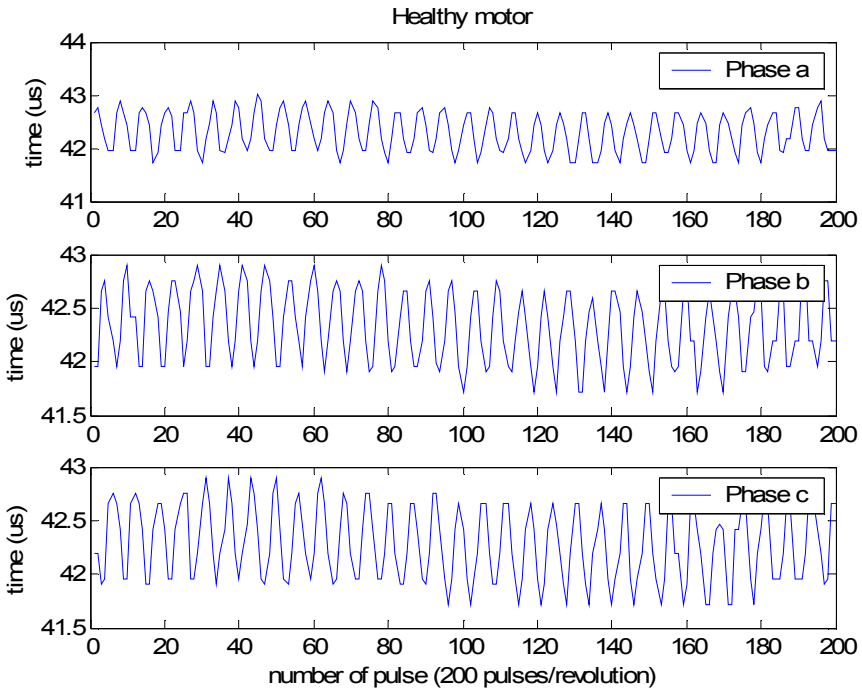

Figure 6.5. Surge test result of a healthy motor.

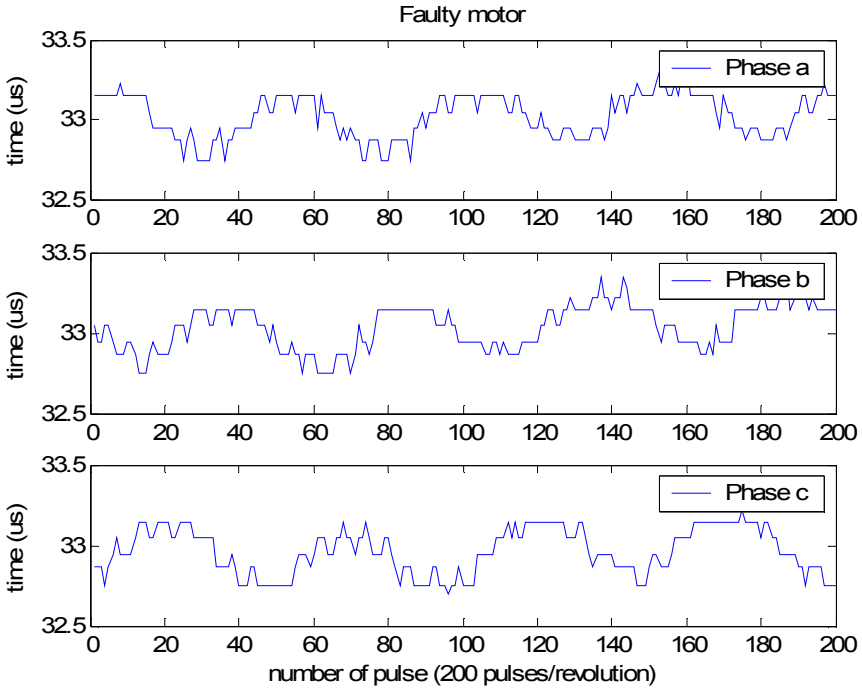

Figure 6.6. Surge test result of a faulty motor with an eccentric rotor.

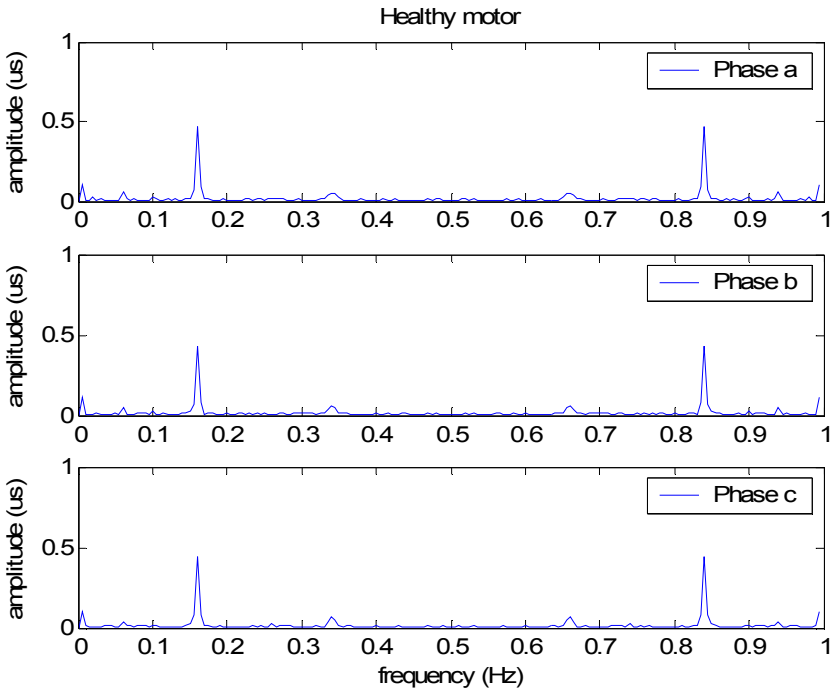

Figure 6.7. Spectral analysis of a healthy motor

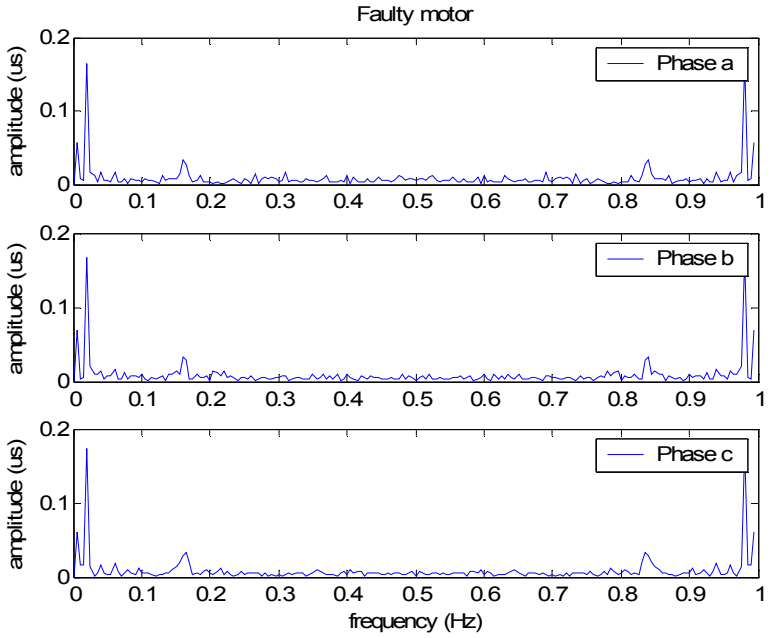

Figure 6.8. Spectral analysis of a faulty motor with an eccentric rotor

6.4 Conclusions

This chapter analyzed the effect of air gap eccentricity on surge waveforms. Air gap eccentricity made surge waveforms rotor-position dependent. In this way air gap eccentricity was clearly seen in surge waveforms, without high-frequency data acquisition and high-resolution signal processing.

A new detection method was proposed to detect air gap eccentricity in induction motors using the surge test. Experiments were carried out using a commercial surge tester to validate the feasibility of the proposed detection method. Compared to traditional methods based on spectral analysis, this new method is easier and more immune to noise. It is especially useful for routine and detailed off-line maintenance.

CHAPTER 7

CONCLUSIONS, CONTRIBUTIONS, AND RECOMMENDATIONS

7.1 Summary and Conclusions

The goal of this research is to design a detection scheme for air gap eccentricity in closed-loop drive-connected induction motors. Air gap eccentricity is a common effect arising from a range of mechanical problems in induction motors. Early detection of air gap eccentricity allows maintenance to be scheduled during a planned downtime, avoiding a costly emergency.

A literature review of existing methods in motor condition monitoring was presented in Chapter 2. Their features and limitations were analyzed. Among those techniques, MCSA is the most common detection method because stator current is readily available in most applications. MCSA can be implemented at no additional cost.

The first conclusion of this research is that MCSA is insufficient in detecting air gap eccentricity in closed-loop drive-connected induction motors. It is necessary to monitor the stator voltage and current together to ensure good detection sensitivity and reliability. When a motor is supplied by a vector-controlled drive, its supply voltage is not a pure sine wave as that of a line-connected machine. Fault harmonics exist in the stator voltage and current. The distribution of fault harmonics between the stator voltage and current is affected by the drive controllers and the mechanical load. The speed and current PI controllers make voltage harmonics larger, while the misalignment caused by the mechanical load increases current harmonic amplitudes. In the experiments, the

motor had 25.6% static eccentricity and 38.4% dynamic eccentricity. In the no-load test, when the motor ran at 300 rpm and 1200 rpm, the normalized voltage harmonic amplitudes were 0.0055 and 0.0013, while normalized current harmonics had smaller amplitudes of 0.001 and 0.0009, respectively. However, in the load test, at the same speed of 300 rpm and 1200 rpm, the normalized voltage harmonic amplitudes changed to 0.027 and 0.0077, while the current amplitudes became 0.0295 and 0.014 which were larger than the voltage harmonics. Furthermore, when speed bandwidth was reduced to 5 rad/s and motor was running at 1200 rpm, the voltage harmonic (amplitude of 0.001) again became larger than the current harmonic (amplitude of 0.0005). Monitoring either stator voltage or current alone reduced detection sensitivity and reliability, and it was necessary to monitor both variables together. Because stator voltage and current were readily available in the drive controllers, the proposed detection scheme monitored fault harmonics in the stator voltage and current space vectors. In this way the detection is sensorless, reliable, and cost effective.

The second conclusion of this research is that the detection scheme needs to incorporate the effects of changing operating conditions into the fault detection. Unlike line-connected motors, the speed and load of drive-connected motors vary widely. When a motor drives a mechanical load, they comprise a torsional spring system. The torsional spring system resonates at different degrees with changing motor operating conditions. The resonance, in turn, modulates air gap and changes the amplitudes of the eccentricity-related harmonics. For example, in the no-load test, when motor speed was increased from 300 rpm to 1755 rpm, the normalized voltage harmonic amplitudes changed from 0.0055 to 0.0012, and the current harmonics changed from 0.001 to 0.0009, respectively.

In the load test, these harmonics changed from 0.027 to 0.0043 and from 0.0295 to 0.005 for voltage and current, respectively. Thus, thresholds must be established that correspond to each possible operating condition. This is a challenge. First, the relationship between fault harmonic amplitudes and operating conditions is very complicated, because the resonance depends on many factors, such as motor size, installation, etc. It is difficult to formulate the relationship as strict analytical equations. Second, it is difficult to establish thresholds of all operating conditions by direct measurement, since motor speed and load may change continuously.

This investigation proposed a detection scheme using an artificial neural network. The neural network was trained to learn the relationship between fault harmonics and operating conditions and then was used to estimate the thresholds for fault detection. A neural network is usually represented by only a few neurons and therefore can be stored in a limited memory. In addition, since the neurons use non-linear activation functions, the estimations given by the neural network are more accurate than linear interpolations from a look-up table. The processes to design the neural network were described. For two sets of test data of 96 points and 70 points, the proposed neural network was able to distinguish the faulty motor and healthy motor correctly over the entire range of operating conditions of the experimental motors.

The third conclusion of this research is that the surge test is a useful off-line method for detecting air gap eccentricity in induction motors. Air gap eccentricity causes surge waveforms to be rotor-position dependent. The variation of surge waveforms in rotation can be used to indicate air gap eccentricity. In this research, how the first zero-crossing points of the surge waveforms changed in one complete revolution was used to

detect the eccentricity fault. For a healthy motor, the fundamental component of the change was at 0.16 Hz, with amplitude of 0.49 μs. However, for a faulty motor, this component was located at 0.015 Hz, with amplitude of 0.15 μs. The healthy motor and faulty motor were distinguished by comparing the fundamental frequencies. The surge test is an off-line method that does not require high-frequency data acquisition and high-resolution signal processing. This method is especially useful for routine and detailed maintenance.

7.2 Contributions

The contributions of this investigation are summarized as follows:

- This research is the first work to investigate applications of MCSA to the detection of air gap eccentricity in closed-loop drive-connected induction motors. The investigation helps understanding the limitations of existing detection techniques. The new detection method proposed in this work is able to diagnosis air gap eccentricity more sensitively and more reliably.
- The limitations of MCSA in detecting air gap eccentricity in closed-loop drive-connected induction motors are analyzed in detail. The effects of drive controllers and mechanical load on the distribution of fault harmonics between the stator voltage and current are investigated. It is pointed out that monitoring stator voltage and current together is necessary to ensure good detection sensitivity and reliability.

- To incorporate the variation of fault harmonic amplitudes with changing operating conditions into the fault detection, a detection scheme using an artificial neural network is proposed and experimentally verified.
- A direct time-stepping finite element model to simulate air gap eccentricity in closed-loop drive-connected induction motors is developed. The model can incorporate the effects of magnetic nonlinearities and space harmonics resulting from the machine magnetic circuit topology and winding layouts. Therefore, the simulation is more accurate than other methods such as the WFA. In addition to air gap eccentricity, this model is able to simulate other types of faults in drive-connected electrical machines.
- The effect of rotor eccentricity on surge waveforms is analyzed. A new off-line method for detecting air gap eccentricity is proposed and experimentally verified.

7.3 Recommendations

Some recommendations are listed for continuing investigation in this research field:

- More experiments need to be carried out to further evaluate the sensitivity and reliability of the proposed detection scheme on a wide range of electric machines with different degrees of air gap eccentricity, motor size, load types, and installations. For very small degrees of eccentricity and very small motors, the proposed detection scheme may fail because of insignificant fault harmonics. It is important to find these critical points.

- Some types of mechanical load, for example, a reciprocating compressor, can result in a sinusoidal torque oscillation at multiples of rotational speed. This type of load causes harmonics at the same frequencies as air gap eccentricity. The magnitudes of those harmonics are always much larger than those of fault harmonics. An efficient method to separate air gap eccentricity and load oscillation needs to be investigated.

REFERENCES

[1] EPRI, "Improved motors for utility applications and improved motors for utility applications industry assessment study", Vol. 1, *EPRI EL-2678, 1763-1,* final report, and Vol. 2, *1763-1* final report, October 1982.

[2] D. G. Dorrell, W. T. Thomson, and S. Roach, "Analysis of airgap flux, current, and vibration signals as a function of the combination fo static and dynamic airgap eccentricity in 3-phase induction motors," *IEEE Transactions on Industry Applications*, Vol. 33, No. 1, Jan./Feb. 1997, pp24-34.

[3] W. T. Thomson and A. Barbour, "On-line current monitoring and application of a finite method to predict the level of static airgap eccentricity in three-phase induction motors," *IEEE Transactions on Energy Conversion*, Vol. 13, No. 4, Dec. 1998, pp347-357.

[4] W. T. Thomson, D. Rankin, and D. G. Dorrell, "On-line current monitoring to diagnose airgap eccentricity in large three-phase induction motors-industrial case histories verify the predictions," *IEEE Transactions on Energy Conversion*, Vol. 14, No. 4, Dec. 1999, pp1372-1378.

[5] W. T. Thomson, D. Rankin, and D. G. Dorrell, "On-line current monitoring to diagnose airgap eccentricity-an industrial case history of a large high-voltage three-phase induction motors," *Electric Machines and Drives Conference Record*, 1997, ppMA2/4.1-MA2/4.3.

[6] W. T. Thomson and A. Barbour, "The on-line prediction of airgap eccentricity levels in large (MW range) 3-phase induction motors," *IEEE International Electric Machines and Drives Conference*, 1999, pp383-385.

[7] R. Schoen and T. G. Habetler, "Effects of time-varying loads on rotor fault detection in induction machines," *IEEE Transactions on Industry Applications*, Vol. 31, No. 4, July/Aug. 19995, pp900-906.

[8] R. Schoen and T. G. Habetler, "Effects of time-varying loads on rotor fault detection in induction machines," *IEEE Industry Applications Society Annual Meeting*, 1993, pp324-330.

[9] R. Schoen, B. K. Lin, T. G. Habetler, Jay H. Schlag, and Samir Farag, "An unsupervised, on-line system for induction motor fault detection using stator current monitoring," *IEEE Transactions on Industry Applications*, Vol. 31, No. 6, Nov./Dec. 1995, pp1280-1286.

[10] R. Schoen and T. G. Habetler, "Evaluation and implementation of a system to eliminate arbitrary load effects in current based monitoring of induction machines," *IEEE Transactions on Industry Applications*, Vol. 33, No. 6, Nov./Dec. 1997, pp1571-1577.

[11] B. Yazici and G. B. Kliman, "An adaptive statistical time-frequency method for detection of broken bars and bearing faults in motors using stator current," *IEEE Transactions on Industry Applications*, Vol. 35, No. 2, Mar./Apr. 1999, pp442-452.

[12] A. Bellini, F. Filippetti, G. Franceschini, and C. Tassoni, "Closed-loop control impact on the diagnosis of induction motors faults," *IEEE Transactions on Industry Applications,* Vol. 36, No. 5, Sept./Oct. 2000, 1318-1329.

[13] R. M. Tallam, T. G. Habetler, and Ronald G. Harley, "Stator winding turn-fault detection for closed-loop induction motor drives," *IEEE Industry Applications Society Annual Meeting*, 2002, pp1553-1557.

[14] R. R. Obaid and T. G. Habetler, "Current-based algorithm for mechanical fault detection in induction motors with arbitrary load conditions," *IEEE Industry Applications Society Annual Meeting*, 2003, pp. 1347-1351.

[15] R. R. Obaid, T. G. Habetler, and D. J. Gritter, "A simplified technique for detecting mechanical faults using stator current in small induction motors," *IEEE Industry Applications Society Annual Meeting*, 2000, pp479-483.

[16] J. S. Hsu, "Monitoring of defects in induction motors through air-gap torque observation," *IEEE Transactions on Industry Applications*, Vol. 31, No. 5, Sept./Oct. 1995, pp1016-1021.

[17] J. S. Hsu, H. H. Woodson, W. F. Weldon, "Possible errors in measurement of air-gap torque pulsations of induction motors," *IEEE Transactions on Energy Conversion,* Vol. 7, No. 1, Mar. 1992, pp202-208.

[18] S. Nandi, S. Ahmed, and H. A. Toliyat, "Detection of rotor slot and other eccentricity related harmonics in a three phase induction motor with different rotor cages," *IEEE Transactions on Energy Conversion*, Vol. 16, No. 3, Sept. 2001, pp253-260.

[19] S. Nandi, R. Mohan Bharadwaj, and H. A. Toliyat, "Mixed eccentricity in three phase induction machines: analysis, simulation and experiments," *IEEE Industry Applications Society Annual Meeting*, 2002, pp1525-1532.

[20] H. A. Toliyat, M. S. Arefeen, and A. G. Parlos, "A method for dynamic simulation of air-gap eccentricity in induction machines," *IEEE Transactions on Industry Applications*, Vol. 32, No. 4, July/Aug. 1996, pp910-918.

[21] A. Bellini, *et. al.*, "On-field experience with online diagnosis of large induction motors cage failure using MCSA," *IEEE Transactions on Industry Applications*, Vol. 38, No. 4, July/Aug. 2002, pp1045-1053.

[22] W. T. Thomson and M. Fenger, "Industrial application of current signal analysis to diagnose faults in 3-phase squirrel cage induction motors," *Pulp and Paper Industry Technical Conference*, 2000, pp205-211.

[23] M. E. H. Benbouzidi, M. Viera, and C. Theys, "Induction motors' faults detection and localization using stator current advanced signal processing techniques," *IEEE Transactions on Power Electronics*, Vol. 14, No. 1, Jan. 1999, pp14-22.

[24] M. E. H. Benbouzid, H. Nejjari, R. Beguenane, and M. Vieira, "Induction motor asymmetrical faults detection using advanced signal processing techniques," *IEEE Transactions on Energy Conversion*, Vol. 14, No. 2, June 1999, pp147-152.

[25] A. Barbour and W. T. Thomson, "Finite element study of rotor slot designs with respect to current monitoring for detecting static airgap eccentricity in squirrel-cage induction motors," *IEEE Industry Applications Society Annual Meeting*, 1997, pp112-119.

[26] N. A. O. Demerdash and J. F. Bangura, "Characterization of induction motors in adjustable-speed drives using a time-stepping coupled finite-element state-space method including experimental validation," *IEEE Transactions on Industry Applications*, Vol. 35, No. 4, July/Aug. 1999, pp790-802.

[27] W. N. Fu, P. Zhou, D. Lin, S. Stanton, and Z. J. Cendes, "Modeling of solid conductors in 2-D transient finite element analysis and its application to electric machines," *IEEE International Electric Machines and Drives Conference*, 2003, pp1272-1278.

[28] X. Huang and T. G. Habetler, "Analysis of air gap eccentricity in closed-loop drive-connected induction motors," *IEEE International on Electric Machines and Drives Conference*, 2003, pp1443-1447.

[29] H. Nejjari and M. E. H. Benbouzid, "Monitoring and diagnosis of induction motors electrical faults using a current Park's vector pattern learning approach," *IEEE Transactions on Industry Applications*, Vol. 36, No. 3, May/June 2000, pp730-735.

[30] A. J. M. Cardoso and E. S. Saraiva, "Computer-aided detection of airgap eccentricity in operating three-phase induction motors by Park's vector approach," *IEEE Transactions on Industry Applications*, Vol. 29, No. 5. Sept./Oct. 1993, pp897-901.

[31] A. J. M. Cardoso, E. S. Saraiva, M. L. Sousa Mateus, and A. L. Ramalho, "On-line detection of airgap eccentricity in 3-phase induction motors, using Park's vector approach," *IEEE Industry Applications Society Annual Meeting*, 1991, pp94-98.

[32] A. M. S. Mendes and A. J. M. Cardoso, "Voltage source inverter fault diagnosis in variable speed AC drives, by the average current Park's vector approach," *IEEE International Electric Machines and Drives Conference*, 1999, pp704-706.

[33] R. S. Wieser, M. Schagginger, C. Kral, and F. Pirker, "The integration of machine fault detection into an indirect field oriented induction machine drive control scheme the Vienna monitoring method," *IEEE Industry Applications Society Annual Meeting*, 1998, pp278-285.

[34] F. Filippetti, G. Franceschini, C. Tassoni, and Peter Vas, "AI techniques in induction machines diagnosis including the speed ripple effect," *IEEE Transactions on Industry Applications*, Vol. 34, No. 1, Jan./Feb. 1998, pp98-108.

[35] A. Murray and J. Penman, "Extracting useful higher order featues for condition monitoring using artificial neural networks," *IEEE Transactions on Signal Processing,* Vol. 45, No. 11, Nov. 1997, pp2821-2828.

[36] P. V. Goode and M-Y Chow, "Using a neural/fuzzy system to extract heuristic knowledge of incipient faults in induction motors: part I-methodology," *IEEE Transactions on Industrial Electronics*, Vol. 42, No. 2, April 1995, pp131-138.

[37] P. V. Goode and M-Y Chow, "Using a neural/fuzzy system to extract heuristic knowledge of incipient faults in induction motors: part II-application," *IEEE Transactions on Industrial Electronics*, Vol. 42, No. 2, April 1995, pp139-146.

[38] A. Bernieri, G. Betta, and C. Liguori, "On-line fault detection and diagnosis obtained by implementing neural algorithm on a digital signal processor," *IEEE Transactions on Instrumentation and Measurement*, Vol. 45, No. 5, October 1996, pp894-899.

[39] Z. Ye, B. Wu, and A. R. Sadeghian, "Induction motor mechanical fault online diagnosis with the application of artificial neural network," *IEEE Applied Power Electronics Conference*, 2001, pp1015-1020.

[40] M. E. H. Benbouzid and H. Nejjari, "A simple fuzzy logic approach for induction motors stator condition monitoring," *IEEE International Electric Machines and Drives Conference*, 2001, pp634-639.

[41] G. Betta, M. D'Apuzzo, and A. Pietrosanto, "A knowledge-based approach to instrument fault detection and isolation," *IEEE Transactions on Instrumentation and Measurement*, Vol. 44, No. 6, Dec. 1995, pp1009-1016.

[42] A. J. Ellison and S. J. Yang, "Effects of rotor eccentricity on acoustic noise from induction machines," *Proceedings of IEE*, 118, (1), 1971, pp174-184.

[43] S. P. Verma and R. Natarajan, "Effects of eccentricity in induction motors," *International Conference of Electric Machines*, 1982, pp930-933.

[44] K. J. Binns and W. T. Barnard, " Some aspects of the use of flux and vibration spectra in electrical machines," *Proceedings of Conference on Applications on time-series analysis*, University of Southampton, Southampton, UK, 1977, pp71.1-71.12.

[45] C. M. Riley, B. K. Lin, T. G. Habetler, and R. R. Schoen, "A method for sensorless on-line vibration monitoring of induction machines," *IEEE Transactions on Industry Applications,* Vol. 34, No. 6, Nov./Dec. 1998, pp1240-1245.

[46] C. M. Riley, B. K. Lin, T. G. Habetler, and Gerald B. Kliman, "Stator current harmonics and their causal vibrations: a preliminary investigation of sensorless vibration monitoring applications," *IEEE Transactions on Industry Applications*, Vol. 35, No. 1, Jan./Feb. 1999, pp94-99.

[47] X. Huang, T. G. Habetler, and R. G. Harley, "Detection of rotor eccentricity faults in closed-loop drive-connected induction motors using an artificial neural network," *IEEE Power Electronics Specialist Conference*, 2004.

[48] X. Huang and T. G. Habetler, "Detection of mixed air gap eccentricity in closed-loop drive-connected induction motors," *IEEE International Symposium on Diagnostics for Electric Machines, Power Electronics and Drives*, 2003, pp312-316.

[49] J. R. Cameron, W. T. Thomson, and A. B. Dow, "Vibration and current monitoring for detecting airgap eccentricity in large induction motors," *Proceedings of IEE*, Vol. 133, Pt. B, No. 3, May 1986, pp155-163.

[50] E. Wiedenbrug, G. Frey, and J. Wilson, "Impulse testing as a predictive maintenance tool," *IEEE International Symposium on Diagnostics for Electric Machines, Power Electronics and Drives*, 2003, pp13-19.

[51] Baker Instrument, "Digital surge / DC HiPot / resistance tester D3R/D6R/D12R users manual," *Baker Instrument Manual*, 2000.

[52] J. Stack, "*Fault signature detection for rolling element bearings in electric machines*," Ph.D. Dissertation, Georgia Institute of Technology, U.S., 2002.

[53] R. M. Tallam, "*Current-based sensorless detection of stator winding turn faults in induction machines*," Ph.D. Dissertation, Georgia Institute of Technology, U. S., 2001.

[54] R. R. Obaid, "*Detection of rotating mechanical asymmetries in small induction machines*," Ph.D. Dissertation, Georgia Institute of Technology, U.S., 2002.

[55] R. Schoen, "*On-line current-based condition monitoring of three-phase induction machines*," Ph.D. Dissertation, Georgia Institute of Technology, U.S., 1994.

[56] N. Mohan, "*Electric drives-an integrative approach*," year 2001 edition, published by MNPERE, 2001.

[57] G. Ellis, "*Control system design guide: using your computer to understand and diagnose feedback controllers*," second edition, published by Academic Press, 2000.

[58] S. Haykin, "*Neural networks: a comprehensive foundation*," second edition, published by Prentice Hall, 1999.

[59] Ansoft Corporate, "Maxwell® 2D field simulator,"*Ansoft Corp. Manual*, 2002.

[60] W. le Roux, R. G. Harley, and T. G. Habetler, "Rotor fault analysis of a permanent magnet synchronous machine," *International Conference on Electric Machines*, Bruges, Belgium, 2002.

[61] N. A. Al-Nuaim and H. A. Toliyat, "A novel method for modeling dynamic air-gap eccentricity in synchronous machines based on modified winding function approach," *IEEE Transactions on Energy Conversion*, Vol. 13, No. 2, June, 1998, pp156-162.

[62] H. A. Toliyat, T. A. Lipo, and J. C. White, "Analysis of a concentrated winding induction machines for adjustable speed drive applications," *IEEE Transactions on Energy Conversion*, Vol. 6, No. 4, December, 1991, pp679-683.

[63] M. Haji and H. A Toliyat, "Pattern recognition-a technique for induction machines rotor fault detection 'broken bar fault'", *International Conference on Electric Machines and Drives Conference*, 2001, pp899-904.

[64] M. Haji and H. A. Toliyat, "Pattern recognition-a technique for induction machines rotor fault detection 'eccentricity and broken bar fault'," *Industrial Applications Society Annual Meeting*, 2001, pp1572-1578.

[65] G. B. Kliman and D. Song, "Remote monitoring of DC motor sparking by wavelet analysis of the current," *IEEE Symposium on Diagnostics for Electric Machines, Power Electronics and Drives*, 2003, pp25-27.

VITA

Xianghui Huang was born in Henan, China on June 17, 1975. He received his dual Bachelor of Engineering Degrees in Power Engineering and Mechanical Engineering, and the Master of Engineering Degree in Power Engineering from Shanghai Jiao Tong University, Shanghai, China in 1997 and 2000, respectively.

In August 2001, he began his study at Georgia Institute of Technology, Atlanta, GA, where he has been pursuing his doctoral study in electric machine condition monitoring. While at Georgia Tech, he worked as a research assistant in Power Electronics and Motor Diagnostics Group in the School of Electrical and Computer Engineering. He is a student member of the IEEE and the IEEE Power Engineering Society's Georgia Tech Chapter.